14th DELTA
User Meeting

&

Annual Report 2018

Dortmund
28. November 2018

Edited by C. Sternemann, R. Wagner,
D. Lützenkirchen-Hecht (2018)

November 2018

Preface

Dear reader, dear colleague,

with this 14th annual report, you'll see a summary of the progress made in the operation and the upgrade of the DELTA machine and the scientific results obtained at the different beamlines since the last users meeting in 2017. The reports on instrumentation dealing with e.g. orbit feedback, the new RF systems and the survey and alignment of magnets and vacuum chambers have huge importance for our daily work at DELTA. Those activities mirror the efforts that are continuously spent by the machine group to improve the machine performance, in particular to make DELTA work as reliably as possible, and we take the opportunity to thank all the involved scientists, engineers and technicians. Moreover, the status report on the DELTA machine, the planned and already performed upgrade work and a first glance at DELTA's far future underline the significant developments of the DELTA machine.

The annual report also reflects the various activities from users – from regional, national and international universities and institutions – performing their research at DELTA synchrotron radiation source. Going through the numerous contributions, it is impossible to identify a real core area. The presented research addresses biology and life sciences, matter under extreme conditions in terms of pressure and temperature, engineering science, surface science and thin film physics, making use of the various experimental techniques available at DELTA, from soft X-ray photoelectron spectroscopy and photoelectron diffraction, to hard X-ray scattering and different X-ray spectroscopies.

Finally, we have to thank the involved universities and research institutions, in particular the TU Dortmund, the local government and the diverse funding agencies for their manifold support of the activities compiled here – without such efforts the conducted projects would not have been possible. We gratefully acknowledge all these different contributions.

Christian Sternemann, Ralph Wagner & Dirk Lützenkirchen-Hecht

Contents:

Instrumentation

Status and Future of DELTA

S. Khan for the DELTA accelerator team[1]

Zentrum für Synchrotronstrahlung (DELTA), Technische Universität Dortmund

Operation in 2018. DELTA is a 1.5-GeV synchrotron light source operated by the TU Dortmund, comprising a linear pre-accelerator, a full-energy booster synchrotron and a storage ring with 115.2 m circumference. It is operated 2000 hours/year for synchrotron radiation users and 1000 hours/year for accelerator physics studies. The average availability, i.e., the ratio of delivered to scheduled user beam time, was 93.7% in 2018 (quarter I to III) due to problems with the cooling water plant, the orbit correction system, the injection chain, and other minor issues. After venting the southwest arc of the storage ring in 2017, the beam lifetime has fully recovered reaching optimum values >16 h (at 100 mA). In addition to testing the new superconducting wiggler, extensive infrastructure work was undertaken during the 2018 summer shutdown, including cooling water installation for the upgrade of the radiofrequency (RF) system and replacing the maintenance-intensive and inefficient ceiling lights in the accelerator hall by LED-based lamps.

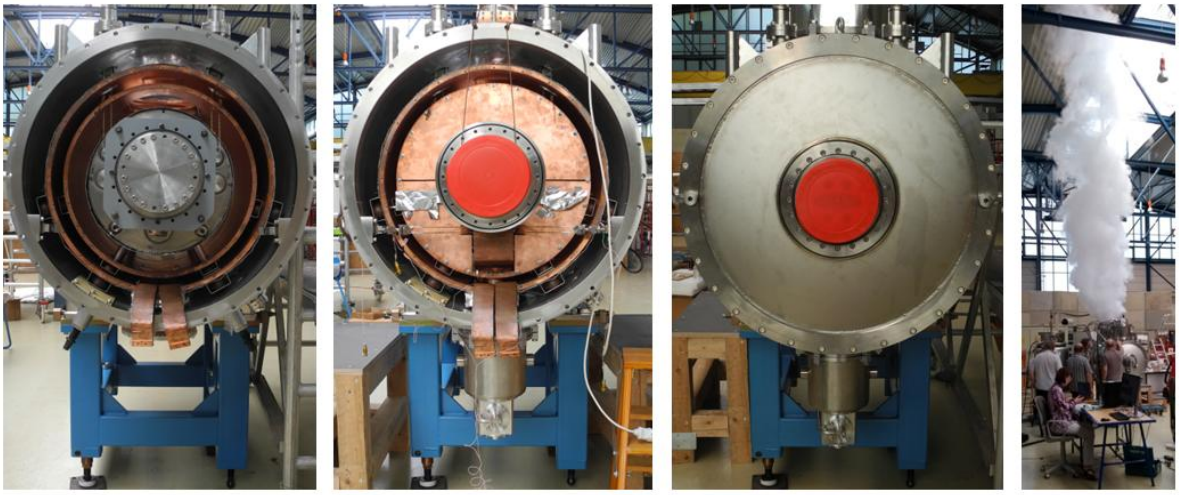

Figure 1: The new 7-T superconducting wiggler at different stages of its assembly. Right: A quench during training of the superconducting coils.

Upgrades. A new superconducting wiggler had been manufactured at BINP in Novosibirsk [1] and was delivered by truck on July 20th 2018. In addition to a higher peak field (7 T instead of 5.3 T), the number of periods is increased (9 instead of 5) and the liquid-He consumption will be close to zero (instead of 130 l/week). After extensive preparations to provide electric power, cooling water, liquid nitrogen, liquid helium , vacuum etc., the wiggler was assembled (see Fig. 1), cooled to 4 K, and quench-trained by experts from BINP within a period of 4 weeks. The design field of 7 T was reached after 5 quenches, and with 3

[1] A. Althaus, W. Brembt, B. Büsing, G. Dahlmann, T. Dybiona, A. Erpelding, J. Friedl, A. Glassl, P. Hartmann, B. Hippert, B. Isbarn, S. Khan, V. Kniss, S. Kötter, D. Krieg, C. Mai, A. Meyer auf der Heide, B. Riemann, D. Rohde, H.-P. Ruhl, D. Schirmer, G. Schmidt, F. Teutenberg, T. Schulte-Eickhoff, M. Sommer, T. Weis

more quenches, a field of 7.2 T was achieved. Magnetic measurements showed satisfactory values of the field integrals and the field variation during a 70-hour test was about 10^{-4} T.

In view of the higher energy loss due to the new wiggler, a second RF cavity will be added to the storage ring. The new EU-type cavity was manufactured, delivered, and is being tested using a recently installed 75-kW solid-state amplifier [2]. The horizontal realignment of all vacuum chambers and magnets or upgrades of the control system was finalized [3]. This and the progress on other activities of the DELTA accelerator group including results from the short-pulse facility are presented in other articles of this Annual Report [4-11].

The future. A major future project is the upgrade of the short-pulse source using EEHG (echo-enabled harmonic generation) [12] to generate ultrashort radiation pulses at shorter wavelengths. Here, progress has been made regarding beam optics, vacuum chambers, and magnets [4]. A design study for ultrafast electron diffraction (see, e.g., [13]) using a future few-MeV source of femtosecond electron bunches at DELTA is underway in collaboration with a group from the University of Duisburg-Essen [7]. Regarding the far future of accelerator physics at TU Dortmund, already addressed at a first workshop in July 2016, a second workshop was held on February 20th 2018 and the issue is under further discussion.

References

[1] N. Mezentsev, E. Wallén, *Superconducting Wigglers*, Sync. Rad. News 24:3, 3 (2011).
[2] P. Hartmann et al., *DELTA Radiofrequency Systems*, this Annual Report.
[3] G. Schmidt et al., *Survey and Alignment of the DELTA Magnets and Vacuum Chamber*, this Annual Report.
[4] B. Büsing et al., *Progress towards EEHG at the DELTA Short-Pulse Facility*, this Annual Report.
[5] A. Glassl et al., *Reducing the Momentum Compaction Factor of the Storage Ring at DELTA Based on Simulations with a New Lattice Model*, this Annual Report.
[6] S. Kötter et al., *Upgrading the Slow Orbit Feedback of DELTA with New Software*, this Annual Report.
[7] D. Krieg et al., *Photocathode Gun Cavity for an Electron Gun for Ultrafast Electron Diffraction at DELTA*, this Annual Report.
[8] N. Neumann et al., *Estimate of the Spectral Bandwidth of Tunable THz Radiation at DELTA*, this Annual Report.
[9] A. Meyer auf der Heide et al., *Estimate of the Beam Energy Spread at the Short-Pulse Facility*, this Annual Report.
[10] D. Schirmer, First Experience with Machine Learning Techniques in DELTA Controls, this Annual Report.
[11] M. Sommer et al., *Numerical Tracking Studies on Coupled-Bunch Instabilities in the Presence of RF Phase Modulation*, this Annual Report.
[12] G. Stupakov, *Using the Beam-Echo Effect for Generation of Short-Wavelength Radiation*, Phys. Rev. Lett. 102, 074801 (2009).
[13] S. P. Weathersby et al., *Mega-electron-volt ultrafast electron diffraction at SLAC National Accelerator Laboratory*, Rew. Sci. Instrum. 86, 073702 (2015).

DELTA Radiofrequency Systems

P. Hartmann, W. Brembt, V. Kniss, T. Weis and the DELTA team
Zentrum für Synchrotronstrahlung (DELTA), Technische Universität Dortmund

Linac & Booster RF Systems. The 3-GHz radiofrequency (RF) system of the Linac and the 500 MHz booster RF system did not cause any trouble in 2018. As of Nov. 8, 2018, the 500-MHz solid-state amplifier of the booster, installed in Feb. 2017, ran for a total of 5634 hours without causing any trouble.

Even though no module drop-outs had been detected at the booster amplifier (see below), all booster amplifier modules were reworked in June 2018 by the manufacturer. This had no effect on the amplifiers performance.

Low-Level RF. The 15 years old RF master clock for booster and storage ring was replaced in September 2018 by a new generator. This became necessary when the base frequency of the 500 MHz Systems was moved from 499.819 MHz to 499.830 MHz due to magnet alignment. The old master generates a phase jump at 499.825 MHz whenever its frequency is tuned. This repeatedly led to a beam loss in the storage ring. The newly installed generator may be tuned over the full available frequency range from 499.3 MHz to 500.3 MHz without losing the stored beam due to the 'phase-continuous frequency setting' feature.

DELTA RF System. The RF tube amplifier providing up to 40 kW RF power to the single DORIS-type cavity in the storage ring also caused no trouble in 2018.

In preparation of the installation of a second (EU-type) cavity, the cooling water supplies of the old RF system were reordered and connected to a new water distributor. Hereby we discovered that there was no water flow through the snout of the DORIS coupler. Since this particular water flow had never been surveyed, this state may have persisted for several months, maybe even for years. The RF coupler will be replaced during the winter shutdown by a spare coupler which sits under vacuum on a spare cavity in the RF lab at DELTA. The new water distributor has flow interlocks on all water lines.

Preparation for the installation of the EU-type cavity in the storage ring. Several preparatory steps have been performed:

1. Installation of a new high-capacity cooling water line to the tube amplifier cabinet.
2. Installation of a new water distributor for the old RF system with flow regulators and interlocks on each water outlet.
3. Replacement of the glycol-cooled dummy loads of the booster and the storage ring by deionized water cooled dummy loads.
4. Decommissioning of the glycol cooling system. The 8-m^3 stand with heat exchanger, pump, etc. will be dismounted in the winter shutdown. This makes way for a new water rack for the EU-type cavity.
5. A second new flow-regulated and interlocked water distributor for the EU-type cavity with its 13 separate water lines is waiting to be installed.
6. The environment of the future position of the EU-type cavity was carefully surveyed. The

position of the base plate of the cavity support was determined to better than 1 mm. The base plate itself will be mounted on the girder during winter shutdown.
7. A commercially available digital low-level RF system was purchased. Once the second cavity will be installed in the ring, it will be used to control phase, amplitude and plunger position of both cavities. The system needs a dedicated motor controller that was purchased and is currently being commissioning by the DELTA controls group.

EU cavity commissioning. The EU-type cavity was delivered in Dec. 2017. Environmental installations had been prepared beforehand or were installed in winter/spring 2018:
1. An in-house developed remote-controlled water distributor with 13 flow-regulated and interlocked water ports,
2. an in-house developed interlock system fast enough for the power circulators arc detector,
3. a stand-alone water cooler for the power circulator,
4. a roughly 10 meters long coaxial RF power line equipped with a calibrated directional coupler right in front of the cavity between the circulator and the cavity,
5. automated remote power measurements to survey the commissioning of the cavity,
6. vacuum pumps and an interlocked vacuum gauge (interlock level: 10^{-6} mbar),
8. a newly developed plunger controller, developed at BESSY (HZB, Berlin) and deployed at DELTA for the first time.

The cavity was baked for one week at 130°C. RF conditioning started on April 23, 2018. Due to very good vacuum behavior, pulsed conditioning was not necessary. After only four days the maximum forward power of 72 kW, measured at the directional coupler in front of the cavity, was reached.

Starting at 60 kW forward power, a strong increase of X-ray radiation was observed at the entrance door of the bunker. At 72 kW forward power, we measured up to 3 μSv/h. Conditioning was stopped and an additional lead shield was installed at the bunker door. This limited the measured radiation to below 1 μSv/h.

During the following roughly 400 hours of operation, mainly at 72 kW forward power, the radiation level decreased to about two thirds of its initial value.

In May 2018, we observed a decrease of output power of the 75-kW solid-state amplifier (SSA). This was due to badly screwed contacts at the output of sub-modules of the SSA. Hence, all amplifier modules of the storage-ring amplifier and the booster amplifier were re-worked by the manufacturer. The screwed contacts were replaced by soldered contacts. Module drop-outs have not been observed ever since.

In order to cure a known problem with the diagnostic coupler, we vented the cavity mid-August. The uncoated ceramic cap that protects the coupler was replaced by ceramic cap coated with 1 μm titanium. In addition, we changed tapers and installed an additional ion getter pump on the beam port of the cavity.

During the following re-conditioning process, the vacuum window of the coupler broke just before arriving at 25 kW RF power. An investigation of the broken coupler showed that sparking took place on the outside of the vacuum window in the volume between the two

ceramic plates of the coupler. This volume is purged with pressurized air to provide cooling to the ceramic plates. The reason for sparking is unknown. The repair of the coupler will take 4 months at least.

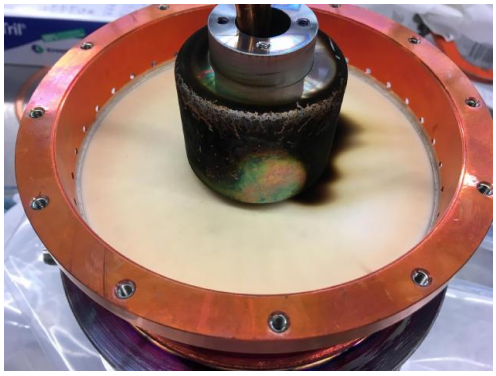

Figure 1: Vacuum window of the broken coupler. The outside ceramic plate and the brass housing are removed (courtesy Research Instruments GmbH).

Implications of the coupler accident. In order to avoid this type of accident in the future, several provisions are made:

1. An additional particle filter was installed in the air tube in front of the coupler.
2. A fast proportional reflected power interlock is currently being developed and will be installed at the directional coupler in front of the cavity. This interlock will on the long run also be installed at the DORIS-type cavity in the ring.
3. The integration of an arc detector into the coupler is currently being considered.

In addition, the response time of the vacuum interlock will be substantially decreased by bypassing the interlock relay of the vacuum gauge with a fast electronics device.

We appreciate help with words and deeds from W. Anders and V. Dürr from HZB, Berlin, and J. Jacob from ESRF, Grenoble.

Upgrading the Slow Orbit Feedback of DELTA with New Software

Stephan Kötter, Benjamin Isbarn, Andreas Glassl, Malte Sommer, Thomas Weis
Zentrum für Synchrotronstrahlung (DELTA), Technische Universität Dortmund

A new slow-orbit-feedback software is under commissioning at DELTA. It minimizes the deviation of the measured transverse orbit from a reference orbit by altering the currents of the available steerer magnets. This is necessary to avoid beam loss, protect hardware components from being heated by synchrotron radiation, maximize photon flux for beamlines and locate the beam next to the septum in the injection area. The transverse orbit position of the storage ring is currently controlled via a customized SVD-based approach in service since 2005 [1]. The main goals in replacing this software are increasing reliability, versatility and performance.

Correcting the orbit requires solving a convex minimization problem [2]. At DELTA, this problem is subject to inequality constraints which account for the limited range of the available steerer magnets [1]. The new software deploys an implementation of a primal-dual interior point method on a second-order cone from the CVXOPT Python package to solve this problem [3]. This method type heavily exploits the problem structure of convex optimization problems subject to arbitrary linear equality and inequality constraints [6]. Major advantages of this algorithm type over the SVD-based approach currently in use are their versatility in natively handling constraints, their predictable run time [5] and their theoretically proven feature of finding an optimal solution if there is any [6].

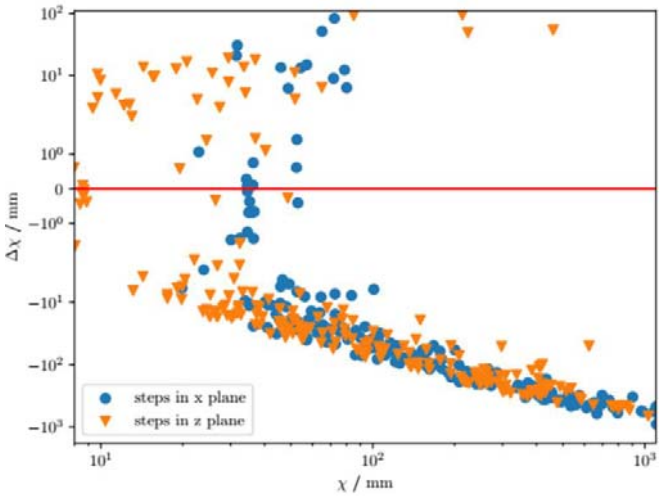

Figure 1: The quantity χ measures the overall deviation of the actual orbit from the reference orbit including weight factors for selected beam position monitors (BPMs). A negative value of its change $\Delta\chi$ for one correction step indicates an improvement. Positive values of $\Delta\chi$ arise from the limited accuracy of BPMs and correctors, and only values $\Delta\chi > 100$ mm are considered to be miscorrections.

In spring 2018, the new software was shown to work in principle without miscorrections (Fig. 1) [6]. Shortly after this, the quality of the applied orbit correction of the new and old slow-orbit-feedback software was compared by testing both programs on the same set of perturbations [6]. Both programs performed similar with the new program performing slightly better. The correction speed was found to be limited by the current sources and the network driver controlling the ramping process. In summer, the new software was enabled to keep the transverse orbit position at each BPM fixed or within a fix range by further exploiting the ability of the software to handle inequality constraints. This approach is

similar to the Eigenvector Method with Constraints (EVC) demonstrated at the Super-SOR light source and the Advanced Light Source (ALS) presented in [7] and may replace the weight factors currently in use at DELTA to increase correction quality in insertion devices and at the injection area.

The new slow-orbit-feedback software will be further upgraded in the upcoming months. Features in development include removing the pincushion distortion from orbit measurements based on signal function simulations of the DELTA beam position monitors [8] and adding a second optimization problem to reduce overall corrector strengths by exploiting linear dependencies in the regularized orbit-response matrix. In addition, the user interface will be reworked to comply with an ongoing effort to update the panels of the control system at DELTA. The software is expected to enter service early 2019.

References

[1] M. Grewe, *Orbitkorrektur am Speicherring DELTA*, Dissertation, TU Dortmund (2005).

[2] H. Wiedemann, *Particle Accelerator Physics*, 3rd ed. Berlin: Springer (2007).

[3] CVXOPT: *A Python package for convex optimization*. http://abel.ee.ucla.edu/cvxopt

[4] A. Ben-Tal et al., *Lectures on Modern Convex Optimization: Analysis, Algorithms, Engineering Applications*. Philadelphia: MOS-SIAM Series on Optimization (2001).

[5] S. Sra et al., *Optimization for Machine Learning*. MIT Press (2011).

[6] S. Kötter, *Evaluation of an Interior Point Method Specialized in Solving Constrained Convex Optimization Problems for Orbit Correction at the Electron Storage Ring at DELTA,* Proc. IPAC18, Vancouver, Canada (2018), 3507.

[7] N. Nakamura et al., *New orbit correction method uniting global and local orbit corrections*, Nucl. Instr. Methods A 556 (2006), 421.

[8] A. Jankowiak, *Strahldiagnose und Closed-Orbit-Charakterisierung mit HF-Strahllagemonitoren am Beispiel der Synchrotronstrahlungsquelle DELTA*, Dissertation, TU Dortmund (1999).

Numerical Tracking Studies on Coupled-Bunch Instabilities in the Presence of RF Phase Modulation

M. Sommer, B. Isbarn, S. Kötter, T. Weis
Zentrum für Synchrotronstrahlung (DELTA), Technische Universität Dortmund

Introduction

Recently, the suppression of coupled-bunch instabilities by RF phase modulation was analyzed by experimental studies [1,2] as presented in the last annual report. The voltage in the accelerating cavity in the presence of RF phase modulation can be described by

$$U(t) = U_0 \sin\left(\omega_{RF} t + A_m sin(\omega_{mod} t)\right)$$

with the amplitude U_0, the RF frequency ω_{RF}, the modulation amplitude A_m and the modulation frequency ω_{mod}. The optimum value of ω_{mod} could be confirmed to be slightly below twice the synchrotron frequency ω_s, as expected from previous works at other accelerators. In addition, the dependence of $\tau^{-1} = \tau_g^{-1} - \tau_d^{-1}$, with the coupled-bunch growth rate τ_g^{-1} and damping rate τ_d^{-1}, on the modulation amplitude A_m was analyzed and could be determined to be quadratic. To validate these studies, a numerical simulation code was developed [3], based on [4]. It combines the usually used concept of representing the electron bunches by rigid macroparticles to calculate coupled-bunch effects with a multi-particle approach to calculate phase modulation effects. The numerical results of one bunch with $n_p = 10000$ particles tracked over $n_t = 20000$ turns are shown in Fig. 1. The energy deviation (rms) and the time deviation of the center of mass of the bunch relative to the reference particle are shown together with the phase space of one particle and the wake field inside the accelerating cavity. The growth rate τ_g^{-1} is determined by an exponential fit on the envelope of the wake field.

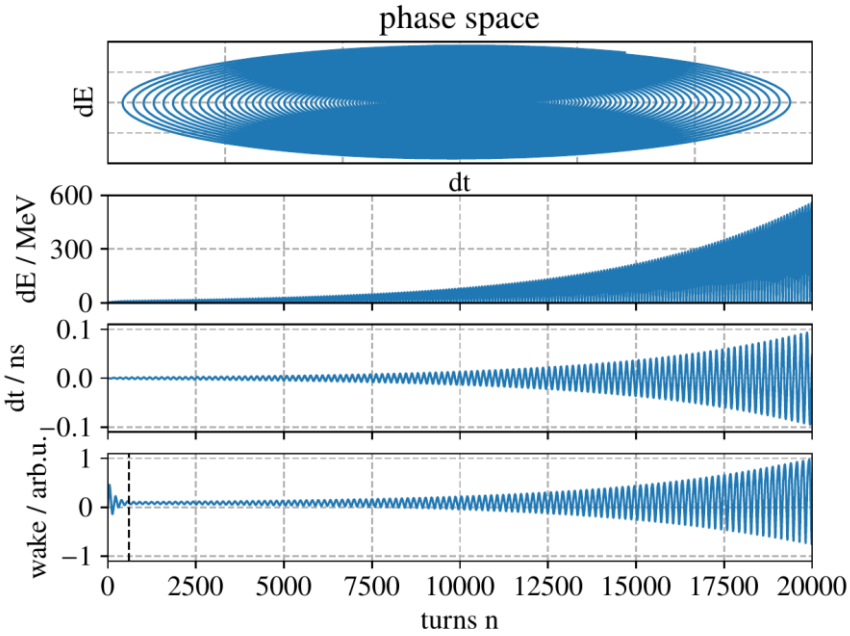

Figure 1: Exemplary numerical results without RF phase modulation. From top to bottom: The phase space of a single particle, the energy deviation dE (rms), the time deviation dt of the center of mass of the bunch and the value of the wake field in the cavity. The transient effect at the beginning is cut off to prevent it from distorting exponential fits (highlighted by a dashed black line).

Comparison of numerical and experimental results

For performance reasons, the emission of synchrotron radiation is completely neglected in the simulation. For this reason, only the growth rate τ_g^{-1} can be analyzed in contrast to the experiment where $\tau^{-1} = \tau_g^{-1} - \tau_d^{-1}$ is measured. Since the damping rate τ_d^{-1} does not depend on RF phase modulation parameters, it can be seen as a constant offset. Therefore, the results can still be compared with respect to the dependence on modulation amplitude, just the absolute values are expected to be different. As shown in Fig. 2, the experimental results of a quadratic dependence could be confirmed by numerical calculations.

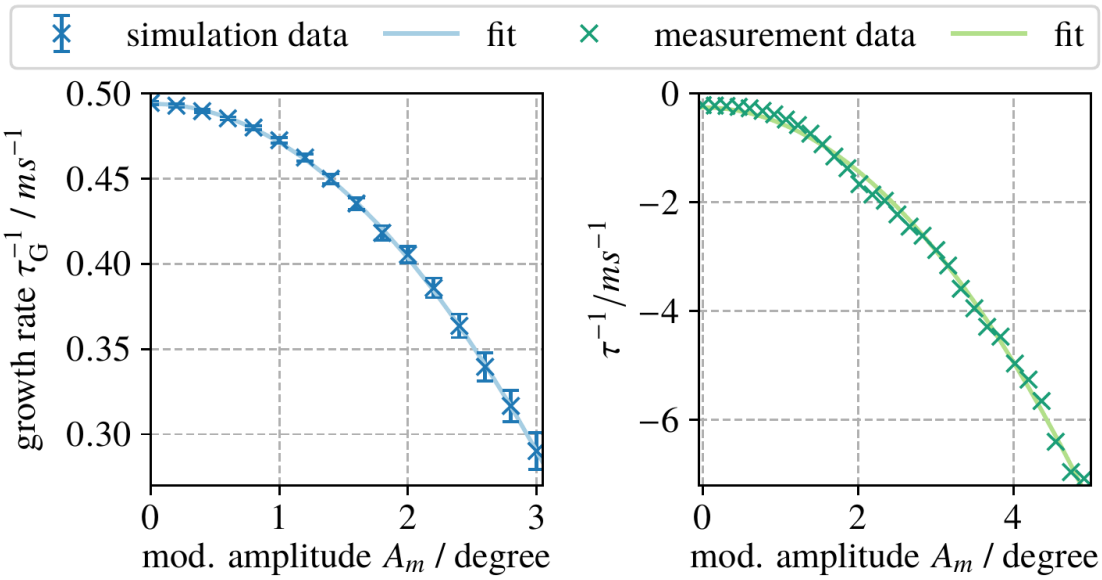

Figure 2: Comparison of simulation data (left) and measurement data (right) with corresponding quadratic fits.

References

[1] M. Sommer, et al., *Coupled-Bunch Instability Suppression Using RF Phase Modulation at the DELTA Storage Ring*, IPAC 2015, Richmond, VA, USA, 179.
[2] M. Sommer, et al., *Interaction of RF Phase Modulation and Coupled-Bunch Instabilities at the DELTA Storage Ring*, IPAC 2016, Busan, Korea, 1720.
[3] M. Sommer, et al., *Numerical Multiparticle Tracking Studies on Coupled-Bunch Instabilities in the Presence of RF Phase Modulation*, IPAC 2018, Vancouver, BC, Canada, 3511.
[4] M. Migliorati, *Multibunch and Multiparticle Simulation Code with an Alternative Approach to Wakefield Effects*, Phys. Rev. ST Accel. Beams 18 (2015), 031001.

Survey and Alignment of the DELTA Magnets and Vacuum Chamber

G. Schmidt, T. Dybiona, S. Khan, T. Schulte-Eickhoff
Zentrum für Synchrotronstrahlung (DELTA), Technische Universität Dortmund

Overview

The performance of a storage ring regarding beam lifetime, stability and injection efficiency depends on the alignment of all components. If the stored beam passes through the center of the quadrupole magnets, nonlinearities are minimized, the model of the magnetic optics is more accurate and the machine is easier to operate. During the last two years, all quadrupole magnets and vacuum chambers of the storage ring were realigned horizontally (see also [1]). The storage ring has now stabilized on a good beam lifetime, high orbit stability, reproducibility of magnet settings, improved injection efficiency and on a low radiation level in the DELTA hall.

Alignment of quadrupole magnets

The adjustment of quadrupole magnets was done using a Leica Absolute Tracker AT 402 for measuring the position of magnets before, during and after the adjustment of the quadrupole magnets. The quadrupole and vacuum chamber movement was in addition monitored with dial indicators (accuracy better than 0.01 mm). This allows to measure and visualize the movement of several components in real time whereas the tracker can only measure one point after another.
It was necessary to generate a reference coordinate system for the DELTA magnets which takes into account several boundary conditions. One of the constraints is that the quadrupole magnets cannot be adjusted longitudinally. Another one is that the length of the electron orbit should remain constant during the realignment.
First alignment steps indicated an orbit length change by moving the magnets to the target orbit. To compensate for this, it was decided to move the quadrupole magnets to an average displacement of 0.6 mm.
Measurements with stored beam have shown that the permanent injection bump is causing an orbit length change of approximately 4 mm compared to an orbit through the center of the quadrupoles. This deviation can explain the observed change of the orbit length if aligning to the simulated reference orbit passing through the center of quadrupoles.
A comparison of the measured radial quadrupole offsets with respect to the reference coordinate system before and after the adjustment is shown in Fig. 1.
After first tests it was decided to perform the radial adjustment in steps localized within up to five quadrupoles. This allowed to adjust the corresponding corrector magnet and to continue machine operation without time-consuming optimization. Several adjustment steps were done in the western part of the storage ring. The anticipated setting of the respective corrector magnet always allowed to store beam after an alignment intervention. User operation was possible at all beamlines without loss of intensity by retaining the orbit position. In order not to impair user operation, the magnets were moved in several steps to their final position. The experience with alignment steps of up to 1 mm was positive. All quadrupole magnets have reached their target position within ±0.3 mm.

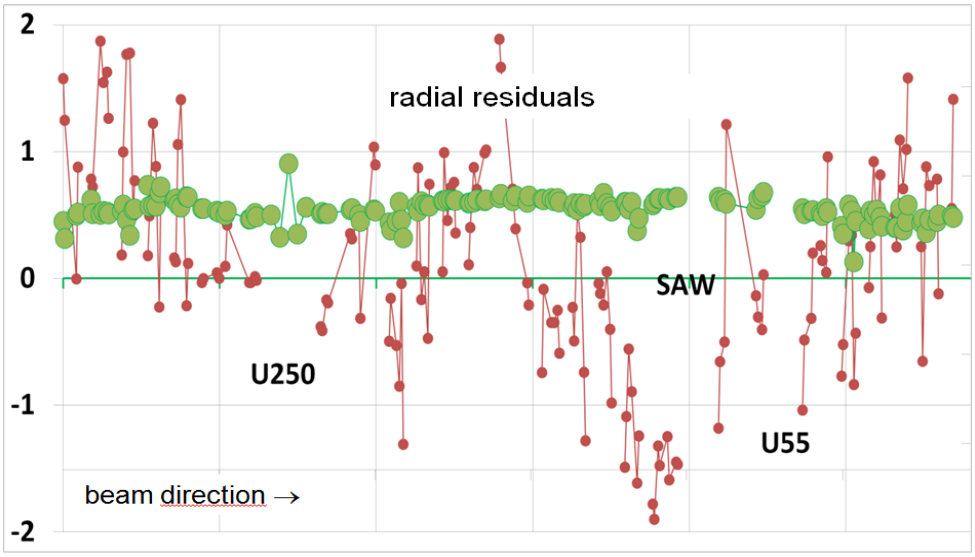

Figure 1: Radial displacement of quadrupole magnets before (red dots) and after the adjustment (green dots). Each magnet is equipped with two alignment marks shown as two dots. The measurement accuracy is ± 0.3 mm.

The undulator U250 has also been adjusted to the target position. The undulator U55 and the superconducting wiggler SAW will be the next insertion devices to be adjusted. The radial position of dipole magnets is less critical and will be corrected simultaneously with their longitudinal adjustment.

The wiggler beamlines were not sensitive to the horizontal adjustment of the quadrupole magnets. The U55 beamline was sensitive and first measurements were done to align the beamline to the electron reference orbit [2].

Outlook

The final goal of the alignment program is a stored electron beam passing through the centers of the aligned quadrupole magnet. Finally, sensitive beamlines, which have already been adjusted vertically, have to be aligned horizontally to the new electron reference orbit. At some places, the electron beam must still pass off-center through quadrupole magnets due to injection, lifetime and vacuum chamber heating reasons. If possible, further adjustment of the vacuum chambers will be done in these areas.

References

[1] G. Schmidt et al., *Survey and Alignment of the DELTA Magnets and Vacuum Chamber*, DELTA Annual Report 2017.

[2] U. Berges, private communication.

First Experience with Machine Learning Techniques in DELTA Controls

D. Schirmer
Zentrum für Synchrotronstrahlung (DELTA), Technische Universität Dortmund

Recently, artificial intelligence (AI) has experienced a renaissance in many fields. AI-based concepts are nature-inspired and can also be used in the field of accelerator controls. At DELTA, various studies on this subject have been carried out in the past [1-5]. Due to increasing computing performance and great advances in theoretical AI research as well as the availability of powerful AI programming frameworks, this works again met great interest and could be continued successfully.

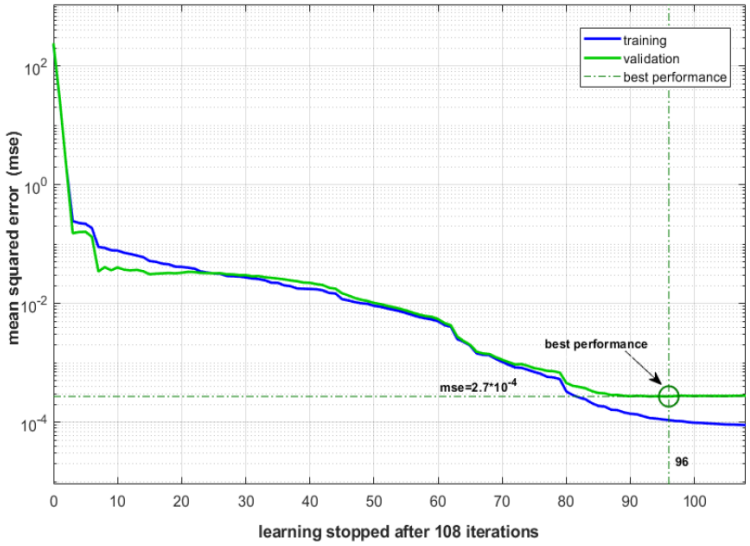

Figure 1: FFNN-supervised learning performance (mse) with approx. 1500 measured machine data records (orbit/steerer-data sets). Best validation performance (mse) of $2.7 \cdot 10^{-4}$ was reached after 96 training iterations of all records.

First studies and experiences were described in [6] and the papers cited therein. Among other possible applications, the use of neural networks for automated correction of the electron beam position (orbit control) is of interest. Machine learning (ML) simulations with a DELTA storage ring model were already successful [6]. Recently, conventional Feed-Forward Neural Networks (FFNN, see Fig. 2 left) were trained on the basis of real machine data (Fig. 1) in order to carry out local and global beam position corrections in the 1.5 GeV storage ring DELTA. First experimental results are promising.

Two completely different computing methods, single value decomposition (SVD) [7] and machine-learning-based, lead to comparable results (see Fig. 2, right). Nevertheless, there is still considerable potential for improvements. Further possible machine learning implementations are currently under consideration. For example, improving the electron transfer efficiencies from the linear accelerator to the booster synchrotron (BoDo) and from BoDo to the storage ring could be another demanding use case.

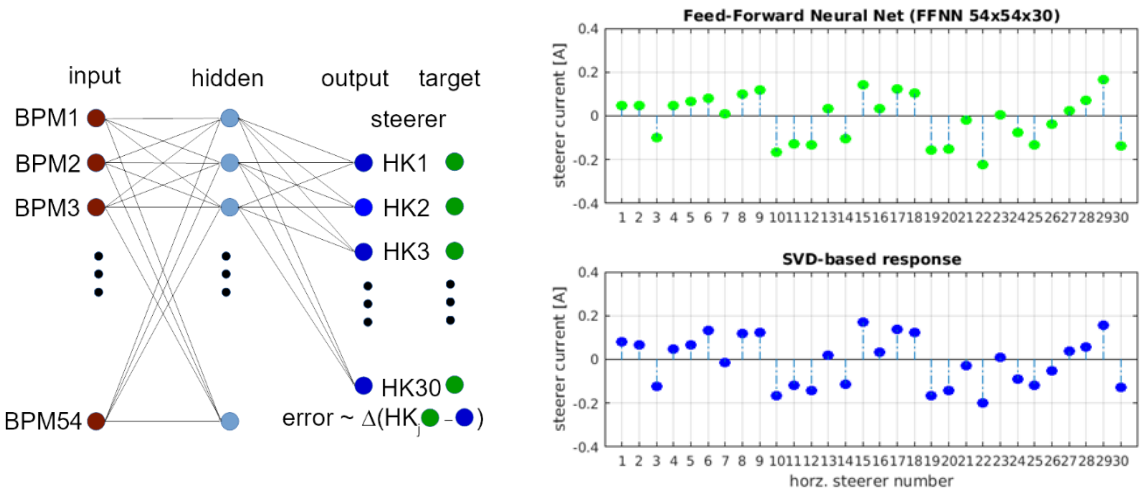

Figure 1: Left: Layout of the Feed-Forward Neural Network (FFNN 54x54x30) for horizontal orbit correction at DELTA. Right: Comparison of steerer strenght calculations based on singular-value decomposition (SVD, blue dots) and FFNN (green dots) after network training with real machine data. Both orbit correction techniques show very similar results.

References:

[1] C. Biermann, E. Wildner and A. Lüdeke, *A cybernetic machine for controlling and optimizing accelerator processes*, DELTA Internal Report, 1996, unpublished.
[2] D. Schirmer et al., Proc. PAC 1995, Dallas, USA, 1879.
[3] E. Zimoch, *Entwicklung und Einsatz eines intelligenten Agentensystems zur Optimierung der Injektion in den Speicherring der Synchrotronstrahlungsquelle DELTA*, Dissertation, TU Dortmund, 2003.
[4] D. Schirmer, *Electron Transport Line Optimization Using Neural Networks and Genetic Algorithms*, Proc. EPAC 2006, Edinburgh, Scotland, 1948.
[5] T. Buening, D. Mueller, *Entwurf und Vergleich unterstützender Systeme zur Verbesserung der Injektionseffizienz von DELTA, basierend auf Evolutionsstrategien und neuronalen Netzen*, Diploma Thesis, TU Dortmund, 2005.
[6] D. Schirmer, *Intelligent Controls for the Electron Storage Ring DELTA*, Proc. IPAC 2018, Vancouver, Canada, 4855.
[7] M. Grewe, *SVD-basierte Orbitkorrektur am Speicherring DELTA*, Dissertation, TU Dortmund, 2005.

Photocathode Gun Cavity for an Electron Gun for Ultrafast Electron Diffraction at DELTA

D. Krieg[+], S. Khan[+], K. Sokolowski-Tinten[*], T. J. Albert[*]

[+] Zentrum für Synchrotronstrahlung (DELTA), Technische Universität Dortmund
[*] Fakultät Physik, Universität Duisburg-Essen

Introduction

Ultrafast electron diffraction (UED) is a technique to study the structural dynamics of matter, combining diffraction of electrons with sub-angstrom De-Broglie wavelength with femtosecond time resolution. UED pump-probe experiments require ultrashort laser pulses to pump a sample, electron bunches with small emittance and ultrashort length to analyze the state of the sample by diffraction and excellent control of the delay between them. Electrons accelerated to a few MeV in a radiofrequency (RF) photocathode gun offer significant advantages, compared to keV electrons from electrostatic electron sources, regarding emittance and bunch length due to the reduction of space charge effects. Furthermore, the longer mean free path of MeV electrons allows for thicker samples and hence a broader range of possible materials. The goal of the project UED@DELTA is to design a university-based UED facility with ultrashort and low-emittance MeV electron bunches at DELTA. The basis of this design is a photocathode gun cavity.

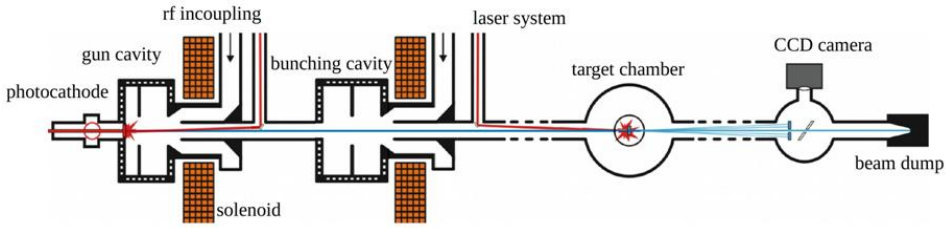

Figure 1: Basic design of an electron source for ultrafast electron diffraction.

Comparison of different gun cavities

The basic design of an electron source for UED is shown in Fig. 1. Electrons are emitted by a laser pulse from the photocathode which placed inside a 1.5-cell gun cavity. The most important factor for the acceleration and beam dynamics is the on-axis longitudinal electric field $E_z(z)$. Cavities with varying geometries and RF frequencies f will lead to different $E_z(z)$. The maximum gradient $E_0=\max(E_z)$ is typically located at the cathode to rapidly accelerate the electrons and efficiently suppress space charge effects, since these scale as $1/\gamma^2$, where γ is the Lorentz factor [1]. The electric fields $E_z(z)$ for existing gun cavities, e.g. [2,3], are shown in Fig. 2 and for two idealized cases in Fig. 3. To evaluate the longitudinal momentum gradient dp_z/dt, electrons are tracked numerically through these cavities for two gun phases φ_E and φ_{SPC}, where φ_E maximizes the energy gain and φ_{SPC} the gradient at the cathode. The results of these simulations are also shown in Fig. 2 and 3.

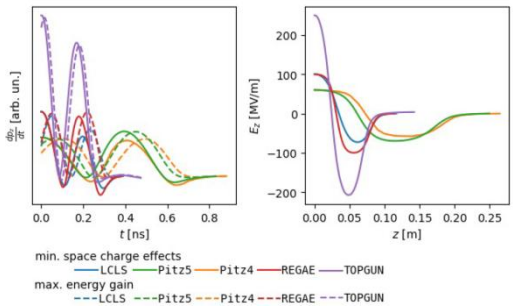

Figure 2: Electric field component $E_z(z)$ of different existing cavities and resulting gradient of $p_z(t)$.

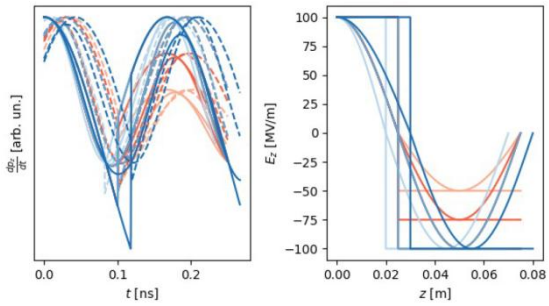

Figure 3: Electric field component $E_z(z)$ for two idealized cases with resulting gradient of $p_z(t)$.

The REGAE [3] and the LCLS cavity yield the high gradients but the REGAE cavity should be preferred because of its RF incoupling scheme. While at LCLS a side-coupling is chosen, at REGAE the RF power is coupled in coaxially to reduce a growth of emittance. Former investigations [4] showed that a frequency f = 3 GHz yields the best compromise between the suppression of space charge effects and nonlinearities in longitudinal phase space, which are limiting bunch length and emittance. For higher frequencies, the dimensions of the cavity will be smaller and thus more susceptible to manufacturing inaccuracies. Space charge effects can be suppressed independent of the gun cavity by increasing the laser pulse length, but then a rebunching cavity is needed, which is operated off-crest. The nonlinearities in the longitudinal phase space can be highly reduced by a linearization scheme known as stretcher mode [5]. In this scheme, the cavity parameters are chosen in such a way that the electron bunch is expanding longitudinally after the gun and is rebunched in the second cavity. As a consequence, a gun cavity with high acceleration gradient near the cathode is needed and with a careful choice of parameters the achievable bunch length and emittance is mainly limited by the nonlinearities, which can be highly reduced with the stretcher mode. As a result, the REGAE design appears to be the best choice for the planned UED facility and a rebunching cavity will be needed.

References

[1] M. Ferrario et al., *Space Charge Effects*, Rep. CERN-2014-009, 331.

[2] A. Cahill et al., *RF design for the TOPGUN photogun: A cryogenic normal conducting copper electron gun*, Nucl. Instrum. Methods A 865 (2017), 105.

[3] V. Paramonov et al., *Design of an L-band normally conducting RF gun cavity for high peak and average RF power*, Nucl. Instrum.Methods A 854 (2017), 113.

[4] D. Krieg et al., *First conceptual design studies of an electron source for ultrafast electron diffraction at DELTA*, in Proc. of IPAC 2017, Vancouver, Canada, 4530.

[5] B. Zeitler et al., *Linearization of the longitudinal phase space without higher harmonic field*, Phys. Rev. ST Accel. Beams 18 (2015), 120102.

Estimate of the Spectral Bandwidth of Tunable THz Radiation at DELTA

N. Neumann[1], C. Mai[2], M. Brosi[3], F. Frei[4], C. Gerth[5], S. Khan[2], M. Laabs[1], A. Meyer auf der Heide[2], D. Plettemeier[1], J. Steinmann[4]
[1]TU Dresden, Germany, [2]TU Dortmund, Germany, [3]KIT Karlsruhe, Germany,
[4]PSI Villigen, Switzerland, [5]DESY Hamburg, Germany,

Overview

The measurement and control of the bunch length in a free-electron laser like the European XFEL or SwissFEL is essential for the operation of this kind of light source. The spectrum of coherent THz radiation is a good measure for the longitudinal electron bunch shape and has formerly been studied using scanning spectrometers [1] which allow to measure an averaged bunch shape. However, this method neglects shot-to-shot variations which are inherent to linear accelerators.

Figure 1: Photograph of the detector readout board holding eight THz detector elements. The chip layout with antennas providing narrowband sensitivity between 50 GHz and 700 GHz is shown on the lower right.

Estimate of the THz source bandwidth

A single-shot detector for spectral fingerprint measurements was developed by TU Dresden. This device is a Schottky-diode-based on-chip spectrometer measuring 2.4 mm by 1.4 mm and featuring eight narrowband detector elements in the range from 50 GHz to 700 GHz (Fig. 1). In contrast to other THz detectors it is operated at room temperature while still offering a good sensitivity [2].

At DELTA, the generation of narrowband THz radiation was first tested in 2014 and is routinely used since 2017 [4,5]. The source relies on an interaction between an intensity-modulated laser pulse and the electrons in the storage ring. It offers tunable radiation in the range from 50 GHz to 6 THz and a theoretically estimated minimum bandwidth of about 58 GHz at low frequencies.

For a characterization of THz detectors it is important to determine their spectral response. Assuming a tunable source with a central frequency f_c and unknown, but limited, bandwidth, the measured combined spectral response R_{det} of detector and source reads

$$R_{\mathrm{det}}(f) = \int_{-\infty}^{\infty} h_{src}(f', f = f_c) \cdot h_{\mathrm{det}}(f') \cdot df' \qquad (1)$$

This function has been measured by acquiring THz detector output signals during sweeps of the central frequency of the THz source.

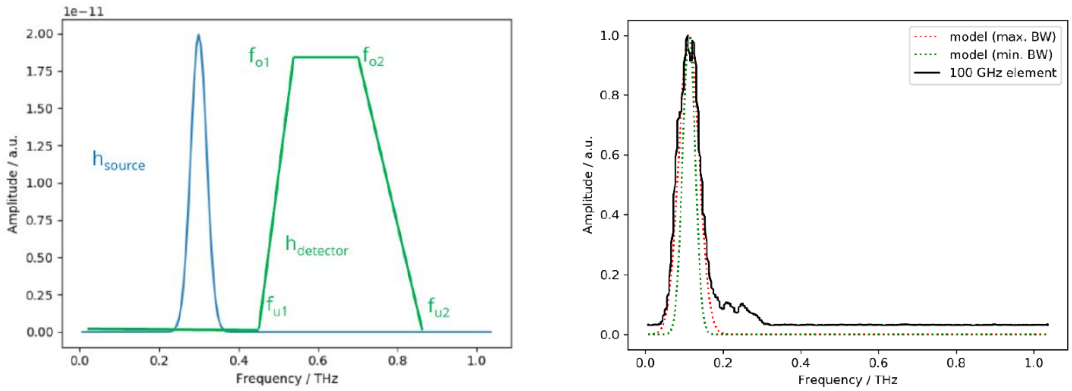

Figure 2: Left: Simplified model of detector and source response. Right: Measured (solid) and calculated (dotted) detector response for the 100 GHz element (f_{u1}=95 GHz, f_{o1}=100 GHz, f_{o2}=125 GHz, f_{u2}=130 GHz) with minimum (green) and maximum (red) source bandwidth.

Figure 2 (left) shows a simplified model of the convolution integral R_{det}. Here, the source response h_{src} is assumed to have a Gaussian shape and the detector response h_{det} is assumed to be a piecewise linear function. An experimental minimum and maximum source bandwidth were estimated assuming a Heaviside-like detector response and a Dirac-like response, respectively. Inverting R_{det} numerically leads to a minimum bandwidth B_{min} = 35 GHz (FWHM) and a maximum source bandwidth B_{max} = 59 GHz (FWHM) which is consistent with the theory [4]. With the estimated source bandwidth and applying equation (1), the detector characteristics can be modeled, as shown in Figure 2 (right).

Outlook

Further analysis of the data will yield a better understanding of the spectral response of the novel detector developed in Dresden. A more precise estimate of the source bandwidth is conceivable with a known detector response, e.g., taking advantage of the well-defined cutoff behavior of waveguide-coupled detectors. A detailed characterization of detectors will help to match detector properties to experimental needs for the application at accelerators with ultra-short electron bunches.

References

[1] L. Fröhlich et al., *Bunch length measurements using a Martin-Puplett interferometer at the VUV-FEL*, Proc. FEL 2005, Palo Alto, USA, 114.

[2] M. Laabs et al., *On-chip THz spectrometer for bunch compression fingerprinting at fourth-generation light sources*, J. Synchrotron Rad. 25 (2018), 1509.

[3] M. Schiselski et al., *A planar Schottky diode based integrated THz detector for fast electron pulse diagnostics*, International Microwave Symposium IMS 2016, San Francisco, CA, USA.

[4] P. Ungelenk et al., *Studies of Ultrashort THz Pulses at DELTA*, Proc. IPAC 2014, Dresden, Germany, 1936.

[5] P. Ungelenk et al., *Continuously tunable narrowband pulses in the THz gap from laser-modulated electron bunches in a storage ring*, Phys. Rev. Accel. Beams 20 (2017), 020706.

[6] C. Mai et al., *A Tunable Narrowband Source in the Sub-THz and THz Range at DELTA*, IPAC 2018, Vancouver, 4534.

Estimate of the Beam Energy Spread at the Short-Pulse Facility

A. Meyer auf der Heide, B. Büsing, S. Khan, D. Krieg, C. Mai, B. Riemann, F. Teutenberg
Zentrum für Synchrotronstrahlung (DELTA), Technische Universität Dortmund

Overview

The DELTA short-pulse facility [1] is based on coherent harmonic generation (CHG) [2]. Figure 1 shows the CHG scheme (left) and the layout of the facility (right). Seeding the electron bunches with femtosecond 800-nm or 400-nm laser pulses leads to microbunching and coherent emission of ultrashort pulses at harmonics of the laser wavelength. Further downstream, a gap in the longitudinal electron distribution gives rise to coherent emission of terahertz (THz) radiation. The power of the CHG pulses is described by

$$P_{coh} \propto \left(\frac{N}{n^{\frac{1}{3}}} \exp\left(-\frac{n^2}{2A^2}\right)\right)^2.$$

Here, N is the number of electrons, n is the harmonic number, and $A = \Delta E/\sigma_E$ is the energy modulation amplitude with the natural electron energy spread σ_E.

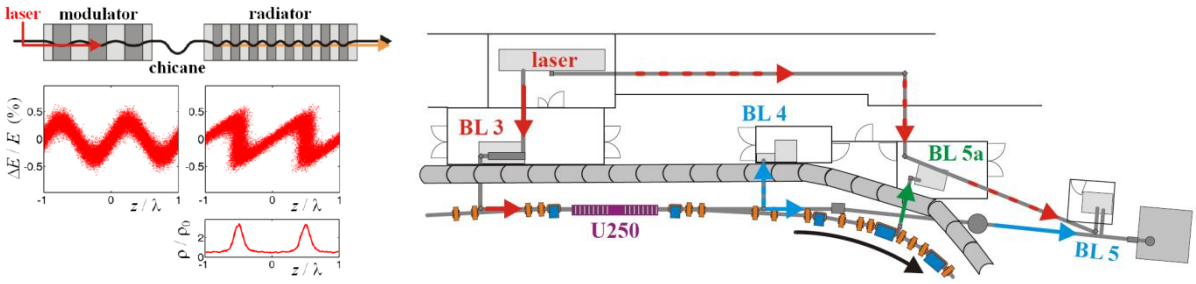

Figure 1: Left: CHG principle with laser-induced energy modulation in an undulator (modulator) converted into periodic microbunching by a magnetic chicane and coherent emission at laser harmonics in a second undulator (radiator). Right: Layout of the DELTA short-pulse facility with femtosecond laser system, laser beamline BL 3, undulator U250 (comprising modulator, chicane and radiator), diagnostics beamline BL 4, the soft-X-ray beamline BL 5 operated by the Forschungszentrum Jülich, and the dedicated THz beamline BL 5a.

CHG in the presence of RF phase modulation

In standard user operation at DELTA, a routinely applied phase modulation of the accelerating radiofrequency (RF) results in a decrease of the average electron density while increasing the beam lifetime. In the case of laser-induced energy modulation, the electron density and, thus, the number of electrons participating in the energy modulation as well as the electron energy spread σ_E change periodically. By introducing a lengthening factor s which transforms $N \rightarrow N/s$ and $\sigma_E \rightarrow \sigma_E/s$ and, thus, $A \rightarrow A \cdot s$, the emitted CHG power transforms to $P_{coh} \propto \left(\frac{N}{s n^{1/3}} \exp\left(-\frac{n^2}{2s^2A^2}\right)\right)^2$. With an oscillating s caused by the RF phase modulation, also the CHG power oscillates.

Estimating the electron energy spread

An evaluation of the modified formula for the CHG power P_{coh} with different modulation amplitudes $A = \Delta E/\sigma_E$ shows different types of oscillation. For large A, the emitted power is largest at phases with a small s which corresponds to a higher electron density but also to a larger energy spread. For smaller amplitudes, the behavior reverses. The THz signal, however, does not change its behavior, as it mainly requires a small energy spread. In the intermediate region between large and small modulation amplitudes, for example at $A = 3.3$ (see Fig. 2, right), the CHG signals tends to oscillate twice as often. Here, a combination of reduced electron density but also reduced energy spread appears to be better than either a minimum energy spread or a maximum electron density.
In combination with routinely performed chicane scans (see Fig. 2, left) which allow a measurement of the modulation amplitude $\Delta E/E$, an estimate of the relative energy spread of $\frac{\sigma_E}{E} = \frac{\Delta E}{E}/A \approx 1.2 \cdot 10^{-3}$ can be calculated. This result is almost twice as high as the natural energy spread of $7 \cdot 10^{-4}$ according to the design lattice of DELTA. A possible influence of the RF phase modulation on the energy spread requires further investigations.

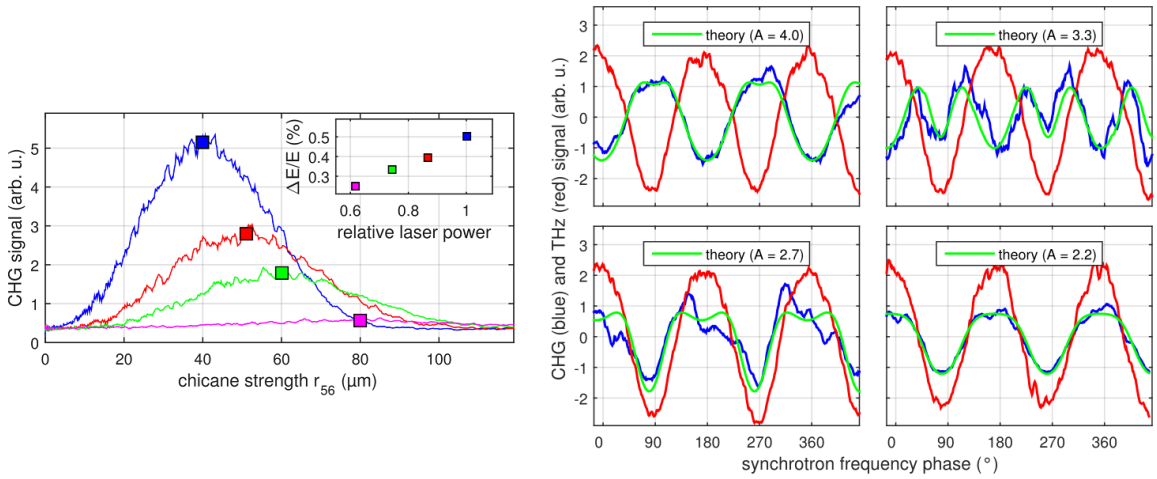

Figure 2: Left: CHG signal versus chicane strength for different laser pulse energies. The inset shows the corresponding relative modulation amplitude. Right: Laser-induced THz (red) and CHG (blue) signals (mean values subtracted) under the influence of an RF phase modulation as function of the synchrotron frequency phase and theoretical CHG signals (green) for different energy modulation amplitudes A.

References

[1] S. Khan et al., *Generation of Ultrashort and Coherent Synchrotron Radiation Pulses at DELTA*, Sync. Rad. News 26:3 (2013), 25.
[2] B. Girard et al., *Optical Frequency Multiplication by an Optical Klystron*, Phys. Rev. Lett. 53 (1984), 2405.
[3] G. Stupakov, *Beam Echo Effect for Generation of Short-Wavelength Radiation*, Proc. of FEL 2009, Liverpool, United Kingdom, 15.
[4] A. Meyer auf der Heide et al., *Measurement of the Laser-Induced Energy Modulation Amplitude at the Short-Pulse Facility at DELTA*, Proc. of IPAC 2018, Vancouver, Canada, 4538.

Reducing the Momentum Compaction Factor of the Storage Ring at DELTA Based on Simulations with a New Lattice Model

Andreas Glassl, Stephan Kötter, Carsten Mai, Malte Sommer, Benjamin Isbarn, Thomas Weis
Zentrum für Synchrotronstrahlung (DELTA), Technische Universität Dortmund

A new lattice model *del018* [1] of the DELTA storage ring was developed in MAD-X [2] based on the older model *del008* [3]. The new model incorporates changes to magnet positions of the storage ring lattice resulting from an ongoing effort to realign the magnetic centers of the quadrupoles with the closed orbit [4]. Among other changes, fringe fields of the dipoles were added to the new model and the effective lengths of the quadrupoles were reevaluated as well.

The new model was able to replicate the length of the orbit determined from the RF frequency and the transverse tunes as measured with the kicker-based tune measurement system of DELTA [5]. Optical functions determined by applying the COBEA algorithm [6] to a measured orbit-response matrix revealed an asymmetry which the model did not match. This issue was corrected in an effort to create a more realistic model by fitting the beta functions produced by the model to the beta functions produced by COBEA.

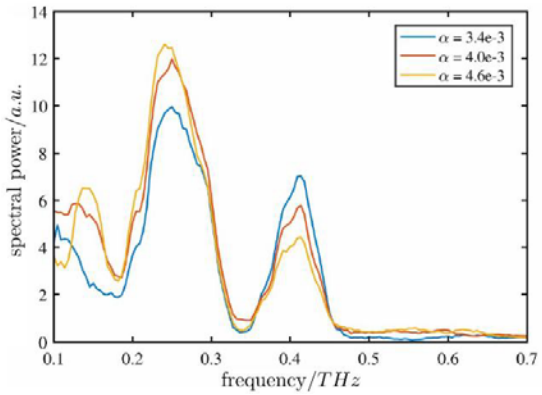

Figure 1: Spectral power at the THz beamline before (yellow) and after reduction (red and blue) of the momentum compaction factor.

The fitted model was used to simulate a quadrupole setting which reduced the momentum compaction factor of the storage ring by increasing the quadrupole field strengths of the QF01 family and reducing the quadrupole field strength in the remaining quadrupoles in the arcs of the storage ring to keep the tune fixed. This setting was successfully tested and achieved a bunch length reduction of 20 % [1]. The spectral power of the THz beamline [7] in the regime of 400 GHz was increased by ~40 % (Fig. 1).

Future applications of the model may include fine-tuning of the quadrupole setting to achieve an even shorter bunch length or to control the power distribution at the THz beamline to a better extent [1].

References:

[1] A. Glassl, *Optiksimulation an DELTA*, Master Thesis, TU Dortmund (2018).
[2] O. Kopitetzki, *Vermessung und Modellierung der Optik des Speicherrings DELTA,* Dissertation (2005).
[3] Hans Grote et al., *The MAD-X Program*, Version 5.03.04, User's Reference Manual.

[4] G. Schmidt et al., *Survey and Alignment of the DELTA Magnets and Vacuum Chamber*, DELTA Annual Report 2017.
[5] P. Hartmann et al., *Kicker Based Tune Measurement System for* DELTA, Proc. DIPAC 2007, Venice, Italy, 277.
[6] B.Riemann, *The bilinear-exponential closed-orbit model and its application to storage ring beam diagnostics,* Dissertation, TU Dortmund (2016).
[7] C. Mai, *A Tunable Narrowband Source in the Sub-THz and THz Range at DELTA,* Proc. IPAC 2018, Vancouver, Canada, 4535.
[8] C. Mai, private communication (2018).

Progress towards EEHG at the DELTA Short-Pulse Facility

B. Büsing, S. Khan, C. Mai,
A. Meyer auf der Heide, B. Riemann, M. Schmutzler
Zentrum für Synchrotronstrahlung (DELTA), Technische Universität Dortmund

Overview

Echo-enabled harmonic generation (EEHG) is a seeding scheme for free-electron lasers proposed in 2009 [1]. As shown in Fig. 1 (left), it is based on a twofold laser-induced modulation of the energy of relativistic electrons. Test experiments were conducted at SLAC in the USA and SINAP in China [2,3]. EEHG is also proposed as a method to generate ultrashort pulses in storage rings [4,5]. Compared to coherent harmonic generation (CHG) presently employed at the DELTA short-pulse facility [6], EEHG will enable coherent emission at higher harmonics of the laser wavelength. DELTA is presently the only storage ring worldwide at which the implementation of EEHG is planned.

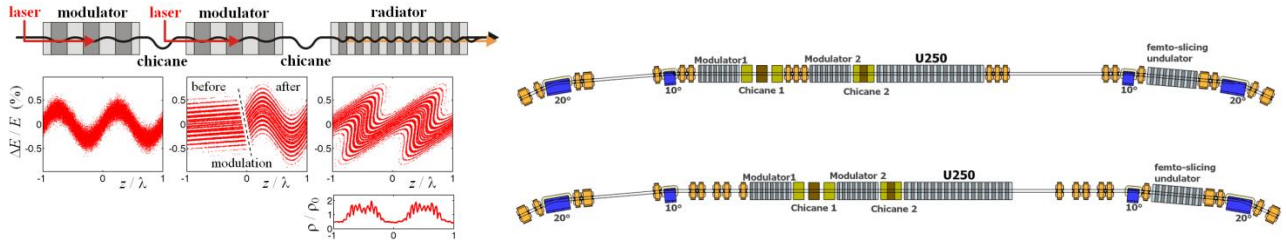

Figure 1: Left: EEHG principle with twofold laser-induced energy modulation in two undulators (modulators) converted into microbunching by magnetic chicanes and coherent emission at high laser harmonics in a third undulator (radiator). Right: Two possible future configurations of the northern part of the DELTA storage ring with a 20 m long straight section for EEHG [7].

Magnetic lattice of the storage ring

Currently there are two possible magnet configurations containing a 20m long straight section to implement EEHG in the northern part of the DELTA storage ring, shown in Fig. 1 (right). Both with moderate beta functions, zero dispersion in the straight section and large dynamic aperture [7][8]. Beam dynamics simulations such as “tune shift with amplitude” and stability studies including misalignments and multipole errors are ongoing work.

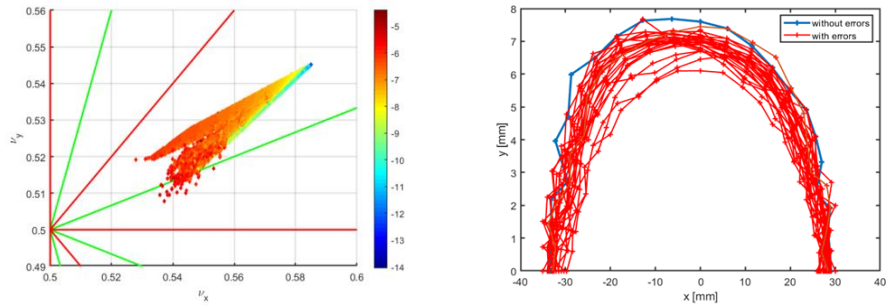

Figure 2: Left: Tune shift with amplitude in a tune diagram with color-coded diffusion rate. Right: Dynamic aperture (right) without errors (blue) and for 25 seeds of misalignment errors (red).

Simulation of designs for magnetic chicanes

The EEHG scheme requires two different chicanes, one strong and one weak. Two designs of chicanes with three and four dipole magnets were investigated, taking into account in particular the maximum available space and the horizontal deflection of the electron beam [9].

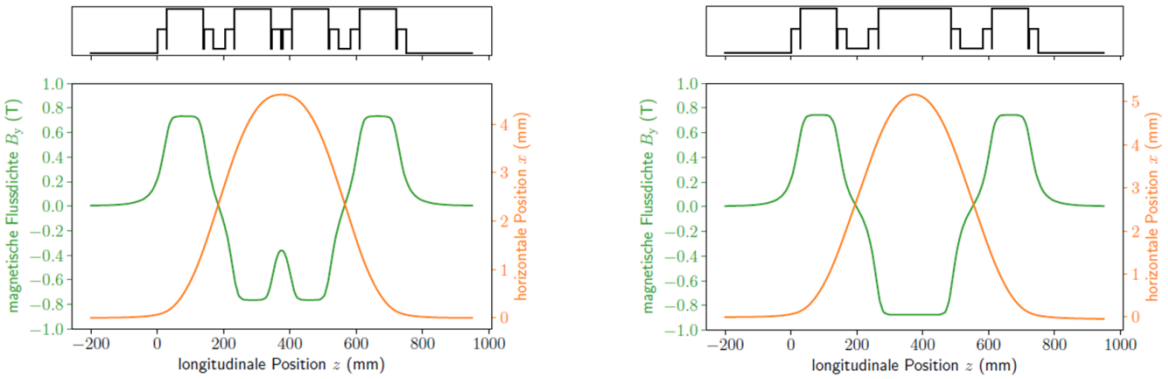

Figure 3: Magnetic field strength and horizontal deflection for a four dipole chicane (left) and three dipoles (right) [9].

Hardware

For the implementation of EEHG at DELTA, two new electromagnetic modulators (period length 200 mm, 7 periods) are already in house and tested [10] while the present U250 undulator (period length 250 mm, 17 periods) will be employed as radiator. Vacuum chambers for the modulators are currently manufactured and new dipole chambers were designed [7].

References

[1] G. Stupakov, *Using the Beam-Echo Effect for Generation of Short-Wavelength Radiation*, Phys. Rev. Lett. 102, 074801 (2009).

[2] Z. Zhao et al., *First lasing of an echo-enabled harmonic generation free-electron laser*, Nature Photonics 6, 360 (2012).

[3] E. Hemsing et al., *Echo-enabled harmonics up to the 75th order from precisely tailored electron beams*, Nature Photonics 10, 512 (2016).

[4] C. Evain et al., *Soft x-ray femtosecond coherent undulator radiation in a storage ring*, New J. Phys. 14, 023003 (2012).

[5] R. Molo et al., *EEHG and Femtoslicing at DELTA*, Proc. FEL 2013, New York, USA, 594.

[6] S. Khan et al., *Generation of Ultrashort and Coherent Synchrotron Radiation Pulses at DELTA*, Sync. Rad. News 26:3, 25 (2013).

[7] B. Büsing, *Teilchenoptische Auslegung und Entwicklung von Dipolkammern für die EEHG-basierte Kurzpulsquelle bei DELTA*, Master Thesis, TU Dortmund (2017).

[8] J. Bengtsson, Moptima AB, Lund, Sweden.

[9] M. Schmutzler, *Dispersive Magnetstrukturen für die Erzeugung ultrakurzer Strahlungspulse bei DELTA*, Master Thesis, TU Dortmund (2018).

[10] D. Zimmermann, *Aufbau eines Magnetmessstandes zur Feldvermessung von Undulatoren bei DELTA*, Master Thesis, TU Dortmund (2016).

A new deep x-ray lithography setup for large wafer exposure at BL1 of DELTA

Sebastian Leese[1], *Thorsten Witt*[1], *Georg Jülicher*[1], *Jennifer Bolle*[1], *Tanja Schulte-Eickhoff*[1], *Christian Sternemann*[1], *Michael Paulus*[1], *Metin Tolan*[1], *Ottó Markus*[2]
[1] *Fakultät Physik / DELTA, Technische Universität Dortmund, 44221 Dortmund, Germany*
[2] *microworks GmbH, 76344 Eggenstein-Leopoldshafen, Germany*

X-ray imaging for medical use demands large gratings that can not be produced with the existing x-ray lithography scanner DEX01 at beamline BL1 of the DELTA synchrotron radiation source. Therefore, a new lithography setup for wafers with a length up to 450 mm and a maximum width of 100 mm was implemeted and commissioned at BL1 in cooperation with the company *microworks*.

After survey of the experimental hutch of beamline BL1 using a FARO-Prime system, a three dimensional construction drawing of the planned setup was created considering the spacial limitations of the hutch as well as of the existing lithography scanner. The main component of the new setup is a high precision linear stage that was mounted on special cross sectional profiles to allow vibration-free movement. A holder for wafer and lithography mask was developed based on a 10 mm thick aluminium plate that was fixed to the linear stage allowing for a high precision vertical movement of large wafers for x-ray exposure. In order to make the setup as simple as possible, it works at ambient conditions in air atmosphere. By minimizing the x-ray path through air and using a filter to suppress the high energy part of the white x-ray beam, the production of ozone is minimized which is controlled by corresponding ozone sensore inside the experimental hutch. The beryllium window that seperates the experimental hutch from the DELTA vacuum is protected against ozone by controlled constant helium flow. The linear stage is moved by a stepper motor that is controlled by an arduino board. Limit switches for hardware security and for calibration of motor position were implemented. The exposures of the wafers are performed via a program package, that determines the dose applied to the wafer via read out of the DELTA beam current and control of the motor speed. The exposure can be initiated using a control board available at BL1. For the post exposure bake of the large wafers two hotplates were combined with a copper plate. The bake procedure was optimized by analysing sequences of infrared photos of the copper plate during annealing circles.

This lithography setup for large wafer exposure (see figure 1) was successfully tested after commissioning with 200 mm long substrate covered with a several hundred μm thick epoxy based x-ray resist. Thereby structures (see figure 2) were produced that allow production of microparts of high quality for industrial applications. Further investigations are planned in order to be able to appreciate the full potential of the new setup.

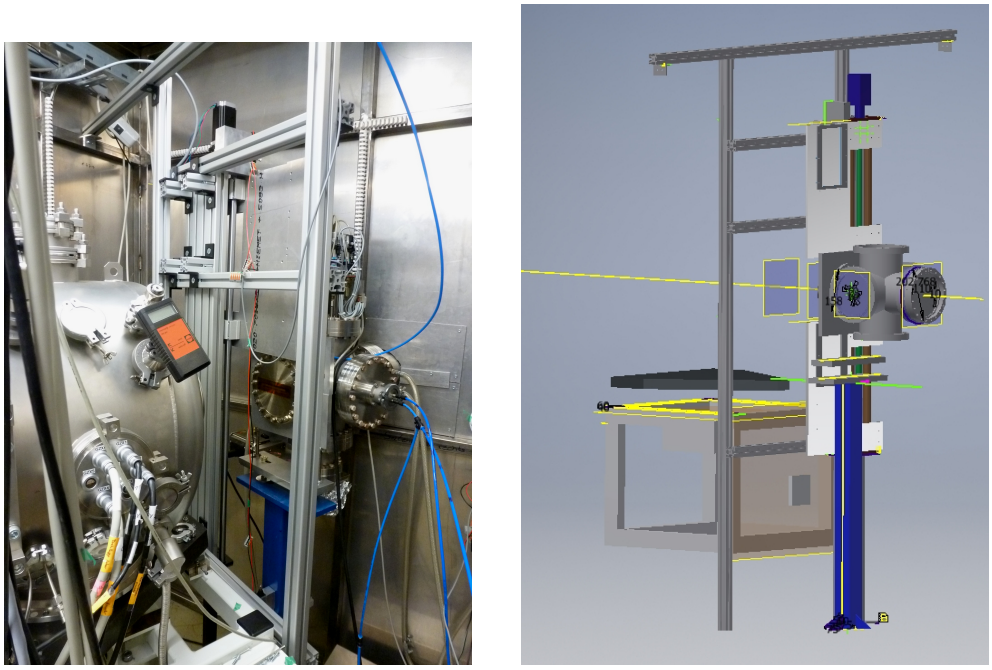

Figure 1: New deep x-ray lithography setup at BL1 of DELTA. Left: photograph[1]; Right: construction drawing

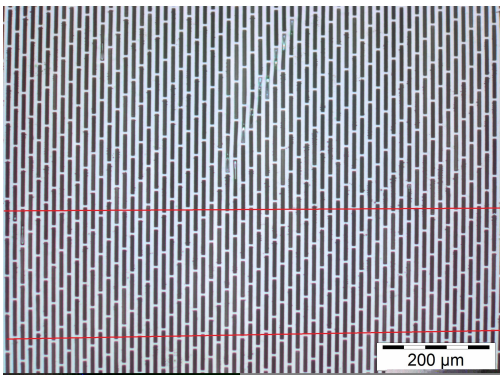

Figure 2: Microscope image of a large wafer with mean periode $< P >= (14,85 \pm 0,07)\,\mu$m (markers: analysed periodes)[1]

References

[1] S. Leese. Röntgenlithographie für großflächige Belichtungen an der Strahllinie BLl bei DELTA, 2018. Dortmund.

Commissioning of a von Hamos spectrometer for X-ray emission spectroscopy at beamline BL9

Robin Sakrowski[1], Christian Sternemann[1], Florian Otte[2], Max Wilke[3] and Metin Tolan[1]

[1] Fakultät Physik/DELTA, TU Dortmund, 44221 Dortmund, Germany
[2] FXE Instrument, European XFEL GmbH, 22869 Schenefeld, Germany
[3] Institut für Erd- und Umweltwissenschaften, Universität Potsdam, 14476 Potsdam-Golm, Germany

In this experiment a wavelength dispersive von Hamos spectrometer (made by JJ X-ray) designed for high resolution X-ray emission spectroscopy (XES) was commissioned and tested at beamline BL9 of DELTA.
XES provides valuable insight to the electronic structure of atoms and molecules being especially sensitive to spin state and coordination changes. Of particular interest here are the $K\beta_{1,3}$ emission lines and the valence-to-core (vtc) emission of 3d transition metals like iron, cobalt, and manganese. Within this commissioning run we measured emission spectra of iron [1] in FeO, synthetic fayalite (Fe_2SiO_4) as well as of two different iron containing metal-organic frameworks. As calibration sample we used an iron foil. The oxidation state of iron in FeO and Fe_2SiO_4 was assigned as Fe^{2+}. The iron is octahedrally coordinated by six oxygen atoms in both samples.

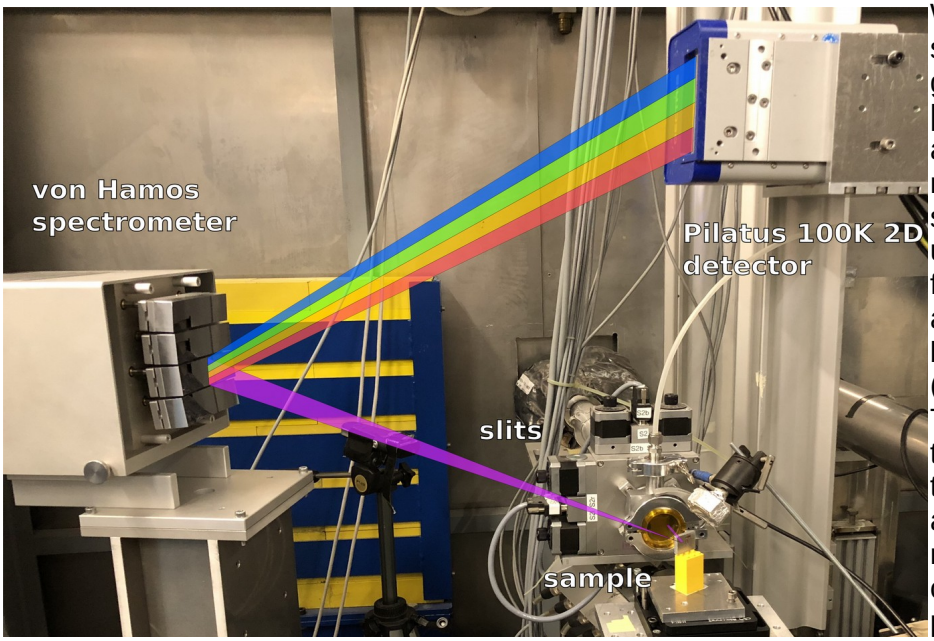

Fig.1: A wavelength dispersive von Hamos spectrometer in near 90° geometry with cylindrical bent Si (220) crystals and Pilatus 100K 2D detector recording the emission spectra at BL9.

We utilized the von Hamos spectrometer in a near 90° geometry as described in [2] to measure the $K\beta_{1,3}$ and vtc X-ray emission signal, from different iron samples described above, using the (440) Bragg-reflection around 65° Bragg-angle with four cylindrically bent Si (220) crystals (bending radius 0.5 m). Therefore, the distance of the von Hamos crystals to the axis between sample and detector was set to 0.5 m to achieve optimized focusing in the horizontal plane. A pre-alignment was carried out by scattering the laser light on a Kapton foil and optimizing the signal from each crystal. The detector was placed 0.44 m above the sample, with the spectrometer half the height. The incident monochromatic beam had an energy of 7300 eV with a spot size of 1.5 x 1.5 mm (v x h). The Pilatus 100K 2D detector has an active area of 83.8 x 33.5 mm^2 and we achieved a spectral bandwidth of 190 eV with an estimated overall energy resolution of 4.9 eV (FWHM of the elastic lines at different energies from 7000 to 7120 eV). This configuration would allow parallel detection of the Fe Kβ and vtc XES signal simultaneously.
For future experiments with this setup a higher focusing in the vertical plane (0.2 mm beam height) should be used to achieve an energy resolution up to 0.7 eV.

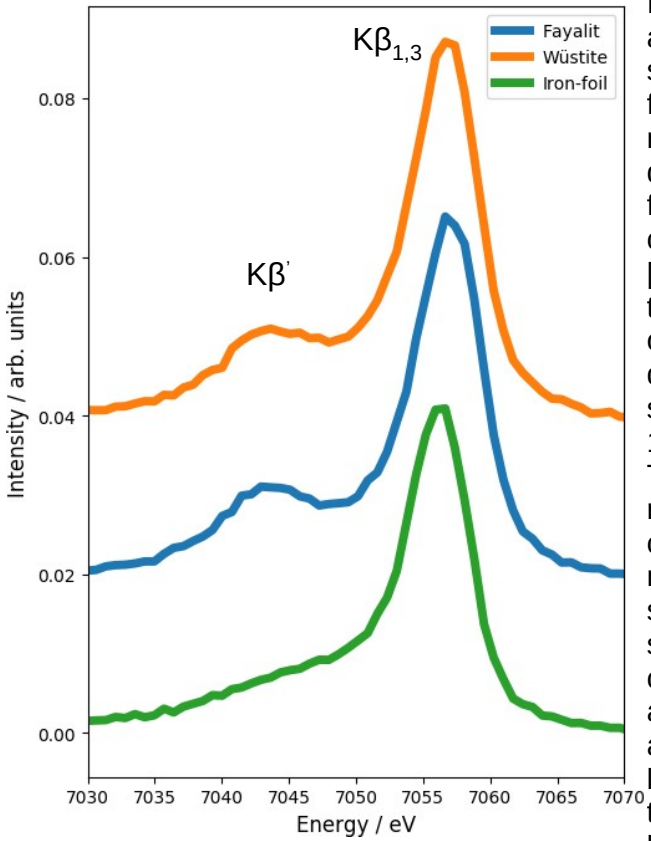

Fig. 2: X-ray emission signal summed for all crystals, normalized and shifted by a constant factor in y. Fe_2SiO_4 (blue), FeO (orange), iron-foil (green). At ~7043 eV the Kβ' feature arises as an indicator for the high-spin state.

In Fig. 2 the measured and normalized (to the area in between 7000-7120 eV) spectra are shown and one can clearly distinguish the Kβ' feature around 7043 eV as well as the $Kβ_{1,3}$ mainline. Latter corresponds to an electric dipole allowed 3p-1s transition with contributions from 3p-3d exchange as well as 3p spin-orbit coupling, known to be sensitive to the spin state [3]. The decrease in both Kβ' intensity and splitting between the Kβ' and $Kβ_{1,3}$ feature in iron is observed as the nominal spin at the metal is reduced. The exposure times were 2000 s for the synthetic fayalite sample, 200 s for FeO and 1000 s for the iron-foil.

The signal from the valence-to-core excitation is roughly sixty times weaker than the mainline contribution and is assigned as a ligand np to metal 1s ($Kβ_{2,5}$) transition with Kβ'' contribution stemming from ligand ns to 1s Fe. In order to resolve these very weak fluorescence lines longer counting times are required for a better statistic, as well as a higher resolution as mentioned above. Even with this semi good resolution valence-to-core contributions could be seen during this run. Further improvements were not possible in the short of time. Overall, we could demonstrate the feasibility of high resolution hard X-ray emission spectroscopy at beamline BL9 which can be a powerful tool for a quantitative probe of iron metal spin state, oxidation state and ligand identity.

Reference:

[1] Rueff, J-P., et al. "Pressure-induced high-spin to low-spin transition in FeS evidenced by X-ray emission spectroscopy." *Physical Review Letters* 82.16 (1999): 3284, DOI: 10.1103/PhysRevLett.82.3284.

[2] Weis, Christopher, et al. "Combining X-ray $Kβ_{1,3}$, valence-to-core, and X-ray Raman spectroscopy for studying Earth materials at high pressure and temperature." *Journal of Analytical Atomic Spectrometry* (2018), DOI: 10.1039/C8JA00247A.

[3] Glatzel, Pieter, and Uwe Bergmann. "High resolution 1s core hole X-ray spectroscopy in 3d transition metal complexes—electronic and structural information." *Coordination chemistry reviews* 249.1-2 (2005): 65-95, DOI: 10.1016/j.ccr.2004.04.011.

Acknowledgment

We would like to thank the DELTA machine group for providing synchrotron radiation and technical support.

Development of a Scanning Reflection X-ray Microscope (SRXM)

A. Schümmer[1], M. Gilbert[1], H.-Ch. Mertins[1],
R. Adam[2], C. M. Schneider[2], L. Juschkin[3], U. Berges[4]

[1] University of Applied Sciences, Münster Stegerwaldstraße 39, 48565 Steinfurt, Germany
[2] Forschungszentrum Jülich, Wilhelm-Johnen-Straße, 52428 Jülich, Germany
[3] Rhein Westfälische Technische Hochschule Aachen, Templergraben 55, 52062 Aachen, Germany
[4] DELTA / TU Dortmund Maria-Goeppert-Mayer-Straße 2, 44227 Dortmund

The advancing miniaturization in magnetic data storage and spintronics requires imaging characterization methods that can also investigate buried layers with element-selectivity and high sensitivity. Free standing zone plates and a scanning device were developed for the extreme ultra violet (EUV) range available at the beamline 12 at the DELTA synchrotron facility. One of the most interesting applications for the SRXM is the chemical / element selective imaging which has been realized in 2018, with a sample of Ti and Si_3N_4 arranged as chess pattern.

Setup

The setup of our SRXM is shown in Fig 1., consisting of a high-resolution zone plate that focuses the beam on a small spot of 6-12 µm diameter on the surface of the sample, more details about the mechanical properties see Tab.1. A central beam stop (CBS) is implemented in the zone plate to block zero order radiation. In contrast to STXM the sample is illuminated in grazing incidence (Tab. 1). This angle allows future magneto-optical reflection spectroscopy as T-MOKE, L-MOKE or XMLD [1]. The magnetic contrast will depend on the orientation between the light's linear polarization vector and the magnetization direction which enables the detection of magnetic domains of ferro- or anti-ferromagnetic materials.

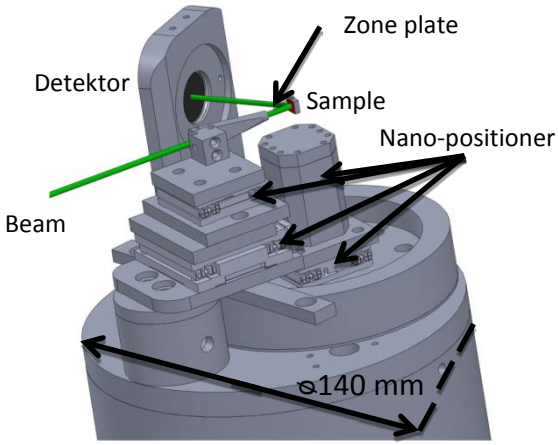

Fig. 1 Setup of the SRXM

Tab 1 – Features of the SRXM

	Horizontal scan	Vertical Scan	Focus range	Incidence angle
Value	-/+10 mm in 50nm steps	+12 mm In 100 nm steps	0-20mm in 50 nm steps	90°-45° to surface (1°accurancy)

As a high resolution EUV optical element the zone plate, created at the FZ Juelich, with a designed spatial resolution of 1250 nm will be used. The zone plate structure has been optimized for the energy range (50-70 eV) and energy resolution ($E/\Delta E$: 50-100) of BL12, resulting in a zone plate of 0.32 mm diameter with a focal length of 15 mm at 60eV and an outermost zone width of 1250 nm.

Imaging chemical contrast

The chemical contrast measurement demonstrates the use of the SRXM at different wavelength. In the photon energy range from 30-70 eV, the reflectivity of the elements Ti and Si_3N_4 changes from identical values at 48eV to strong contrast at 60eV and inverted contrast sign around 30 eV (Fig. 2). This effect is shown with images of a Ti and Si_3N_4 chess pattern. The images are displayed in Fig. 2, right showing the reflection from low reflectance (white) to strong reflectance (black). Strongest contrast is obtained at 65eV (Fig. 3). At 30 eV the images show weaker contrast in Ti and Si_3N_4 but as expected of opposite sign. With tuning the photon energy towards 48 eV the contrast decreases.

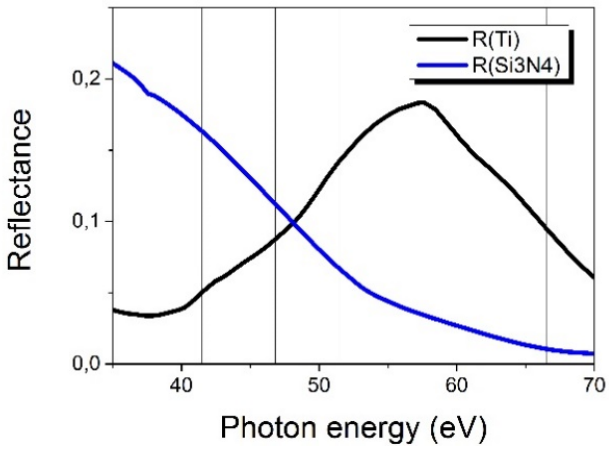

Fig. 2: Reflectance of Si_3N_4 and Ti, calculated with data from the Henke table [2].

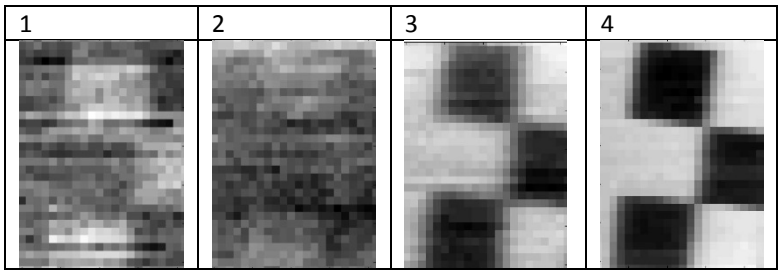

Fig. 3: Image taken with SRXM of a chess pattern consisting of Si_3N_4 and Ti at different wavelength (from left to right: 42eV, 48eV, 52eV, 67eV)

Conclusion and Future developments

We have shown the capability of analyzing the chemical composition of the surface. In a next step we will image explicitely magnetic domain structures and show the capability of investigating buried layer systems.

[1] M. F. Tesch, M. C. Gilbert, H.-Ch. Mertins, D. E. Bürgler, U. Berges, and C. M. Schneider., Appl. Opt. 52, 4294-4310 doi: 10.1364/AO.52.004294 (2013)

[2] L. Henke, E.M. Gullikson, and J.C. Davis. *X-ray interactions: photoabsorption, scattering, transmission, and reflection at E=50-30000 eV, Z=1-92*, Atomic Data and Nuclear Data Tables Vol. 54 (no.2), 181-342 (July 1993)

Soft X-ray Spectroscopy

XPS measurements of CrAlCN DC/HiPIMS PVD coatings

Wolfgang Tillmann[1,a], Dominic Stangier[1,b],
Peter Roese[2,c], Karim Shamout[2,d], Ulf Berges[2,e], Carsten Westphal[2,f]

[1]Institute of Materials Engineering, TU Dortmund University, Germany
44227 Dortmund, Leonhard-Euler-Straße 2

[2]Fakultät Physik / DELTA, TU Dortmund University, Germany
44227 Dortmund, Maria-Goeppert-Mayer-Straße 2

[a]wolfgang.tillmann@uni-dortmund.de, [b]dominic.stangier@uni-dortmund.de,
[c]peter.roese@uni-dortmund.de, [d]karim.shamout@uni-dortmund.de, [e]ulf.berges@uni-dortmund.de, [f]westphal@physik.uni-dortmund.de

Nanocomposite PVD coatings consisting of a crystalline hard phase, which is embedded in an amorphous matrix are of great importance for applications in wear protection and manufacturing processes [1,2]. These coatings offer unique tribo-mechanical properties, which are dominated by the ratio of crystalline to amorphous components and are influenced by the chemical composition as well. In this context, especially nanocomposite coatings composed of a-Si_3N_4 matrix and a hard ternary crystalline Cr or Ti-based nitride phase have been in the focus of recent investigations to improve the high-temperature oxidation resistance and to adjust the tribological properties [3,4]. In addition to silicon containing amorphous matrix materials, the phase separation can also be induced by carbon [5]. However, investigations on these systems, substituting the a-Si_3N_4 by a-C, are of great interest due to the low friction properties and the excellent wear resistance of the carbon [6,7]. Regardless of this fact, only a few studies have so far focused on the synthesis of these systems. Therefore, there is still a lack of knowledge concerning the structural evolution and the correlation to the tribo-mechanical properties of these systems. Within this context, reactively sputtered CrAlCN coatings, processed by a hybrid DC/HiPIMS technology with different carbon contents, were deposited onto heat-treated tool steel substrates. The structural properties were analyzed by high

resolution XPS to understand the evolution of the phase composition in dependency of the carbon content.

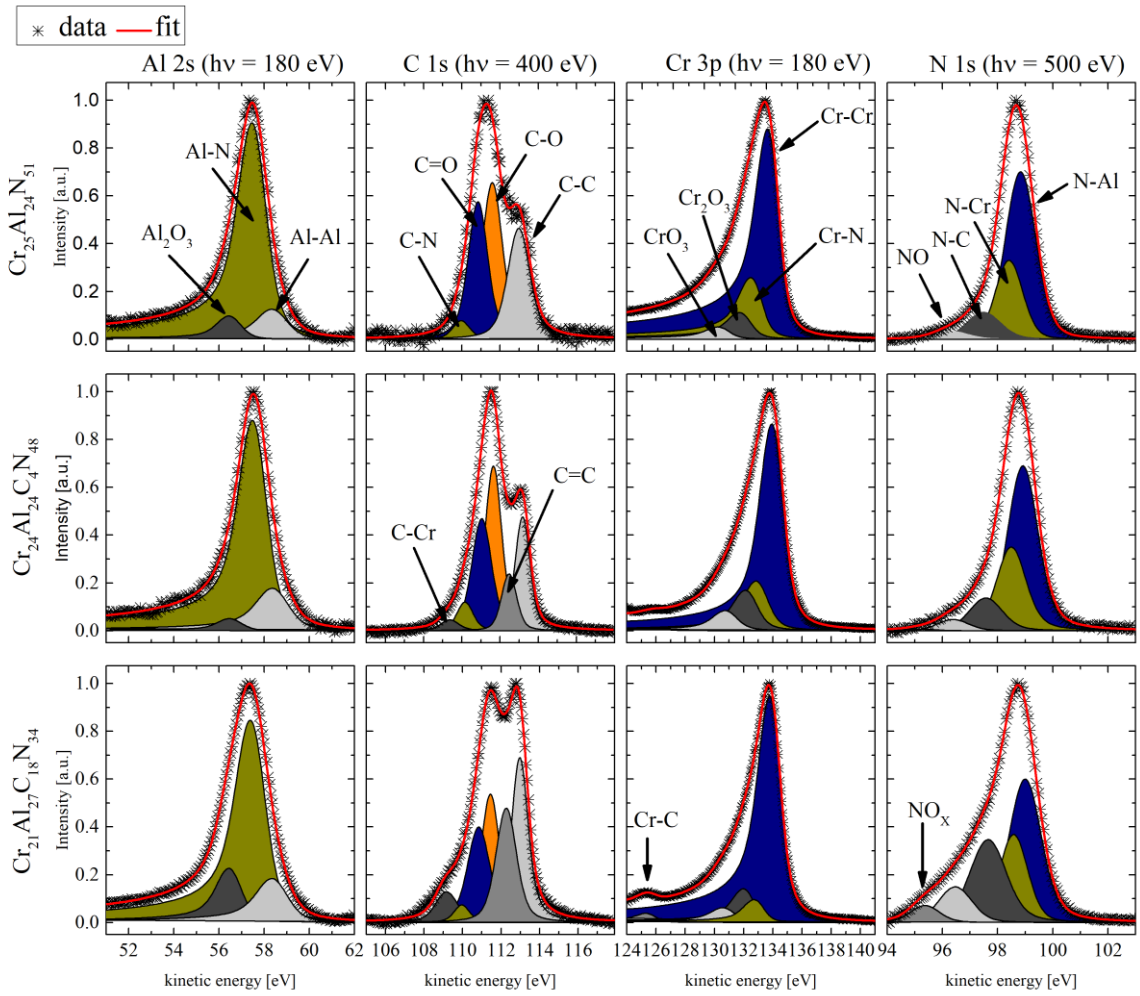

Figure 1: High-resolution XPS spectra of the Al 2s, C 1s, Cr 3p, and N 1s orbitals

The results obtained for the XPS measurements are summarized in Figure 1. It is clearly visible that the variation of the carbon content leads to structural changes in the PVD coatings. With an increasing carbon content, the formation of amorphous C-C, C=C, and C-N structures was observed. Additionally, for the $Cr_{21}Al_{27}C_{18}N_{34}$ coating an increased amount of Cr-C bondings was also detected, leading to a shift of the Al/ Cr ratio in the crystalline fcc CrAlN phase and therefore favor the formation of hexagonal AlN. However, the investigations also prove that the bondings of the Al are not affected by the carbon incorporation in the coating system. All coatings show the highest intensity for the Al-N bonding and small amounts of Al-Al as well as Al_2O_3. The same tendency was observed for the Cr 3p orbital. These results are directly

linked to the core level spectra of the N 1s signal and are in excellent agreement with the observations for Cr 3p and Al 2s.

Based on these results, the formation of carbon containing amorphous phases could be proven and the correlations to the macroscopic properties such as the hardness, Young's modulus, and adhesion of the CrAlCN coatings needs to be part of future work. Especially the effect of the carbon content on the tribological properties needs to be investigated in detail.

References

[1] D.J. Lockwood (Ed.), Nanostructured Coatings, Springer, 2006.

[2] S. Reich, M. Schadewald, M. Bornemann, Materialwissenschaft und Werkstofftechnik 38 (2007) 108–111.

[3] S. Veprek, Surface and Coatings Technology 133-134 (2000) 152–159.

[4] S. Veprek, Advanced Materials Science 5 (2003) 6–16.

[5] U. Jansson, E. Lewin, Thin Solid Films 536 (2013) 1–24.

[6] S.K. Ahn, S.H. Kwon, Journal of Korean Physical Society (2009) 1212–1216.

[7] S.-K. Ahn, S.-H. Kwon, K.-H. KIM, Transactions of Nonferrous Metals Society of China 21 (2011) 78–82.

Beamline BL 5: Forschungszentrum Jülich and Technische Universität Dortmund

Stefano Ponzoni, Mahdi Hajlaoui and Mirko Cinchetti

Experimentelle Physik 6, Fakultaet Physik, TU Dortmund
D-44221 Dortmund
Germany

BL 5 is a VUV beamline located at the U250 planar electromagnetic undulator of Delta. With a photon energy seamlessly tunable between 9 eV and 400 eV BL5 is designed for high resolution photoemission spectroscopy. The experimental station is equipped with a Scienta SES 2002 hemispherical analyzer coupled to a Focus SPLEED detector allowing for both high resolution angle resolved photoemission spectroscopy and spin-resolved photoemission spectroscopy. This configuration makes BL5 ideal for the investigation of the electronic structure of magnetic materials, surfaces, and low dimensional systems.

BL5 is currently operated by Prof. Mirko Cinchetti's Experimentelle Physik 6 (E6) group, from the Technische Universität Dortmund, as part of a collaboration between the E6 group and Prof. Schneider from the Forschungszentrum Jülich.

Most of the available machine time was employed in the investigation of the electronic structure and of the spin properties of hybrid interfaces and low dimensional systems. Two new collaborations, with Dr. A. Brambilla from the Politecnico di Milano and with Dr. R. Di Pietro from the Hitachi Cambridge Laboratory, were initiated. The electronic structure of GaAs/AlGaAs quantum wells was also investigated in the framework of project A08 of the SFB TRR 142 (TU Dortmund and Paderborn University).

The collaboration with Dr. Brambilla aims to the investigation and to the comprehension of the rich and still largely unexplored spin physics in novel hybrid interfaces based on the insertion of a ultra-thin metallic oxide layer between a ferromagnetic substrate and an organic layer.

Since the formation of spin polarized hybrid interface states in a spinterface has been proven to directly influence the spin transport properties of the heterostructure, controlling the surface reactivity is of primary importance for the tailoring of its performance as a building block for organic spintronic devices. In this framework the insertion of a thin oxide layer provides a way to both control the surface reactivity, increasing its reliability and reproducibility due to its chemical stability, and the magnetic interaction between the ferromagnet and the organic layer.

In a recent work [1] the growth of a nearly two-dimensional Cr_4O_5 layer between a Fe(001) substrate has proven to enhance the magnetic hybridization of the spinterface formed with a C60 overlayer with respect to both the bare C60/Fe(001) and the C60/Fe(001)-p(1x1)O heterojunctions. XMCD measurements on the C k1-edge highlight an induced spin polarization in the π^* states of the fullerene. First-principle theoretical calculations suggest that the effect is due to the hybridization of the unoccupied molecular orbitals with the highly spin-polarized Cr d-states in the conduction band of the oxide layer. In this framework we performed bot high resolution ARPES and spin-ARPES measurements on both C60/Fe(001)-p(1x1)O and the $C60/Cr_4O_5/Fe(001)$ heterojunctions in order to investigate the spin-dependent electronic structure of the spinterfaces valence band, with particular emphasis on the C60 HOMO states. This work was also the subject of L. Kugler's thesis, a master student at E6 in 2017/2018.

Despite preliminary results show no significative spin polarization of the C60 occupied molecular orbitals in the C60/Cr_4O_5/Fe(001) hybrid interface, spin-resolved photoemission measurements on C60/Fe(001)-p(1x1)O reveal a spin dependent spectral weight for the fullerene HOMO levels (Fig.1), together with a spin-dependent attenuation of the Fe(001)-p(1x1)O background.

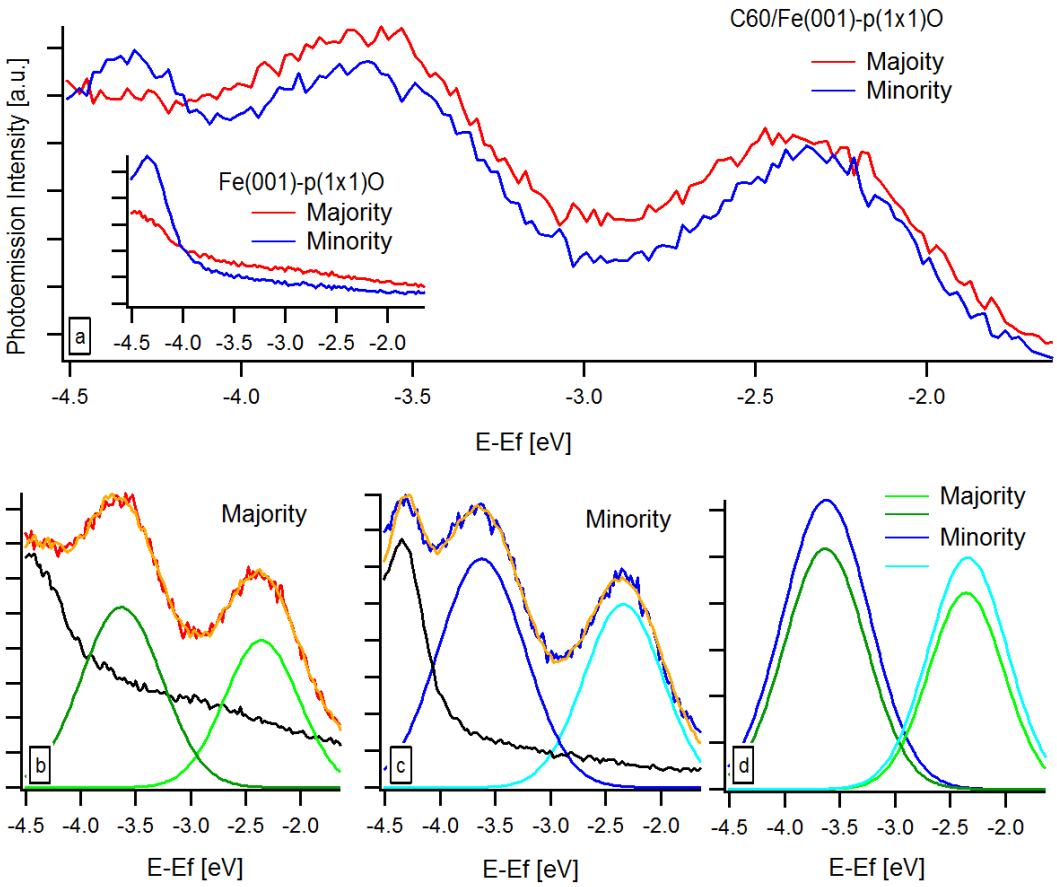

Figure 1: (a) Spin resolved UPS signal from C60/Fe(001)-p(1x1)O heterostructure. The inset is the spin resolved UPS signal from the bare Fe(001)-p(1x1)O substrate. (b,c) Interpolation of the majority and minority UPS signal (yellow line) with a combination of the spin-dependent photoelectron background from the substrate (black line) and two gaussian functions, representing the HOMO and the HOMO-1 states of C60. (d) Comparison of the molecular states features for the two spin channels as obtained from the interpolation procedure. The difference in the amplitude is evident. All measurement were performed at normal emission and with 21.2 eV photons.

The reduced spectral weight of the majority sates can be rationalized in terms of a shorter hole lifetime due to the coupling with the highly (majority) spin polarized Fe d-bands, and is consistent with a spin-dependent generalization of the Newns-Anderson model [2] for week chemisorption in metal/molecule interfaces. On the other hand, the spin dependent attenuation of the photoelectron background from the iron states might indicate that a net magnetic moment is also induced on the Fullerene molecules despite the oxygen decupling layer. In future the spin dependent electronic structure of Fe(001)-p(1x1)O interfaces with planar organic molecules, such as porphyrins, will be investigated.

The collaboration with the group of Dr. Orgiu, from INRS-EMT (Quebec), was continued. Relative work function measurements, with respect to the bare substrate, were performed together with a characterization of the valence band states, by means of UPS, on self-assembled NDI-C_{22}/HOPG interfaces, where the modulation of the surface electrostatic potential, on a nanoscopic scale, leads to intriguing electronic transport properties [3].

A preliminary valence band UPS characterization was also carried out on N2200/GaAs hybrid systems, as a part of a collaboration with Dr. Riccardo Di Pietro, from the Hitachi Cambridge Laboratory (UK). N2200 is an electron acceptor polymer currently investigated as a candidate for the realization of polymeric solar cells and organic electronics devices. The understanding of the polymer electronic structure and the energy level alignment at the heterointerface is a mandatory requirement for the optimization of the device performances.

High resolution ARPES measurements GaAs/AlGaAs quantum well structures (QW) were performed as a part of the SFB TRR 142 A08 project, in collaboration with Prof. T. Zentgraff, from Paderborn university. These experiment established a reliable sample preparation protocol for the removal of the As protective capping layer of the QW, which are prepared ex-situ. In future the quantum well states will be directly probed by means of laser-based time-resolved micro-ARPES in the E6 laboratory.

[1] A. Brambilla et al, Nano Lett. 17, 7440, (2017).

[2] D. M. Newns et al, Phys. Rev. 178, 1530, (1969).

[3] M. Gobbi et al. Nature Comm., 8, 14767, (2017).

FeS_2 (001) sample characterization by means of XPS and XPD

C. Kohlmann[1,2,*], K. Shamout[1,2], P. Roese[1,2], L. Kesper[1,2], U. Berges[1,2], C. Westphal[1,2]

[1] Experimentelle Physik I - Technische Universität Dortmund, Otto-Hahn-Str. 4a, D-44221 Dortmund
[2] DELTA - Technische Universität Dortmund, Maria-Goeppert-Mayer-Str. 2, D-44221 Dortmund
[*] corresponding author: christopher.kohlmann@tu-dortmund.de

The determination of atom locations in crystalline structures is of great importance for numerous systems and applications. Without a detailed knowledge about the atomic structure, the calculation of electronic properties or the creation of synthetic systems with pre-determined properties would not be possible. For structures directly at the surface, scanning-probe microscopy yields an applicable method to gain direct information about a crystals atomic structure. However, in the subsurface region and at buried internal interfaces, no direct three dimensional structure examination techniques are available up until recently. One way to image the three-dimensional atomic structures in subsurface regions is the holographic approach discovered by D. Gabor in 1948 [1]. In order to obtain a hologram, an object has to be irradiated with coherent radiation and the interference pattern of the emitted object-waves and the reference-wave has to be recorded. The hologram itself is the recorded interference pattern of this process. The object-wave can be reconstructed by irradiating the hologram with the reference-wave. A part of the emitted waves from this process imitates the original object-waves in phase and amplitudes. Originally, this technique has been discovered for visible light. Nowadays, this technique is also applicable for electron-waves. Szöke proposed to use photoelectron-waves for the holographic process to directly image atoms locations, as they have small wavelengths suitable for atom imaging [2]. Despite various attempts and great effort, the photoelectron holography was not as succesfull as imagined. Images reconstructed from the holograms were plagued by severe artifacts and only in a few special cases reconstructions of up to 10 atoms could be achieved [3-7]. In 2010, Matsushita et al. published an algorithm "Scattering Pattern Extraction Algorithm with Maximum Entropy Method", which was capable of improved image reconstruction for photoelectron holography in the soft x-ray regime to observe buried structures near the surface region [8]. This method applies regression techniques for reconstructing the crystal structure from experimental data. In 2016, we proposed a photoelectron holography technique for the hard x-ray regime, which is capable of reconstructed images displaying up to 1000 atoms at true atom locations within a range of 16 Å around an emitter source [9]. To confirm the applicability of this holography technique a proof of principle experiment will be carried out in Feb. 2019 at SPring-8, Japan. For this, a pyrite (FeS_2) sample has to be characterized.

In the first step, two kind of FeS_2(001) samples were prepared from an isomorphic pyrite crystal from La Rioja, Spain. The first sample type has been polished and preparated by the procedure proposed by S. Charturvedi et al. [10]. For the preparation process the sample has been annealed at a temperature of $T = 300°$ C for 5 minutes and afterwards sputtered for 10 minutes with Ne^+-ions, which had a kinetic energy of $E_{kin} = 200$ eV. This process has been repeated ten times. For the other sample we used a naturally as grown crystal surface. Therefore no preparation or polishing processes have been applied to this sample type.

Those two sample types have been analyzed by means of photoelectron spectroscopy (XPS) and -diffraction (XPD). For our XPS study the samples were irradiated by x-rays with a photonenergy of $h\nu = 800$ eV in an ultra high vaccum chamber (UHV chamber). Due to the photoelectric effect, electrons are emitted from their binding-orbitals and can be detected by means of their kinetic energies. The result is a spectrum, which shows the intensity of the detected electrons as function of their kinetic energy. The peakpositions are correlated to the emitted photoelectrons binding orbital, which enables a chemical sensitive analysis of the observed sample system. The XPD procedure is based on XPS. For each polar- and azimuth-angle pair the intensity modulation of one XPS-signal is observed. Due to electron diffraction in the crystal lattice the electron waves interfere with eachother. The recorded interference pattern resembles the symmetry of the crystals atom lattice and contains information about the atomic structure.

The results can be seen in figure 1. The survey spectrum in figure 1(a) shows that the polished sample has less contamination on its direct surface. Compared to the survey spectrum of the as grown sample in figure 1(c) the survey shows less peaks of contamination material. Nonetheless, the survey spectrum of the polished surface shows an unexpected ratio of the S 2p and the Fe 3p signals. The ratio should be 2:1 but is about 10:1 . This indicates a S_2-terminated surface, which implies the destruction of the monocrystaline FeS_2 structure near the direct surface. Even though the sample with an as grown surface is contaminated with adsorbats, the ratio of the S 2p and the Fe 3p signal is about 2:1 , which indicates that the monocrystaline structure is preserved.

To test if a diffraction patern could be obtained, the intensity modulation of the Fe 3p signal for one polar angle at $\Theta = 30°$ has been analyzed. The results are shown in figure 1(b) and 1(d). Just the as grown surface shows a symmetric intensity modulation, which indicates that the superposition of the intensity-modulations of the same

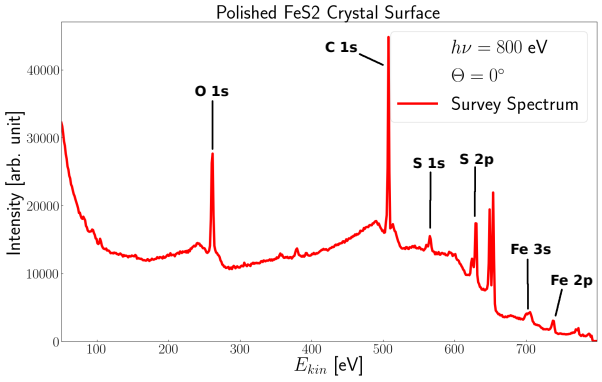

(a) Survey XPS spectrum of the polished FeS_2 sample

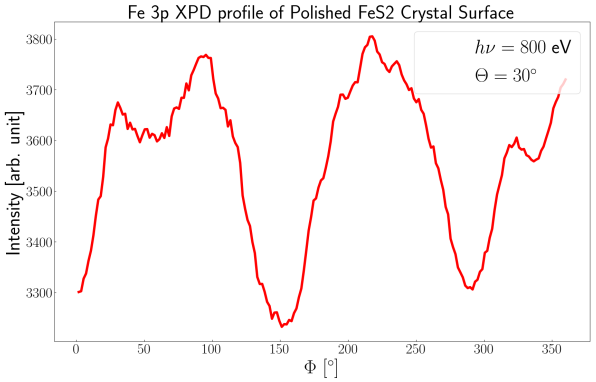

(b) Fe 3p XPD intensity modulation of the polished FeS_2.

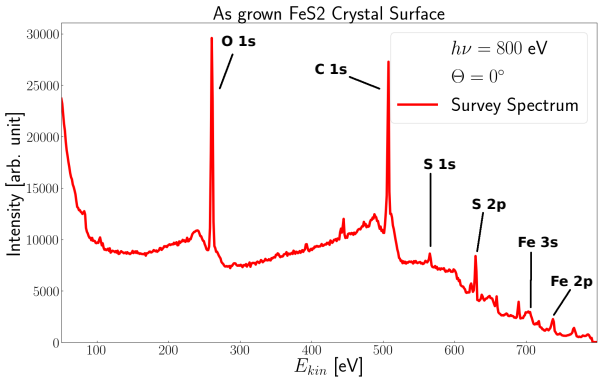

(c) Survey XPS spectrum of the as grown FeS_2 sample.

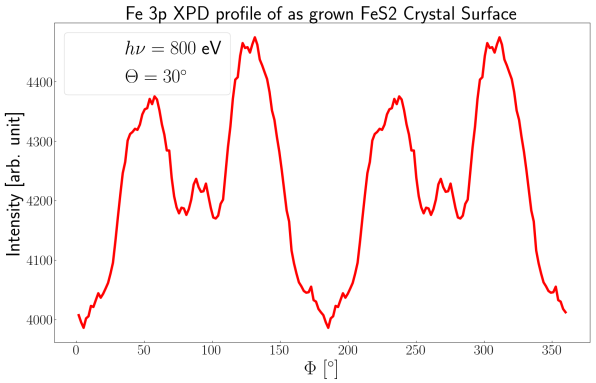

(d) Fe 3p XPD intensity modulation of the as grown FeS_2.

Figure 1: The XPS and XPD data of the two sample types. The XPS spectra were taken for a photon energy $h\nu = 800\,\mathrm{eV}$ and a polar angle $\Theta = 0°$. The XPD modulation was taken for the same energy and under a polar angle $\Theta = 30°$ for the Fe 3p signal. The XPD modulation indicates, that the crystal structure of the polished crystals surface is not monocrystalline.

local structure has been observed. This shows that a monocrystalline structure is preserved at the subsurface. For the polished sample no symmetries could be observed, which shows that the periodic crystal structure must be broken. Therefore no diffraction patterns which suffice for a holographic reconstruction can be gained from this sample type.

It can be concluded, that the sample with an as grown (001)-surface should be used for the high energy photoelectron diffraction (HXPD) study at SPring-8. Even though contaminations at the surface were observed. However the noise from those contaminations will not be a hinderance for a HXPD study. Due to the very large information depth of high energetic photoelectrons, the signal to noise ratio will be sufficent for holographic reconstruction calculations. However a second study, on how to minimize the contamination on an as grown sample surface without destroying the crystal structure, will be carried out before the beamtime at SPring-8 to obtain the best possible outcome.

References

[1] D. Gabor, *Nature* **161**, 777 (1948).
[2] A. Szöke, *AIP Conf. Proceed.* **147**, 361 (1986).
[3] J.J. Barton, *Phys. Rev. Lett.* **61**, 1356 (1988).
[4] G. R. Harp et al., *Phys. Rev. Lett.* **65**, 1012 (1990).
[5] J. Osterwalder et al., *J. Electron Spectrosc. Relat. Phenom.* **68**, 1 (1994).
[6] P. M. Len et al., *Phys. Rev. B* **59**, 5857 (1999).
[7] J. Wider et al., *Phys. Rev. Lett.* **86**, 2337 (2001).
[8] T. Matsushita et al., *J. Electron Spectrosc. Relat. Phenom* **178**, 195 (2010).
[9] T. Lühr et al., *Nano Lett.* **16**, 3195 (2016).
[10] S. Chaturvedi et al., *Americ. Mineralog.* **81**, 261 (1996).

Investigation of two-dimensional germanium on Ag(110) by means of XPS

L. Kesper[1,2,*], P. Roese[1,2], K. Shamout[1,2], U. Berges[1,2], C. Westphal[1,2]

[1] Experimentelle Physik I - Technische Universität Dortmund, Otto-Hahn-Str. 4a, D-44221 Dortmund

[2] DELTA - Technische Universität Dortmund, Maria-Goeppert-Mayer-Str. 2, D-44221 Dortmund

[*] corresponding author: lukas.kesper@tu-dortmund.de

The discovery of graphene by Novoselov and Geim in 2004 opened the new field of monolayer materials (2D) in solid state physics, which are called the Xene-materials. Apart from graphene other Dirac materials, like silicene and germanene, for instance, provide similar properties in a two dimensional structure [1]. Silicene and germanene are predestined because of its strong spin-orbit coupling and tunable band gap for realising topological field effect transistor. The first synthesis of silicene was reported in 2012 and since then it was studied multiple times on several substrates. Even one dimensional nano-ribbons of silicon were be prepared on the here used Ag(110) surface [2] in order to show more attractive electronic properties [1]. The stronger buckling and spin-orbit coupling of germanene may allow to observe the quantum spin Hall effect [3, 4]. In this work germanene is grown epitaxially on a Ag(110) surface and studied using Low Energy Electron Diffraction and X-Ray Photoelectron Spectroscopy.

The first step is to prepare the surface of the silver sample under ultra-high vacuum condition at a base pressure of $p = 2 \times 10^{-10}$ mbar. Several cycles of sputtering and annealing are used for preparation. For sputtering argon ions are accelerated on the sample to remove residuals from the substrate. The subsequently annealing heals remaining defects and effects a reconstruction of the surface. The cleanness and reconstruction of the surface was checked by LEED measurements, shown in figure 1a. The LEED pattern, recorded at a kinetic energy

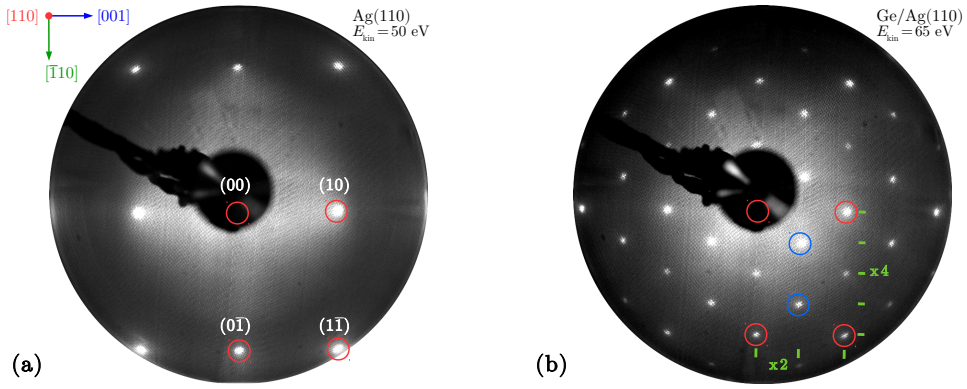

Figure 1: (a) LEED pattern of a clean Ag(110) sample. The red circles indicate the substrate spots of the $p(1\times1)$ reconstruction. (b) LEED pattern of a $c(4\times2)$ superstructure (green/blue) after the growth of less than one monolayer germanium on silver (red).

of $E_{\mathrm{kin}} = 50\,\mathrm{eV}$, shows the unity cell of the $p(1 \times 1)$ reconstruction of the silver, marked by red circles. The germanium is grown epitaxially on the heated Ag(110) sample using electron beam evaporation, resulting in the LEED pattern shown in figure 1b, at $E_{\mathrm{kin}} = 65\,\mathrm{eV}$. Germanium forms a $c(4 \times 2)$ superstructure, marked by green dashes. The centered spots are

circled in blue. A first analysis of the XPS data reveal a thickness of 0.75 ML germanium on the substrate. The results from the LEED and thickness measurements agree with previous STM and LEED studies on this system [5]. XPS can be used to analyse chemical bondings at the interface between the substrate and the adsorbate. Therefore high resolution XPS spectra are recorded and fitted, as shown in figure 2. The polar angle between sample normal and spectrometer is set to $\Theta = 60°$ in order to reach a higher surface sensitivity. The Ag 3d signal shows a splitting of 6 eV due to their spin-orbit coupling. The XPS spectra of the clean silver sample is illustrated in figure 2 on the left. Three plasmon features appear next to the signals of the Ag 3d orbital. Collective oscillations of free electrons at the surface are comprehended as plasmones that can be seen at fixed energies related to the main peaks and signalise clean surfaces [6]. The plasmon peaks vanish after the evaporation of germanium on the substrate. Both spectra of the Ag 3d signal can be fitted by only one Voigt-like component. Even after the growth of germanium on the silver substrate the XPS spectrum, shown in the center of figure 2, does not change due to a possible chemical bonding. The

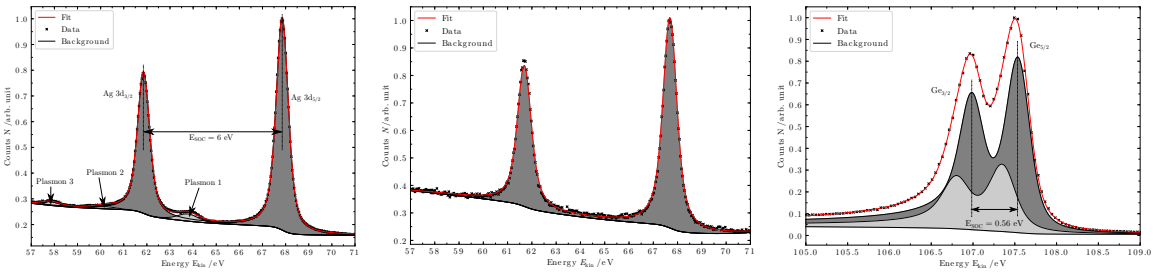

Figure 2: High resolution XPS-measurement, recorded at $\Theta = 60°$. Left: Ag 3d orbital of a clean Ag-sample with an excitation energy of $h\nu = 440$ eV. Center: Ag 3d orbital of the Ge/Ag(110) system with 0.75 ML of germanium. Right: Ge 3d orbital of the same Ge/Ag system with an excitation energy of $h\nu = 140$ eV.

XPS spectrum of the Ge 3d orbital, shown in figure 2 on the right, can be fitted with two chemically shifted components, separated by 0.2 eV. Both chemically shifted components are split by $E_{\mathrm{SOC}} = 0.56$ eV due to the spin-orbit coupling. This gives a clear evidence that the germanium atoms are present in two different chemical environments. Further analysis of this data as well as photoelectron diffraction analysis will be carried out to perform a structural determination of the two-dimensional germanium on the Ag(110).

References

[1] M. Ezawa et al., *Fundamentals and functionalities of silicene, germanene, and stanene*, La Rivista del Nuovo Cimento **41**, 175 (2018).

[2] C. Léandri et al., *Self-aligned silicon quantum wires on Ag (110)*, Surface science **574**, L9 (2005).

[3] A. Molle et al., *Buckled two-dimensional Xene sheets*, Nature materials **16**, 163 (2017).

[4] C.-C. Liu et al., *Quantum spin Hall effect in silicene and two-dimensional germanium*, Physical review letters **107**, 076802 (2011).

[5] C. Léandri et al., *Self-assembled germanium nano-clusters on silver(110)*, Surface science **573**, L369 (2004).

[6] J. Leiro et al., *Study of plasmon structure in XPS spectra of silver and gold*, Journal of Physics F: Metal Physics **13**, 215 (1983).

Structural and chemical analysis of a Pt/Si-alloy on a Si(100) substrate by means of low energy electron diffraction (LEED) and X-ray-photoelectron spectroscopy (XPS)

M. Schmitz[1,2,*], P. Roese[1,2], K. Shamout[1,2], U. Berges[1,2], C. Westphal[1,2]
[1] Experimentelle Physik I - Technische Universität Dortmund, Otto-Hahn-Str. 4a, D-44221 Dortmund
[2] DELTA - Technische Universität Dortmund, Maria-Goeppert-Mayer-Str. 2, D-44221 Dortmund
[*] corresponding author: marie.schmitz@tu-dortmund.de

In recent years Metallic platinum silicide has raised much interest due to possible applications in spintronic devices.
This alloy formation can be used for rectifying junctions on silicon substrates [1] as well as for interconnects in microelectronics [2].

It is known from literature that ultra thin films of platinum form nano wires on the silicon surface [3], whose characteristics in the density of states offer a giant Rashba-type band splitting [4].
The formation process has been studied on substrates in different orientations using STM [5]. They reported a platinum island growth after platinum deposition of 5 ML onto the surface. Those islands remain stable for temperatures up to T = 550°C. For higher temperatures alloy formation takes place.
In this work, a Platinum silicon alloying on a Si(100) surface for thin platinum films was studied using low energy electron diffraction (LEED) X-ray photoelectron spectroscopy (XPS).
The experiments were performed at the U55 beamline 11 at DELTA.
Figure 1 shows the LEED pattern at two different kinetic energies for different temperature stages of Pt/Si on Si(100).

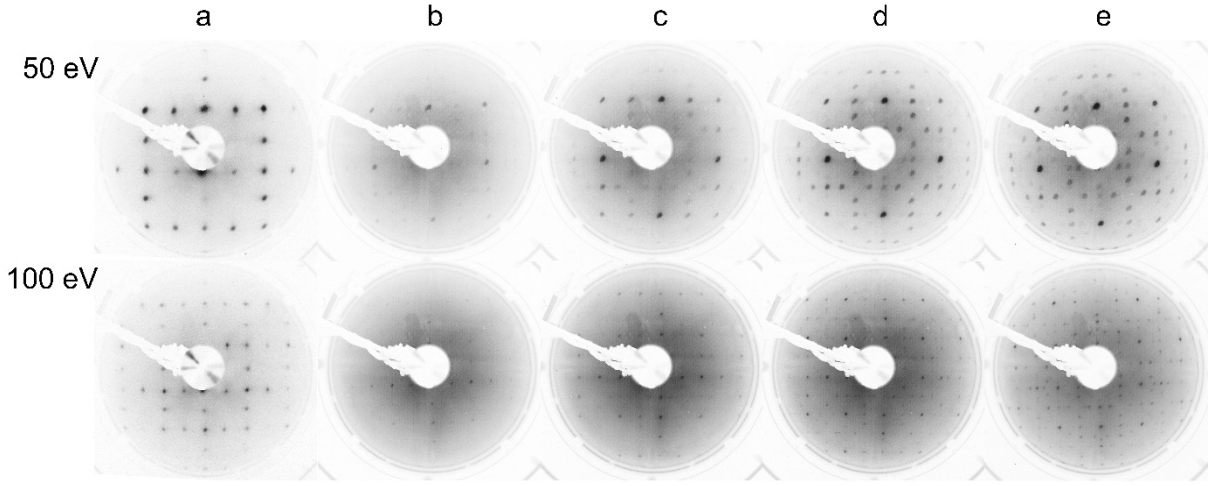

Figure 1: LEED pattern of different temperature stages of the Pt/Si alloy on a Si(100) surface at kinetic energies of 50 and 100 eV, respectively.
a) prepared clean Si(100)-(2×2) surface. The surface shows a (2x2) reconstruction with two domains, rotated by 90°.
b) after deposition of a thin platinum film onto the Si(100) surface the LEED-pattern gets more diffuse due to island formation.

c) while heating the probe up to T = 600°C the Pt-Si alloy formation starts indicated by a clearing of the LEED pattern.
d) at a temperature of T = 750°C the alloy shows new spots due to a surface reconstruction, surrounding the Si-spots.
e) LEED pattern of the final Pt/Si alloy.
For further analysis the chemical bondings of the Si atoms are analysed using XPS measurements at a photon energy of hv = 250 eV.
The results of the annealed Pt surface are shown in Figure 2.

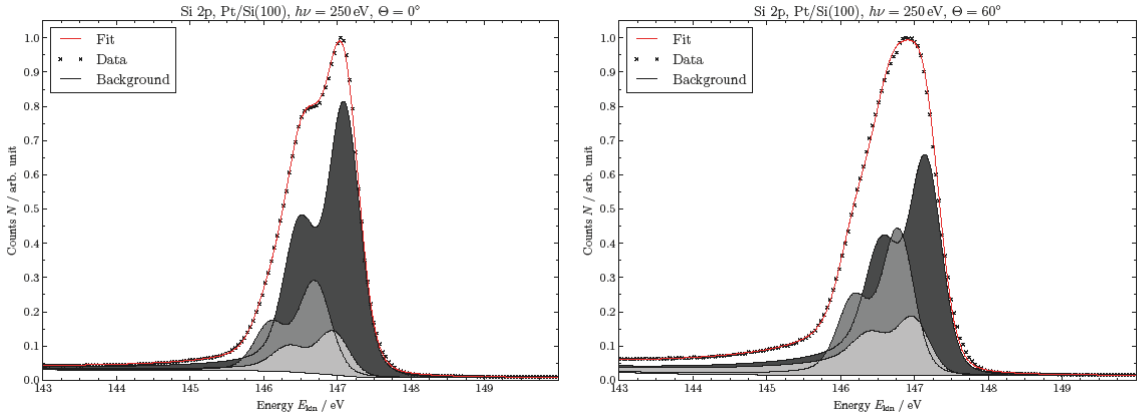

Figure 2: Highresolution Si 2p XPS-spectra of annealed Pt/Si(100) recorded at a photon energy of hv = 250 eV and polar angles of Θ = 0° (left) and Θ = 60° (right).

The spectra can be fitted with thre voigt-like components at kinetic energies of C1: 147,10 eV, C2: 146,96 eV, C3: 146,70 eV. Each component is split by 0,6 eV due to the spin-orbit coupling. The C1 doublet can be identified as Si bulk component. Due to their higher intensity at the surface sensitive measurement, the C2 and C3 components refer to bonding states at the surface.

As a result it can be concluded that the Pt/Si alloy is temperature dependent and the chemical bondings of the silicon atoms can be divided into the bulk and two components at the surface indicating two different chemical environments in the topmost layers.
We're looking forward to perform photoelectron diffraction measurements of the Pt-Si alloy for an exact structure determination.

References

[1] O. Beckstein, et al., Phys. Rev. B 63, 134112 (2001)
[2] R.T. Fryer, et al., J. Alloy. Compd. 682, 216e224 (2016)
[3] Do Kyung Lim, et al., Nano. 18, 095706 (2007)
[4] J. Park, et al., Physical Review Letters 110, 036801 (2013)
[5] A. Wawro, et al., Phys. Rev. B. 72, 205302 (2005)

Structure determination of substrate influenced silicon nano-ribbon growth

P. Roese[1,2,*], P. Espeter[1,2], K. Shamout[1,2], R. Hönig[1,2], U. Berges[1,2], C. Westphal[1,2]

[1] Experimentelle Physik I - Technische Universität Dortmund, Otto-Hahn-Str. 4a, D-44221 Dortmund

[2] DELTA - Technische Universität Dortmund, Maria-Goeppert-Mayer-Str. 2, D-44221 Dortmund

[*] corresponding author: peter.roese@tu-dortmund.de

In the past decade, two-dimensional materials raised scientific interest due to their unique structural and electronic properties. Starting with the discovery of graphene in 2004 [1], the field of two-dimensional materials is strongly growing every year and plenty of new 2D materials are found and characterized. Especially, the two-dimensional silicon nano-ribbons came into scientific focus for possible applications like spintronic devices, which led to a rising interest in the growth and structural analysis of these silicon nano-ribbons. Concerning the growth of silicon nano-ribbons on Ag(110), several publications reported about the formation of the rare, pentagonal silicon structure and a very weak interaction between the silicon nano-ribbons and the Ag(110) substrate [2-5]. Based on this, the question arises whether silicon nano-ribbons form a pentagonal structure on a Au(110) substrate as well. In literature, there is only one report on the growth of silicon nano-ribbons on Au(110), where silicon seemed to grow in a very similar way compared to the growth on a Ag(110) substrate [6]. Since this STM study only probes the topmost layer of the sample surface, the interface structure as well as individual differences in the bonding states of each atom due to the missing chemical resultution of STM could not be determined. To address the arising questions of the internal structure and a possible AuSi alloy formation beneath the silicon nano-ribbons, we performed low energy electron diffraction (LEED), photoelectron spectroscopy (XPS) and angle-resolved photoelectron diffraction (XPD) experiments on silicon nano-ribbons on Au(110).

Therefore, a silicon amount of ≈ 0.4 ML was evaporated onto a clean, (2x1)-reconstructed Au(110) surface. In figure 1 a) and b) the LEED images of the Au(110) surface before and after the silicon evaporation are shown. It's clearly visible, that the surface reconstruction vanishes upon silicon adsorption and only the (1x1)-spots of the bulk remain visible, marked with red circles in figure 1 b). Additionally, silicon forms a (nx6)-periodicity with respect to the underlying substrate, which indicates the successfull preparation of silicon nano-ribbons on Au(110) [6]. The strong interaction between the silicon and gold substrate atoms is also indicated by high resolution XPS spectra of the Au 4f signal (not shown here), forming a new chemically shifted component due to a gold-silicide bonding, whereas the surface component vanishes upon silicon evaporation. The recorded Si 2p XPD pattern recorded at an incoming photon energy of 140 eV is shown in figure 1 c).

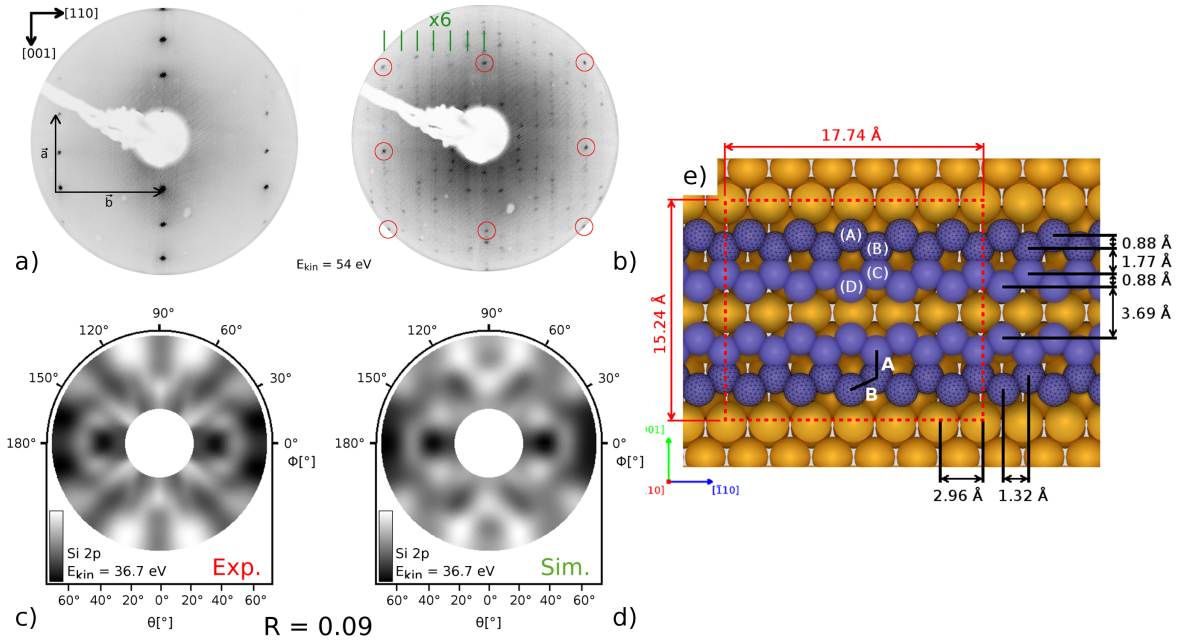

Figure 1: Inverted LEED pattern of the clean (2x1)-reconstructed Au(110) surface a). The vectors $\vec{a}$ and $\vec{b}$ mark the (1x1) bulk unit cell of Au(110). Inverted LEED pattern of 0.4 ML silicon deposited on Au(110) b). The red circles indicate the (1x1) bulk unit cell substrate spots of Au(110) and a (x6)-reconstruction of silicon along the $[\bar{1}10]$-direction is visible. Both pattern are recorded at an electron energy of $E_{\mathrm{kin}} = 54\,\mathrm{eV}$. Experimental Si 2p XPD pattern recorded at a kinetic energy of $E_{\mathrm{kin}} = 36.7\,\mathrm{eV}$ c) and simulated XPD pattern with a R-factor of R = 0.09 d). Structure model for the silicon nano-ribbons on Au(110) resulting from the simulation of the diffraction patterns after applying the genetic algorithm in top-view e). Taken from [7].

After the analysis procedure only one strucuture model for the silicon nano-ribbons on Au(110) showed best agreement between the experimental and simulated pattern as indicated by an R-factor of R = 0.09. The resulting simulated XPD pattern is shown in figure 1 d) and a schematic drawing of the corresponding structure model is shown in figure 1 e). This structure is characterized by two hexagonal zigzag-terminated silicon chains on top of two missing-rows of the substrate, indicating a complete different strucutre compared to the formation of silicon nano-ribbons on Ag(110) as described before. This interesting finding shows that the substrate influences the internal strucutre of the silicon nano-ribbons and can therefore also change the electronic properties of two-dimensional structures. A detailed analysis and characterization of the resulting structure is given in literature [7].

References

[1] K. S. Novoselov et al., *Science* **306**, 666 (2004).
[2] J. I. Cerdá et al., *Nat. Commun.* **7**, 13076 (2016).
[3] P. Espeter et al., *Nanotechnology* **28**, 455701 (2017).
[4] G. Prévot et al., *Phys. Rev. Lett.* **117**, 276102 (2016).
[5] S. Sheng et al., *Nano Lett.* **18**, 2937 (2018).
[6] M. R. Tchalala et al., *Appl. Phys. Lett.* **102**, 083107 (2013).
[7] P. Roese et al., *Appl. Surf. Sci.* **467-468**, 580 (2019).

Intercalation of silver and gold between graphene and silicon carbide

P. Weinert[1,2,*], R. Hönig[1,2], P. Roese[1,2], K. Shamout[1,2], M. Schulte[1,2], U. Berges[1,2], C. Westphal[1,2]

[1] Experimentelle Physik I - Technische Universität Dortmund, Otto-Hahn-Str. 4a, D-44221 Dortmund

[2] DELTA - Technische Universität Dortmund, Maria-Goeppert-Mayer-Str. 2, D-44221 Dortmund

[*] corresponding author: philipp.weinert@tu-dortmund.de

Graphene consists of one single layer of hexagonal arranged carbon atoms. It is characterized by its outstanding mechanical and electronic properties. For example it is the strongest known material, with an ultimate tensile strength of 130 GPa [1] and its charge carrier mobility of $2 \cdot 10^5\,\mathrm{cm}^2/\mathrm{Vs}$ is the highest one known [2]. These properties make graphene highly interesting for many applications.

One method to prepare graphene is to anneal silicon carbide at about 1200 °C in an argon atmosphere. This leads to the sublimation of silicon and the growth of graphene. Unfortunately, the properties of the first layer of graphene are impaired by covalent bonds to the silicon carbide. This first layer is called buffer layer [3, 4, 5]. These bonds can be broken by the intercalation of an element between the silicon carbide and the graphene. This way the buffer layer becomes quasi free standing graphene [6]. For this purpose, silver and gold are used in this work. The materials were deposited onto graphene samples via physical vapour deposition. In figure 1 one image of a sample before (left) and one after (right) the deposition of silver obtained by photoemission electron microscopy (PEEM) is shown. Without the silver, stripes of graphene along the step edges can be seen [7]. After the deposition, this structure is totally covered. In the case of gold, the covered sample leads to a total black picture because of the high work function of gold [8].

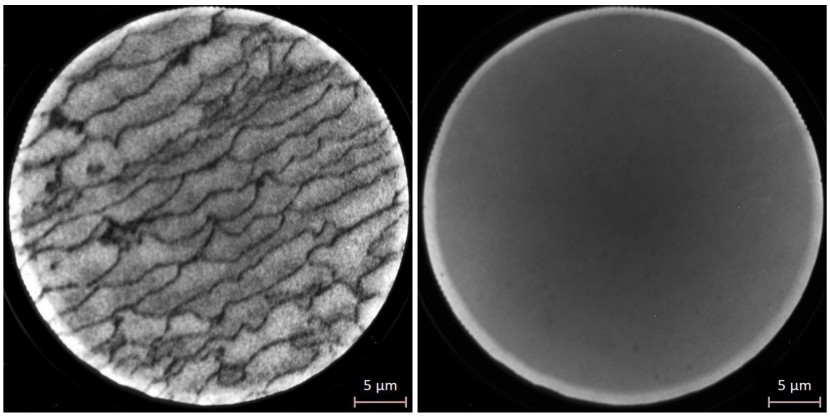

Figure 1: PEEM images of a graphene sample recorded before (left) and after the deposition of silver (right).

After the material has been deposited, the samples were annealed stepwise until the structure of the graphene turned back. This heating process should cause the intercalation of the silver or gold under the graphene. To proof this and refute other explanations, for example the evaporation of the materials, X-ray photoelectron spectroscopy (XPS) was used. In figure 2 and 3 gold and carbon core level spectra of a sample after the intercalation of gold are

shown. The spectrum of the gold 4f signal shown in figure 2 proves the presence of gold on the sample. In addition to this the spectrum of the carbon 1s signal shown in figure 3 can be fitted by two components. One of them is asymmetrical. Therefore this one can be assigned to the graphene. The other one is located at a higher kinetic energy. Therefore this one can be assigned to the silicon carbide [9]. If there would be a buffer layer, it would cause two more components to appear to the left of the signal of the graphene. So it is proven that at least a part of the gold intercalated under the graphene and broken the covalent bounds.

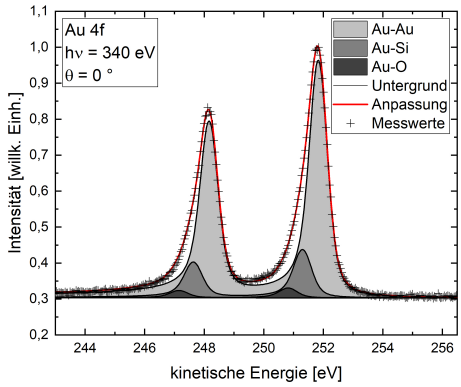

Figure 2: XPS spectrum of the gold 4f signal of a graphene sample grown on silicon carbide after the deposition and intercalation of gold.

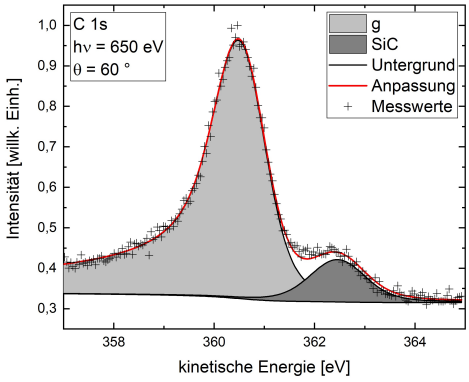

Figure 3: XPS spectrum of the carbon 1s signal of a graphene sample grown on silicon carbide after the deposition and intercalation of gold.

Acknowledgement

We would like to thank the DELTA-staff for their support.

References

[1] C. Lee et al., *Sci.* **321**, 5887 (2008).
[2] H. Kim et al., *Sci. Rep.* **4**, 5278 (2014).
[3] W. A. de Heer et al., *Proc. Natl. Acad. Sci. USA* **108**, 16900 (2011).
[4] I. Forbeaux et al., *Phys. Rev. B* **58**, 24 (1998).
[5] I. Gierz et al., *Phys. Rev. B* **81**, 235408 (2010).
[6] S. Forti et al., *Phys. Rev. B* **84**, 125449 (2011).
[7] C. Virojanadara et al., *J. Phys. D: Appl. Phys.* **43**, 37 (2010).
[8] L. Bergmann et al., *Lehrbuch der Experimentalphysik: Festkörper*, (Walter de Gruyter, Berlin, 2005).
[9] C. Riedl et al., *J. Phys. D: Appl. Phys.* **43**, 37 (2010).

STM and XPS study on self-assembled caffeine monolayers on Au(111)

M. Schulte[1,2,*], I. Baltaci[1,2], P. Roese[1,2], A. Budde[1], U. Berges[1,2] and C. Westphal[1,2]

[1] Experimentelle Physik I - Technische Universität Dortmund, Otto-Hahn-Str. 4a, 44227 Dortmund
[2] DELTA - Technische Universität Dortmund, Maria-Goeppert-Mayer-Str. 2, 44227 Dortmund

In the last decades self-assembled monolayers (SAMs) have attracted considerable attention due to their potential in applications in molecular electronics as well as chemical and biological sensors by varying electrical and structural properties [1]. Polymorphism is also an important property in pharmaceutics due to the different bioavailability of independent phases and therefore varying medical effects [2]. Caffeine shows polymorphism behavior as a solid resulting in two crystallite phases, one stable β-phase and a metastable high temperature α-phase. The latter structure was determined in 2007 [3,4]. Furthermore caffeine is best known for its impact on the human central nervous system [5]. Therefore caffeine is important for pharmaceutical application and a structural analysis of caffeine crystalline growth on different substrates in thick films was done in recent years [6,7]. So an investigation of the caffeine monolayer formation should reveal insides of the crystallite growth and give us some details about different phases. To the best of our knowledge, the formation of caffeine monolayers on metallic substrates has not been reported in literature. We report on the monolayer formation of caffeine on Au(111) to get a deeper insight into the fist growth steps of crystallite caffeine structures in different phases. To achieve this, we performed Scanning Tunneling Microscopy (STM), Low Energy Electron Diffraction (LEED) and X-ray Photoelectron Spectroscopy (XPS).

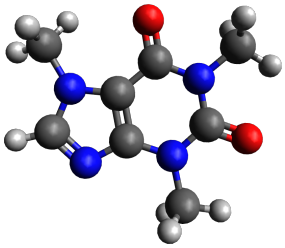

(a) Structure of caffeine. Red spheres correspond to O, white H, gray C and blue N.

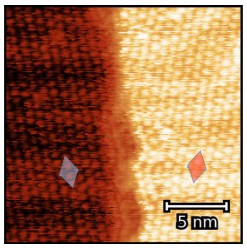

(b) 20×20 nm constant current STM image with drwan unit cells. $I_T = 16\,pA$, $U_T = -1.01\,V$.

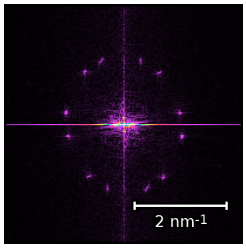

(c) 2D Fast Fourier Transformation of figure 1b.

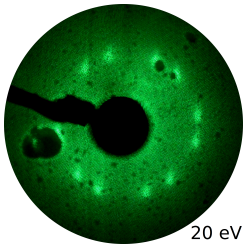

(d) LEED image of caffeine on Au(111) with an kinetic electron energy of 20 eV.

Figure 1: Results of STM and LEED analysis.

The gold substrate was cleaned to obtain the characteristic herringbone $22 \times \sqrt{3}$ reconstruction, checked by STM and LEED. Afterwards a caffeine monolayer was evaporated by molecular beam epitaxy (MBE) with a knudsen effusion cell onto the surface. STM and LEED measurements revealed two ordered hexagonal mirrored domains of caffeine molecules on the Au(111) surface with a next neighbor distance of 8.8 Å. Taking the Au(111) surface into account approximated as a hexagonal lattice neglecting the herringbone reconstruction the caffeine molecules

form a $\begin{pmatrix} 6 & 4 \\ 2 & 6 \end{pmatrix}$ and the mirrored $\begin{pmatrix} 6 & 2 \\ 4 & 6 \end{pmatrix}$ superlattice with three molecules in the unit cell and a lattice constant of 15 Å. Two different domains separated by a step edge are shown in the STM image in figure 1b. The herringbone reconstruction of the substrate is visible throughout the adsorbed film, indicating a very thin coverage. The 2D Fast Fourier Transformation (FFT) of this STM image is shown in figure 1c. It clearly reveals 12 spots of the two hexagonal domains, rotated by an angle of 22°. The presence of two domains is proven by LEED, shown in figure 1d.This image is recorded at an kinetic electron energy of 20 eV. Long range order of the caffeine molecules growing in two domains depending on the orientation of the Au(111) surface was confirmed by LEED and large scale STM images. To study the adsorbate-substrate interaction and get detailed information about the in plane molecule orientations, XPS measurements were performed at Beamline 11 at DELTA.

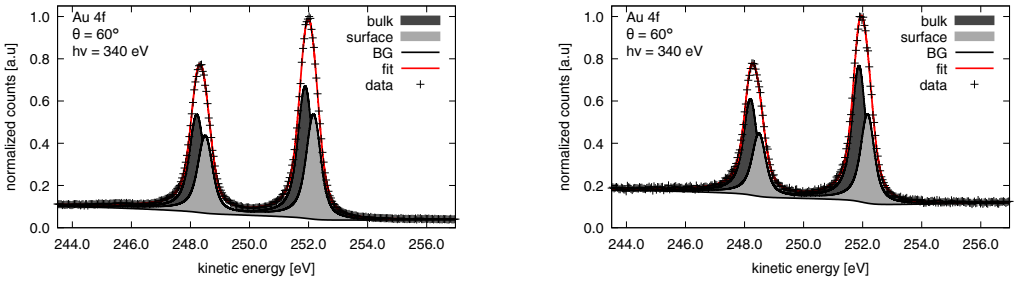

(a) Clean sample.

(b) With caffeine monolayer.

Figure 2: Au4f XPS spectra recorded at $h\nu = 340$ eV and an angle of incidence $\Theta = 60°$ for a clean sample (a) and a sample covered with caffeine (b).

For the fitting procedure convolution of Doniach-Sunjic and Gauss functions were applied for all XPS spectra. A possible substrate-adsorbate interaction was investigated by measuring the Au 4f signal for the clean and covered sample. The Au 4f spectrum of the clean sample is shown in figure 2a recorded at an photon energy of 340 eV under an angle of incidence of $\Theta = 60°$. The surface sensitivity is increased for measurements under those angles, which allows the identification af possible binding components of the surface. In figure 2b the Au 4f signal of the Au(111) surface covered with a monolayer of caffeine is shown. By comparison of both spectra, no significant differences between those measurements are visible. Therefor, we can exclude a chemical bonding of the caffeine molecules with the underlying substrate.

The molecular interactions of caffeine ($C_8H_{10}N_4O_2$) are analyzed by looking at the C1s, N1s and O1s signals as shown in figure 3. The C1s signal shown in figure 3a can be deconvoluted into three different components, which can be assigned to, a superposition of the signal the 8 carbon atoms. Also a satellite peak due to a $\pi \rightarrow \pi*$-transition was found in the signal. For the N1s signal shown in figure 3b all four nitrogen atoms in the caffeine molecule can be separated and assigned to each respective component in the spectrum. Furthermore the two oxygen atoms can not be distinguished, leading to the formation of only one component in the O 1s spectrum, shown in figure 3c. These results are in good accordance to previous XPS results of caffeine molecules in the gas phase [8]. As a conclusion one can say that the molecules only form weak molecule-molecule interaction and no strong bonding to the substrate. With this results we propose that the caffeine molecules form a two dimensional hexagonal plastic crystal

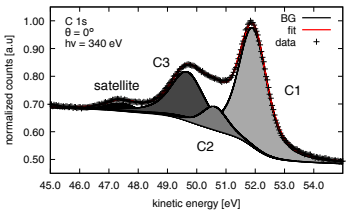

(a) C1s photoelectronspectrum with $h\nu = 340\,\mathrm{eV}$ and $\Theta = 0$ of Caffeine on Au(111)

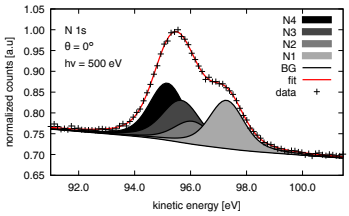

(b) N1s photoelectronspectrum with $h\nu = 500\,\mathrm{eV}$ and $\Theta = 0$ of Caffeine on Au(111)

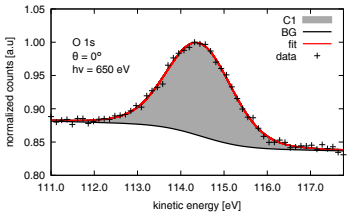

(c) O1s photoelectronspectrum with $h\nu = 650\,\mathrm{eV}$ and $\Theta = 0$ of Caffeine on Au(111)

Figure 3: XPS measurements of caffeine monolayer film on Au(111).

with dynamically disordered orientations of caffeine molecules on the Au(111) surface, which was also found for the metastable hexagonal bulk crystal of caffeine discovered by Derollez et al. [3] with two domains on Au(111) which reconstruct in a $\begin{pmatrix} 6 & 4 \\ 2 & 6 \end{pmatrix}$ and $\begin{pmatrix} 6 & 2 \\ 4 & 6 \end{pmatrix}$ superlattice. A hexagonal plastic crystal structure was also found in surface mediated crystals on different substrates like silicon, silver, soda lime glass, and silver subsurface ion-exchanged soda-lime silicate (SIMO) glasses [9].

References

[1] H. Wang et al., *Org. Electron.* **15**, 1586 (2014.)
[2] K. Raza et al., *SOJ Pharm. Pharm. Sci.* **1**, 10 (2014).
[3] P. Derollez et al., *Acta Cryst. B* **61**, 329-334 (2005).
[4] C. W. Lehmann et al., *Chem. Eur. J.* **13**, 2908-2911 (2007).
[5] A. Nehlig et al., *Brain. Res. Rev.* **17**, 139-170 (1992).
[6] O. Werzer et al., *Cryst. Growth Des.* **13**, 1322-1328 (2013).
[7] C. Röthel et al., *Cryst. Growth Des.* **15**, 4563-4570 (2015).
[8] O. Plekan et al., *J. Phys. Chem. A* **116**, 5653-5664 (2012).
[9] A. Sarfraz et al., *Cryst. Growth Des.* **12**, 583–588 (2012)

X-ray Scattering

Thermally-induced phase transitions of poly(3-hexylthiophene):*N*-substituted aromatic diimide derivatives blends

Adam Kiersnowski[1,3*], Dorota Chlebosz[1,2], Kinga Danielewicz[1], Cezary Kobyłecki[1]
Krzysztof Janus[1], Markus Mezger[2]

[1]Faculty of Chemistry, Wroclaw University of Science and Technology, Wroclaw, Poland
[2]Max Planck Institute for Polymer Research, Mainz, Germany
[3]Leibniz Institute for Polymer Research, Dresden, Germany
[*]correspondence: adam.kiersnowski@pwr.edu.pl

Experimental setup and exemplary results In this work we have studied phase transitions in the blends of poly(3-hexylthiophene) (P3HT) with naphthalene diimides (NDI) *N,N'*-substituted with either n-butyl- (NDInC4), n-hexyl- (NDInC6) or n-octyl (NDInC8) alkyl chains. In the study poly(3-hexylthiophene) (P3HT) with the molar mass of 65 kg/mol (RR=95.7%; Ossila) was used. The blends with various P3HT:NDI ratios selected on the basis of DSC results were heated and cooled within the range of 25-260°C at the ramps of 1°C/min or 2°C/min using the Linkam HFS-X350 stage, mounted with a custom, CNC-milled aluminum bracket on top of the Huber goniometer. The scattered radiation (13 keV) was recorded using either MAR345 detector (60s exposure) or Dectris Pilatus 100k detector. Based on the above experimental setup the two-dimensional diffraction patterns were measured and converted into one-dimensional I(q) profiles. Currently, the I(q) datasets recorded for the blends and pure compounds are being analyzed in order to determine crystal structure of subsequent phases resulting from the thermally-induced transitions. This analysis is done in correlation with the DSC profiles measured for each blend. The exemplary dataset recorded for the pure NDInC4 using the MAR345 detector is shown in Fig. 1.

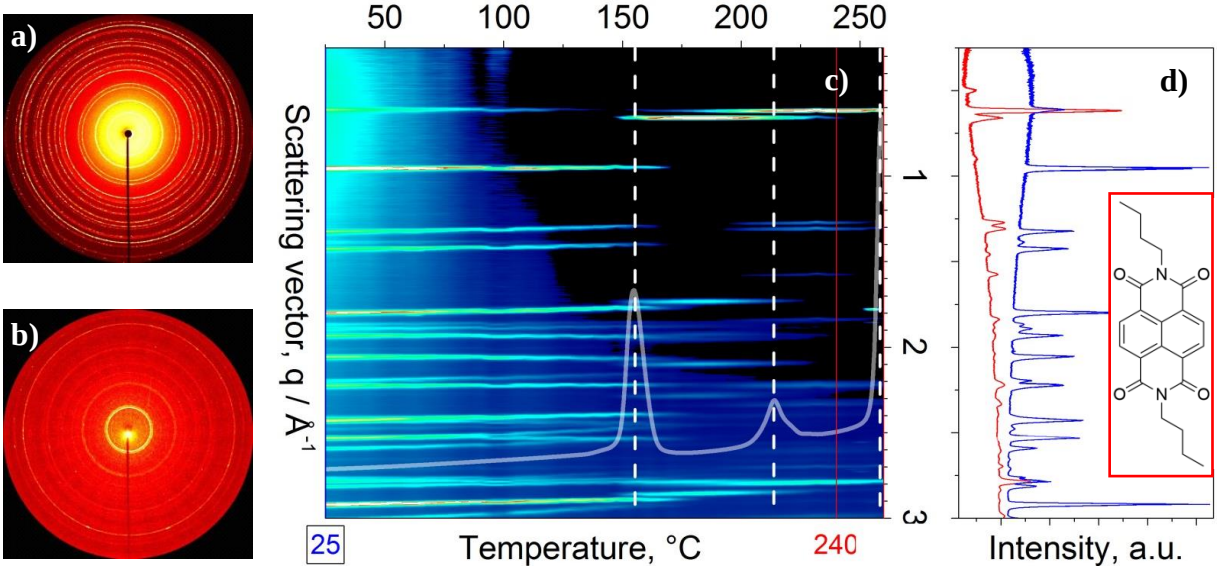

Figure 1. Two dimensional diffraction patterns recorded for the pure NDInC4 (molecule in the red box to the right) at 25°C (a), 260°C (b). Figure (c) displays intensity changes in the 1D profiles recorded during heating and the DSC trace of NDInC4 (grey solid line). Exemplary one-dimensional profiles recorded at 25 °C (blue profile) and 240°C (red profile) are shown to the right in the Figure (d). The q-scale is common for panels (c) and (d).

Acknowledgement. The project was supported through the grant UMO-2016/22/E/ST5/00472 from National Science Centre, Poland. The access to the BL9 beamline (13-17.11.2017) granted by a scientific council of DELTA synchrotron facility is gratefully acknowledged. The researchers express their gratitude to Dr. C. Sternemann and Dr. M. Paulus for their help with the beamline setup.

The pressure-dependent phase behavior of multi-lamellar DMPC vesicles containing cholesterol

Göran Surmeier, Michael Paulus, Christian Sternemann, Marc Moron, Mike Moron, Metin Tolan, and Julia Nase

Fakultät Physik/DELTA, TU Dortmund, 44221 Dortmund, Germany

Email: goeran.surmeier@tu-dortmund.de

A phospholipid bilayer is the basic component of cell membranes, which separate the intracellular and extracellular region and regulate the mass transfer between both regions in all living organisms. Lipid bilayers form different liquid-crystalline and gel-like phases depending on their composition, temperature and pressure. A typical component that regulates the structure of cell membranes is cholesterol. Due to its rigid sterol rings, it affects the mobility and order of lipid tail groups. In this experiment, we investigated the influence of cholesterol on the structure of membranes by studying the pressure-dependent phase behavior of simple model membranes. We prepared multi-lamellar DMPC (1,2-dimyristoyl-*sn*-glycero-3-phosphocholine) vesicles containing different amounts of cholesterol as model membranes and analyzed their structure with small angle X-ray scattering (SAXS).

In former experiments (see our reports from 2016 and 2017), we investigated solid-supported DMPC bi- and multilayers containing cholesterol at the solid-liquid interface between a silicon substrate and an aqueous buffer solution with X-ray reflectivity (XRR) measurements. This method enables to extract detailed vertical electron density profiles and thus provides insight into the substructure of the membrane. However, the influence of the substrate on the membrane structure is unknown. Therefore, we now determined the phase diagram of lipid bilayers forming multi-lamellar vesicles in excess water applying the same temperature, pressure steps and cholesterol concentrations as in the XRR studies to obtain a complete picture of interfacial und bulk systems.

The vesicles were prepared by dissolving DMPC and cholesterol in different ratios in chloroform. Then, the solvent was evaporated to a large extent under a gentle stream of nitrogen before it was completely removed by a desiccator. Afterwards, an aqueous buffer solution was added. To obtain a homogeneous mixture, five freeze-thaw cycles were conducted. The water content of all samples was 80 wt%. The weight ratio between cholesterol and DMPC was varied between 0 wt% and 23.1 wt% cholesterol. We applied pressures of up to 3.5 kbar at a temperature of 20 °C. The measurements were performed in a custom-made high hydrostatic pressure cell [1] at beamline BL9 at DELTA applying a photon energy of 10 keV.

Figure 1 shows the integrated SAXS data of the pressure series of pure DMPC, DMPC with 4.8 wt% and DMPC with 23.1 wt% cholesterol in a small q range around the first order Bragg reflections. The curves were fitted with one or two Pearson type VII distributions. Based on the fits, the positions of the reflections can be determined. These are directly related to the spacing d of the multi-lamellar vesicles and thus provide information about the phase behavior [2, 3]. For pure DMPC, there are two reflections indicating a coexistence of two different phases. At low cholesterol concentrations, we observe an asymmetric maximum that can be interpreted as two overlapping reflections. At high cholesterol concentrations, only one reflection remains.

Figure 2 shows how the spacing changes with increasing pressure for different cholesterol concentrations. In case of pure DMPC, the more intense reflex refers to a spacing of ~67 Å, which corresponds to the rippled gel phase $P_{\beta'}$. The second reflection indicates the presence of

domains in the $L_{\beta'}$ phase with a spacing of ~58 Å. By adding small amounts of cholesterol, the $L_{\beta'}$ phase is suppressed. Instead, we observe a weak reflection corresponding to a spacing similar to the one of the $P_{\beta'}$ phase of pure DMPC and a strong reflection indicating an even larger spacing of up to 72.8 Å. This is probably due to a separation of phases which differ in the cholesterol content, with the phase with the larger spacing being the cholesterol-rich phase. This effect was already observed for a similar phospholipid [3]. At a concentration of 4.8 wt% cholesterol, this separation is suppressed as soon as a pressure of more than 3 kbar is applied, while it is still observed in the high pressure region in case of 9.1 wt% cholesterol. Once the concentration is increased to 14.1 wt% cholesterol or higher, only one phase remains. The spacing of this phase decreases with increasing cholesterol content. As can also be seen from *figure 1*, the SAXS patterns barely change with increasing pressure at high cholesterol concentrations.
In a next step, these data will be correlated with the XRR data and will help to clearly distinguish composition-, pressure- and substrate-induced effects.

Acknowledgments: This work is supported by the Forschergruppe 1979 (**DFG-FOR1979**). We also acknowledge the Delta machine group for providing synchrotron radiation and technical support.

References: [1] C. Krywka, C. Sternemann, M. Paulus, M. Tolan, C. Royer and R. Winter, *ChemPhysChem* **9** (2008) 2809–2815. [2] J. Eisenblätter, R. Winter, *Biophys. J* . **90** (2006) 956-966. [3] R. Winter, *Biochim. Biophys. Acta, Protein Struct. Mol. Enzymol.* **1595** (2002) 160-184.

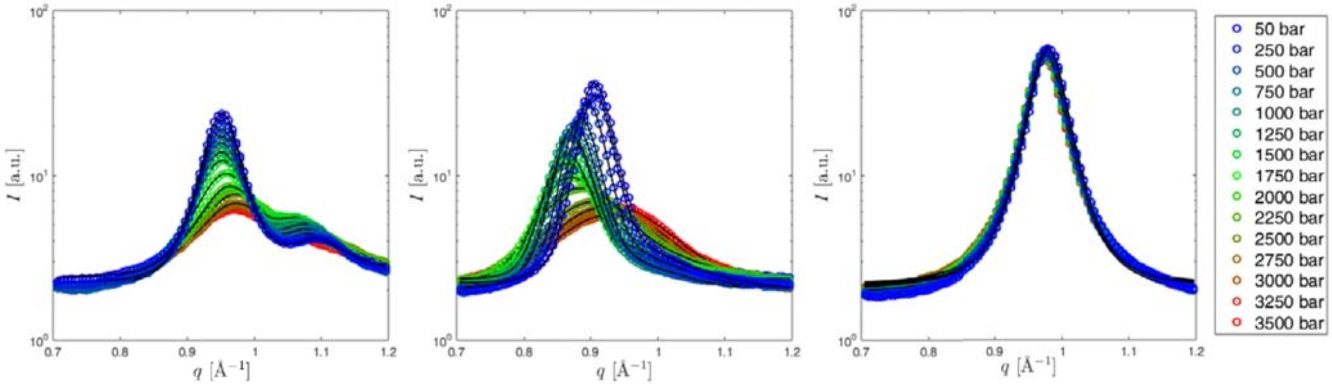

Figure 1: Integrated SAXS data (*colored*) and fits (*black*) of first order *Bragg* reflections of pure DMPC (*left*), DMPC with a cholesterol content of 4.8 wt% (*center*) and DMPC with a cholesterol content of 23.1 wt% (*right*) at different pressures.

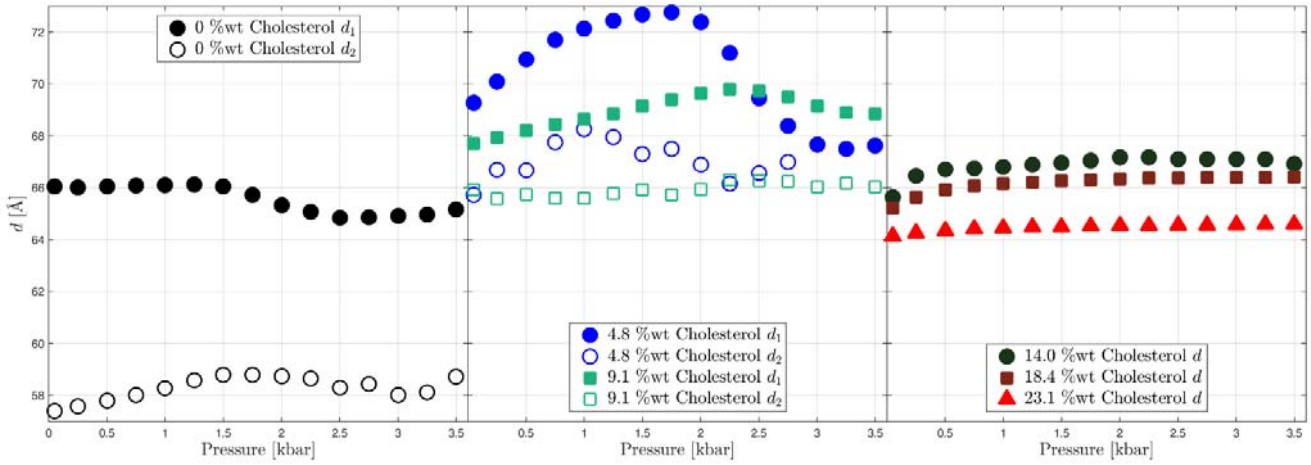

Figure 2: Pressure dependence of the spacing *d* for different cholesterol concentrations. If two reflections occur, d_1 denotes the more intense and d_2 the less intense.

Supramolecular structure of monohydroxy alcohols mixtures

Jennifer Bolle, Christian Sternemann, Michael Paulus, Christian Albers, Göran Surmeier, Fatima Mallal, Robin Sakrowski and Metin Tolan

Fakultät Physik/DELTA, Technische Universität Dortmund, 44221 Dortmund, Germany

Monohydroxy alcohols (MAs) have been scrutinized as a model of hydrogen bonded fluids. These hydrogen bonds are essential for the understanding of the microscopic structure of water, aqueous solutions and alcohols [1]. Mediated by hydrogen bonds the MAs can create ring- or chain-like supramolecular structures. The scheme in figure 1 illustrates such structures showing that the O-O distances for ring-like structures are shorter than for a chain-like arrangement. This structure formation strongly depends on the temperature. Based on the previous work further mixtures of 2E1H (2-ethyl-1-hexanol) and 4M3H (4-methyl- 3-heptanol) were investigated by X-ray diffraction (XRD) in the temperature range from 182K to 384K at beamline BL9 of the synchrotron light source DELTA (TU Dortmund, Dortmund, Germany). The corresponding setup is shown in figure 2. The investigated alcohols were purchased from Sigma Aldrich with stated purity of $\geq 99.0\,\%$. The MAs were filled without further treatment into borosilicate capillaries with 2 mm diameter. An Example of the diffraction patterns measured at an incident energy of 20 keV is shown in figure 3. These patterns exhibit two distinct peaks. The mainpeak at higher momentum transfer (q) is predominant due to the carbon-carbon correlations in the liquid. The prepeak at lower q originates from supramolecular arrangements with typical length scales larger than a single molecule. Its position reflects typical distances owing to oxygen-oxygen correlations.

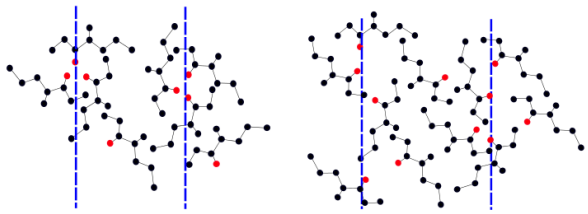

Figure 1: Scheme of ring-like and chain-like cluster-cluster arrangements. The dashed lines symbolize typical intermolecular distances.

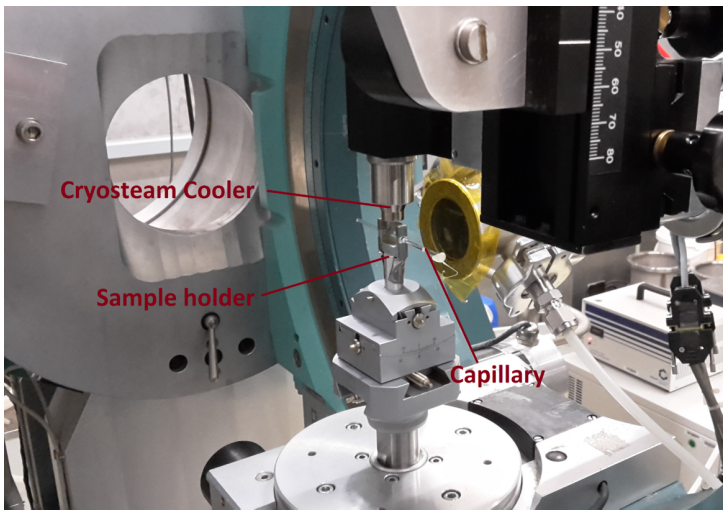

Figure 2: X-ray diffraction setup at beamline BL9 of DELTA

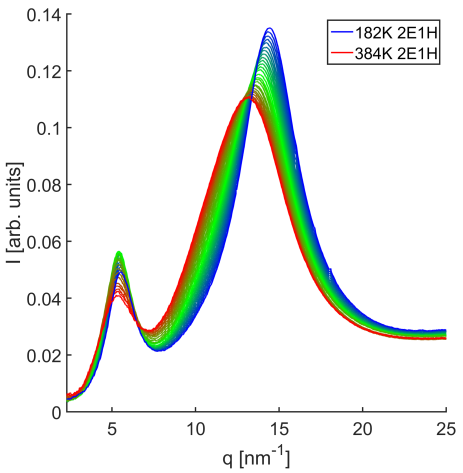

Figure 3: Diffraction patterns of 2E1H with the characteristic pre-and mainpeak

From dielectric spectroscopy it is known that 4M3H is a ring former whereas 2E1H is a chain former. Occurrence of these structures can be characterized by the Kirkwood-Fröhlich correlation factor [2]. The Kirkwood factor g_K quantifies the angle between different dipole vectors of molecules in the liquid [3]. If the Kirkwood factor is below 1, the dipoles of a supramolecular arrangement have anti-parallel orientation, as present in ring structures of the MAs. If the Kirkwood factor is above 1 the MAs form chains. In this case the dipoles have parallel orientation. Some mixtures exhibit a transition from $g_K > 1$ to $g_K < 1$ with rising temperature [4]. The corresponding transition temperature of the mixtures shifts with increasing

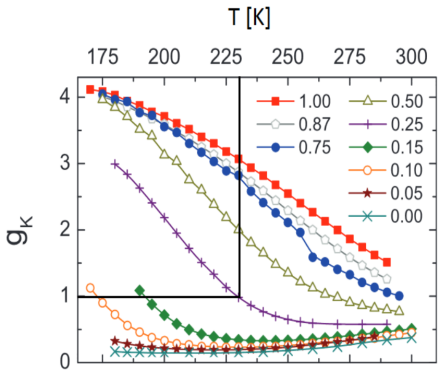

Figure 4: Results from the dielectric studies of $(2E1H)_x(4M3H)_{1-x}$ [4]

This change, indicating an increase of intermolecular distances, can only be explained by a structural change. During the cooling process (T$<$ 250K), the ring structure of 4M3H is destabilized by already small amounts of 2E1H related by increase of this distances. These transition temperatures (black dots in fig. 5) in comparison to the results of dielectric studies are shown in figure 6. The results of dielectric studies were taken from the plot in figure 4. Both show that the transition temperature increases with increasing concentration. These observations show that we can detect a crossover between the predominant species with XRD.

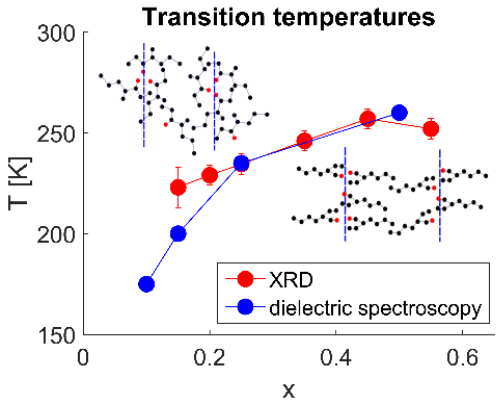

Figure 6: Transition temperature detected with dielectric spectroscopy and XRD

concentration of 2E1H to higher values, indicating a change in the predominant species from rings to chains (fig. 4). In order to compare the results of the Kirkwood factor with our XRD results, the prepeak position of the diffraction patterns was evaluated. This prepeak analysis of $(2E1H)_x(4M3H)_{1-x}$ is shown in figure 5 and gives a hint for the structural crossover. The prepeak position of the pure substances (2E1H and 4M3H) increases with decreasing temperature, indicative for a reduction of the intermolecular distances between supramolecular arrangement. Surprisingly the mixtures (x=0.15,0.20,0.25,0.35,0.45,0.55) show a different course. The peak position increases similar to the position of the pure substances with decreasing temperature until the sign of the slope changes. This is illustrated by the black arrows in figure 5.

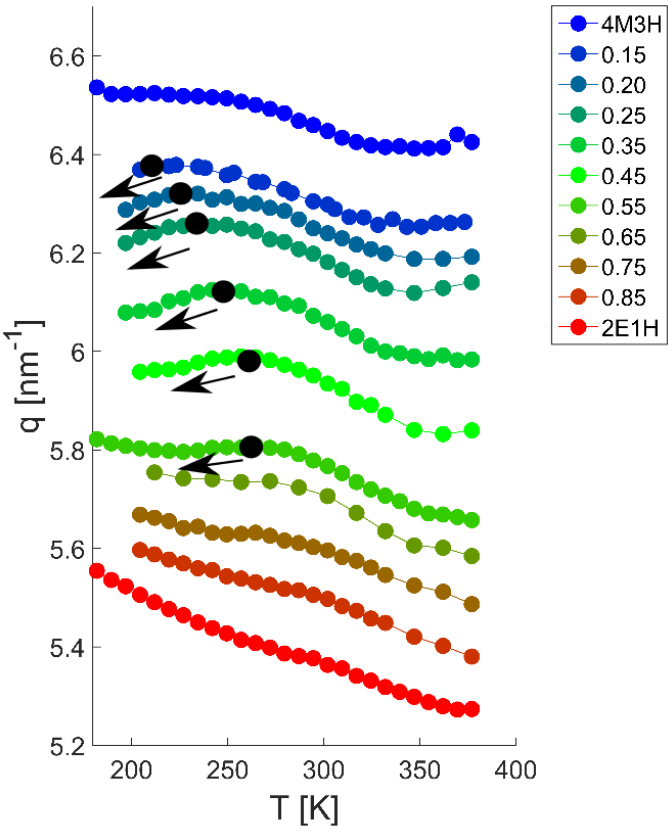

Figure 5: Prepeak position of $(2E1H)_x(4M3H)_{1-x}$ at temperatures from 182K to 380K

Reference

[1] Kaatze, U., Behrends, R., & Pottel, R. (2002). Hydrogen network fluctuations and dielectric spectrometry of liquids. Journal of Non-Crystalline Solids, 305(1), 19-28.
[2] Dannhauser, W. (1968). Dielectric study of intermolecular association in isomeric octyl alcohols. The Journal of Chemical Physics, 48(5), 1911-1917.
[3] Roland Böhmer, Catalin Gainaru, & Ranko Richert. Structure and dynamics of monohydroxy alcohols Milestones towards their microscopic understanding, 100 years after Debye. In: Physics Reports 545.4 (2014), pp. 125195.
[4] Bauer, S., Wittkamp, H., Schildmann, S., Frey, M., Hiller, W., Hecksher, T., & Böhmer, R. (2013). "Broadband dynamicsin neat4-methyl-3-heptanol andin mixtureswith2-ethyl-1-hexanol. " The Journal of chemical physics, 139(13), 134503.

Acknowledgement

We would like to thank the Deutsche Forschungsgemeinschaft(DFG-STE1079/4-1, DFG-STE1079/2-1, DFG-FOR1979) for funding and DELTA for providing synchrotron radiation and technical support. And the financial support by the Cluster of Excellence RESOLV (EXC 1069) funded by Deutsche Forschungsgemeinschaftis gratefully acknowledged.

Impact of pressure on the conformational stability of hen egg-white lysozyme in crowded solutions

Karin Julius[1], Mirko Elbers[1], Michael Paulus[1], Metin Tolan[1], and Roland Winter[2]

[1] *Fakultät Physik / DELTA, Technische Universität Dortmund, 44227 Dortmund, Germany*

[2] *Fakultät für Chemie und Chemische Biologie, Technische Universität Dortmund, 44227 Dortmund Germany*

In living cells, the rates, equilibria and mechanisms of biochemical reactions as well as the biomolecules' conformational stability are strongly influenced by the high fractional occupancy (> 30 %) of 'background' species like osmolytes, proteins, nucleic acids and biopolymers. [1,2] Investigating how the shape, size and concentration of such crowding agents modulate intermolecular interactions between biomolecules, such as proteins, is highly relevant to understand their dynamics, phase behavior and spatiotemporal organization *in cellulo*. [3–11] The pressure dependent intermolecular interaction potential, governing the spatial distribution of the protein hen egg-white lysozyme in solution, can reportedly be derived by applying small-angle X-ray scattering (SAXS) in combination with a liquid-state theory approach. [12–14] Knowledge of potential crowder-induced conformational changes of the protein at ambient and at elevated pressures is crucial for the advanced analysis of high-pressure SAXS data of dense aqueous lysozyme-crowder mixtures in order to explore the effects of different levels of nano- and macromolecular crowding on the pressure-dependent protein pair-interaction potential [14]. On the one hand, the pressure variable has been applied owing to its usefulness in fine-tuning intermolecular distances, on the other hand owing to its relevance in understanding the conformational stability of proteins in organisms thriving at kbar pressure in the deep sea.

The aim of the experiment was to exclude potential pressure-dependent changes in the folded state of the protein lysozyme in the presence of crowder molecules of various sizes, mimicking crowding scenarios as encountered in the heterogeneous biological cell. From the SAXS intensity of a dilute solution of non-interacting lysozyme molecules (c_{lys} ~ 1 % (w/v)), the scattering of a single lysozyme molecule averaged over its orientation can be modeled, yielding the average shape and size of the protein. High-pressure SAXS measurements were carried out on diluted 1 % (w/v) lysozyme in 25 mM Bis-Tris buffer (pH 7) with 15 % (w/v) of small (PEG200, PEG 600), mid-level (PEG 2000) and large (PEG 35000) polymer polyethylene glycol (PEG) added to the solution.
At beamline bl9, the wavelength of the incident photon beam was λ = 1.2399 Å, yielding a wave vector transfer $q = (4\pi/\lambda)\sin(\theta/2)$ of $0.238 < q < 5.769$ nm^{-1} at a distance of 1.103 m between the MAR345 image plate detector and the sample. Here, 2θ describes the scattering angle. The exposure time was 10 min. In order to generate high hydrostatic pressures up to 3.5 kbar in the sample environment, a custom-built high pressure sample cell [15], sealed with flat diamond windows, was employed. Before each measurement, the protein was freshly dissolved at the concentration 1% (w/v) in neat buffer as well as in the 15 % (w/v) PEG + buffer solutions, respectively. The buffer ensures stability of the pH value at all conditions studied. The pure lysozyme-buffer solutions, lysozyme-crowder compositions and the corresponding background solvent scattering were measured at 25 °C in an overall pressure range from 1 bar to 3.5 kbar. Subtraction of the corresponding background solution scattering signal yields the azimuthally averaged SAXS profiles of the solute (protein).
The scattering data of the dilute lysozyme solution and lysozyme + PEG mixtures were refined using the program package PRIMUS [16] as well as by employing the inverse Fourier transformation program GNOM [17,18], yielding the real space distance distribution $P(r)$, as well as the averaged radius of gyration, R_G, of the protein (see Fig. 1).
Employing small-angle X-ray scattering, we have successfully quantified the protein's conformational

stability over a wide range of pressures at various crowding scenarios. In good agreement with literature data, [14] lysozyme is conformational stable with a constant radius of gyration of 1.45 ± 0.05 nm in the whole pressure range and regardless of the respective crowding additive. It is adequately described by the form factor,$\langle P(q)\rangle$, of a prolate ellipsoid of revolution of the semi-axes a = 1.57 nm and b = 2.42 nm.

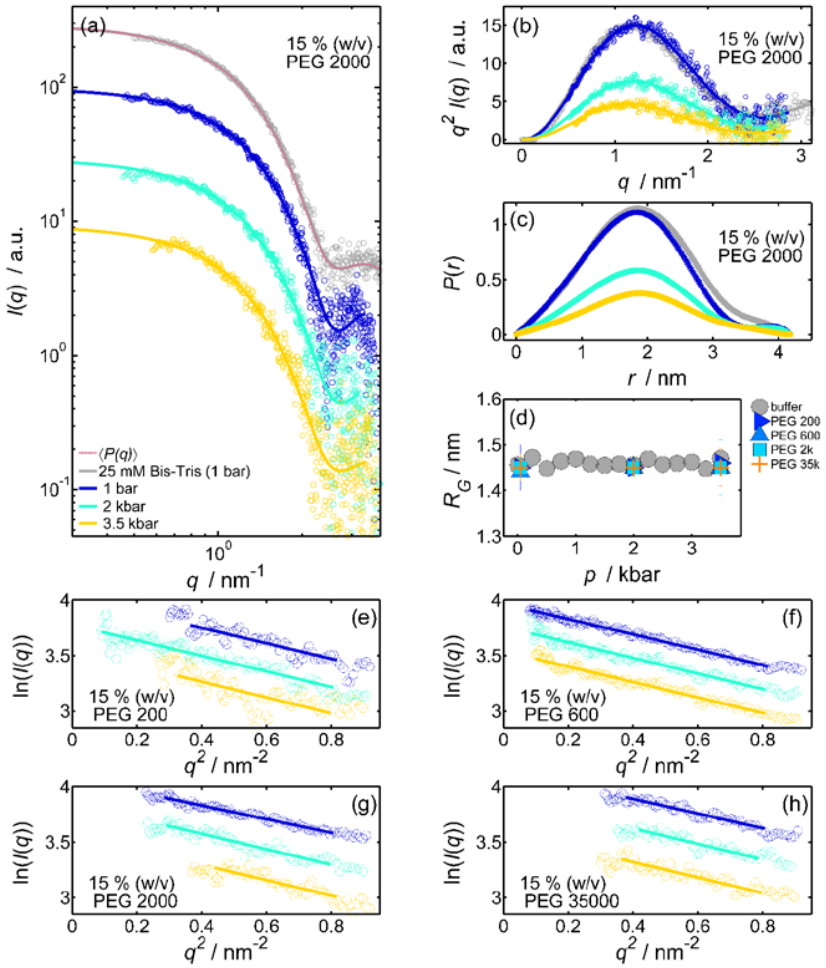

Figure 1. (a) Experimental SAXS curves of 1% (w/v) lysozyme dissolved in 25 mM Bis-Tris + 15% (w/v) PEG 2000 aqueous solution (pH 7), collected at 25 °C in the pressure range from 1 – 3500 bar. The corresponding refinements (*solid lines*), obtained by employing the program GNOM [17,18], as well as the theoretical scattering of a prolate ellipsoid of revolution $\langle P(q)\rangle$ (*magenta*) are depicted as well for reference (b) SAXS data and refinement plotted in the Kratky presentation (q vs. $q^2I(q)$) for selected pressures. (c) Radial pair-distance distribution function, $P(r)$, as a function of pressure. (d) Pressure dependence of the protein's radius of gyration, R_G, in pure 25 mM Bis-Tris buffer solution (pH 7, 25 °C) and in the presence of 15% (w/v) polymer of various molecular weights, derived from the scattering data. (e)-(h) Guinier plot of the 1% (w/v) lysozyme + 15 % (w/v) PEG (200, 600, 2k, 35k) solution scattering intensities for 1 bar, 2 kbar and 3.5 kbar, with the corresponding refinements (*solid lines*) made by PRIMUS [16].

[1] R. Ellis and A. Minton, Nature **425**, 27 (2003).
[2] S. B. Zimmerman and S. O. Trach, J. Mol. Biol. **222**, 599 (1991).
[3] S. F. Banani, H. O. Lee, A. A. Hyman, and M. K. Rosen, Nat. Rev. Mol. Cell Biol. **18**, 285 (2017).
[4] M. S. Long, C. D. Jones, M. R. Helfrich, L. K. Mangeney-Slavin, and C. D. Keating, Proc. Natl. Acad. Sci. **102**, 5920 (2005).
[5] A. P. Minton, J. Cell Sci. **119**, 2863 (2006).
[6] A. P. Minton, Biophys. J. **88**, 971 (2005).
[7] H. X. Zhou, Arch. Biochem. Biophys. **469**, 76 (2008).
[8] R. J. Ellis, Trends Biochem. Sci. **26**, 597 (2001).
[9] B. van den Berg, R. J. Ellis, and C. M. Dobson, *Effects of Macromolecular Crowding on Protein Folding and Aggregation.* (1999).
[10] M. S. Cheung, D. Klimov, and D. Thirumalai, Proc Natl Acad Sci U S A **102**, 4753 (2005).
[11] R. J. Ellis, in *Mol. Asp. Stress Response Chaperones, Membr. Networks*, edited by P. Csermely and L. Vígh (Springer New York, New York, NY, 2007), pp. 1–13.
[12] K. Julius, J. Weine, M. Berghaus, K. Nico, M. Gao, M. Paulus, M. A. Schroer, M. Tolan, and R. Winter, 1 (2018).
[13] M. A. Schroer, Y. Zhai, D. C. F. Wieland, C. J. Sahle, J. Nase, M. Paulus, M. Tolan, and R. Winter, Angew. Chem. Int. Ed. **50**, 11413 (2011).
[14] M. A. Schroer, J. Markgraf, D. C. F. Wieland, C. J. Sahle, J. Möller, M. Paulus, M. Tolan, and R. Winter, Phys. Rev. Lett. **106**, 2 (2011).
[15] C. Krywka, C. Sternemann, M. Paulus, M. Tolan, C. Royer, and R. Winter, Chem. Phys. Chem. **9**, 2809 (2008).
[16] P. V Konarev, V. V Volkov, A. V Sokolova, M. H. J. Koch, and D. I. Svergun, J. Appl. Crystallogr. **36**, 1277 (2003).
[17] D. I. Svergun, J. Appl. Crystallogr. **25**, 495 (1992).
[18] B. D. I. Svergun, A. V Semenvuk, and L. A. Feigin, Acta Crystallogr. Sect. A **44**, 244 (1988).

Pressure-induced phase separation in silica nanoparticle-polymer solutions

Marc Moron, Julian Schulze, Michael Paulus, Julia Nase, Mike Moron, Philippe Poulet and Metin Tolan
Fakultät Physik/DELTA, TU Dortmund, 44221 Dortmund, Germany

We investigated the pressure-dependent phase behavior of silica nanoparticle-polyethyleneglycol mixtures for various polymer sizes and concentrations using the small-angle X-ray scattering (SAXS) technique. Dependent on the polymer concentration, the system shows two phase transitions. For low polymer concentration, it is in the homogenous phase in which the nanoparticles are evenly distributed. With increasing polymer concentration, it undergoes a liquid-liquid phase separation (LLPS). In this phase, the particles form little drops with high nanoparticle concentration surrounded by areas of low nanoparticle concentration. Further increase leads to a reentrant transition into the homogeneous phase [1].
This phase behavior can be explained by depletion effects. The non-adsorbing polymers surrounding the nanoparticles cause an osmotic pressure. Every nanoparticle has a depletion zone in which the center of the polymers cannot enter. If the distance between two particles is small, the depletion layers overlap and that results in an anisotropic osmotic pressure, which causes an attractive force between the nanoparticles and, dependent on the polymer concentration, to phase separation. The mechanism behind this reentrant phase behavior is still not fully understood. Kumar et. al supposed that increasing polymer concentration leads to a dominant polymer-polymer repulsion.
In [2] it was shown that the phase transition back into the homogenous phase also occurs if the system is pressurized. Aim of this work is to increase the understanding of this effect by investigating the phase behavior dependent on polymer size and concentration. With SAXS, it is possible to determine pair potentials and obtain information about the interparticle interaction in the two different phases.

The experiments were performed at beamline BL9 of DELTA at a photon energy of 10 keV. The observed range of polyehtyleneglycol (PEG) concentration reaches from 10^{-4} wt.% to 15 wt.%, whereas the silica nanoparticle concentration amounts to 1 wt.%.
In the considered pressure range of 1 bar to 3500 bar, the reentrant phase behavior only occurs for polymer concentrations above 5 wt.%. The samples were pressurized in a homemade high pressure cell [3].

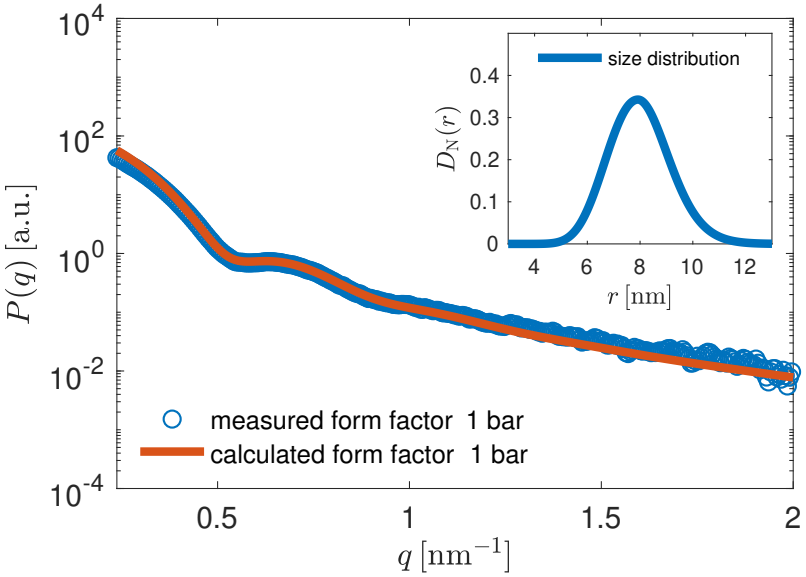

Fig.1: *form factor of the nanoparticles at 1 bar.*

First we determined the form factor $P(q)$ of the nanoparticles which is shown in **Fig. 1.**

For the scattering intensity in a SAXS experiment the following relation holds:

$$I(q) = P(q) \cdot S_{\text{eff}}(q)$$

By measuring the form factor, we were able to determine the effective structure factor $S_{\text{eff}}(q)$ and obtain information about the interparticle interaction dependent on polymer concentration, polymer weight and hydrostatic pressure. **Fig. 2** shows the structure factor for a sample containing 15 wt% PEG6k and 1 wt% silica nanoparticles at elevated pressures. One can see that

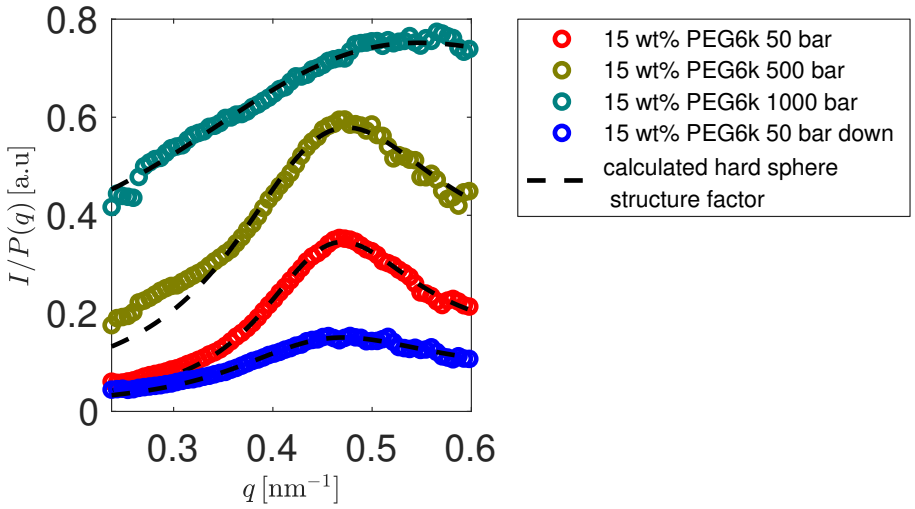

Fig.2: *Structure factor for 15 wt% PEG6k at elevated pressures.*

the maximum in the structure factor visible at low pressures disappears at 1000 bar. This is related to a loss of order. At this pressure, the system undergoes a transition into the homogeneous phase. With this procedure we were able to determine the pressure-dependent phase diagram shown in **Fig. 3**. The phase diagram determined in [2] shows higher pressures for the phase transition due to instability of the samples.

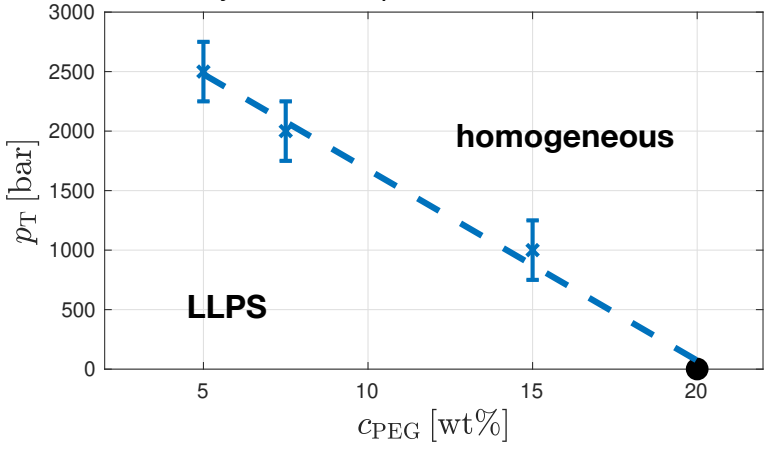

Fig.3: *phase diagram for PEG6k.*

We would like to thank the DELTA machine group for providing synchrotron radiation and for technical support.

References

[1] Sugam Kumar et al. „Structure and interaction in the polymer-dependent reentrant phase behavior of a charged nanoparticle solution“. In: *Phys. Rev. E* 90 (4 Okt. 2014), S. 042316.
[2] Julian Schulze. "Das Phasenverhalten Kolloidaler Systeme Unter Druck." Doctoral Dissertation, TU Dortmund, 2017.
[3] Christina Krywka et al. „The small-angle and wide-angle X-ray scattering set-up at beamline BL9 of DELTA“. In: *Journal of Synchrotron Radiation* 14.3 (Mai 2007), S. 244–251.

Pressure stability of a chaperonin protein complex

Michel Jaworek, Irena Kiesel, Mimi Gao, Roland Winter
Physikalische Chemie 1, TU Dortmund

Scientific background

Chaperonins are oligomeric proteins that play an essential role in assisting protein folding by transiently encapsulation of nascent proteins in an ATP-driven mechanism to prevent misfolding or aggregation.
Furthermore, the effects of different types of stress on proteins, like high temperature and hydrostatic pressure, can be counteracted by the chaperonin´s support of correct refolding.
The complex consists of a large double-ring structure stacked back to back enclosing a central cavity with its lid-like cofactor. Numerous biochemical and structural studies have been carried out for the heat shock protein complex (chaperonin) GroEL/ES of *Escherichia coli*, which belongs to the Group I chaperonins.[1,2]
Previous studies regarding pressure effects on the GroEL/ES complex have shown that under high hydrostatic pressure dissociation of the oligomeric chaperonin may be observed.[3] SAXS measurements, as an orthogonal method to FTIR (Fourier-transform infrared spectroscopy), was performed here to reveal the pressure stability of the complex regarding shape and size.

Experiment

Small-angle X-ray scattering (SAXS) experiments were performed at beamline BL9 using a home-built high-pressure sample cell with flat diamond windows.[4,5] The energy used was 10 keV, corresponding to a wavelength of λ = 0.12 nm. An image plate detector MAR345 (d = 345 mm, 100 µm pixel size) was exposed 15 min per measurement. The sample-to-detector distance was calibrated with silverbehenate. Sample solutions of a concentration of 25 mg/mL protein, GroEL:GroES 2:1, were prepared freshly in buffer (50 mM Tris HCl, 10 mM $MgCl_2$, 10 mM KCl). Additionally, a sample with the same concentrations and additional 3 mM ATP was measured. The temperature was set to T = 50 °C, the pressure range covered was 1 bar to 3500 bar. Data were treated with fit2D, matlab and analyzed with SASfit.

Results and Discussion

The measured SAXS curves (a) without and (c) with 3 mM ATP as a function of hydrostatic are shown in Figure 1. The lines are refined curves corresponding to the pair-distance distribution $p(r)$ displayed in (b) without and (d) with 3 mM ATP. In both cases, with and without ATP, oscillations are visible at low pressures and become weaker at higher pressures. The overall shape of $p(r)$ is similar regardless of the presence of ATP. The maximum in $p(r)$ becomes smaller with hydrostatic pressure, whereas the shape seems to remain stable, only pair distances between 15 and 20 nm were not detected at pressures above 1000 bar (which might be due to the noisy scattering curve and limited q-range for Fourier-transformation). The amplitude of $p(r)$ is determined by the electron density contrast between protein and the

surrounding water. As the water is compressed at high hydrostatic pressures, the electron density of the surrounding water increases and the contrast becomes weaker. This explains the decreasing intensity of $p(r)$.

In conclusion, the protein complex GroEL/GroES seems to be stable against hydrostatic pressure in the range from 1 bar to 3500 bar at 50 °C, as well as in presence of ATP.

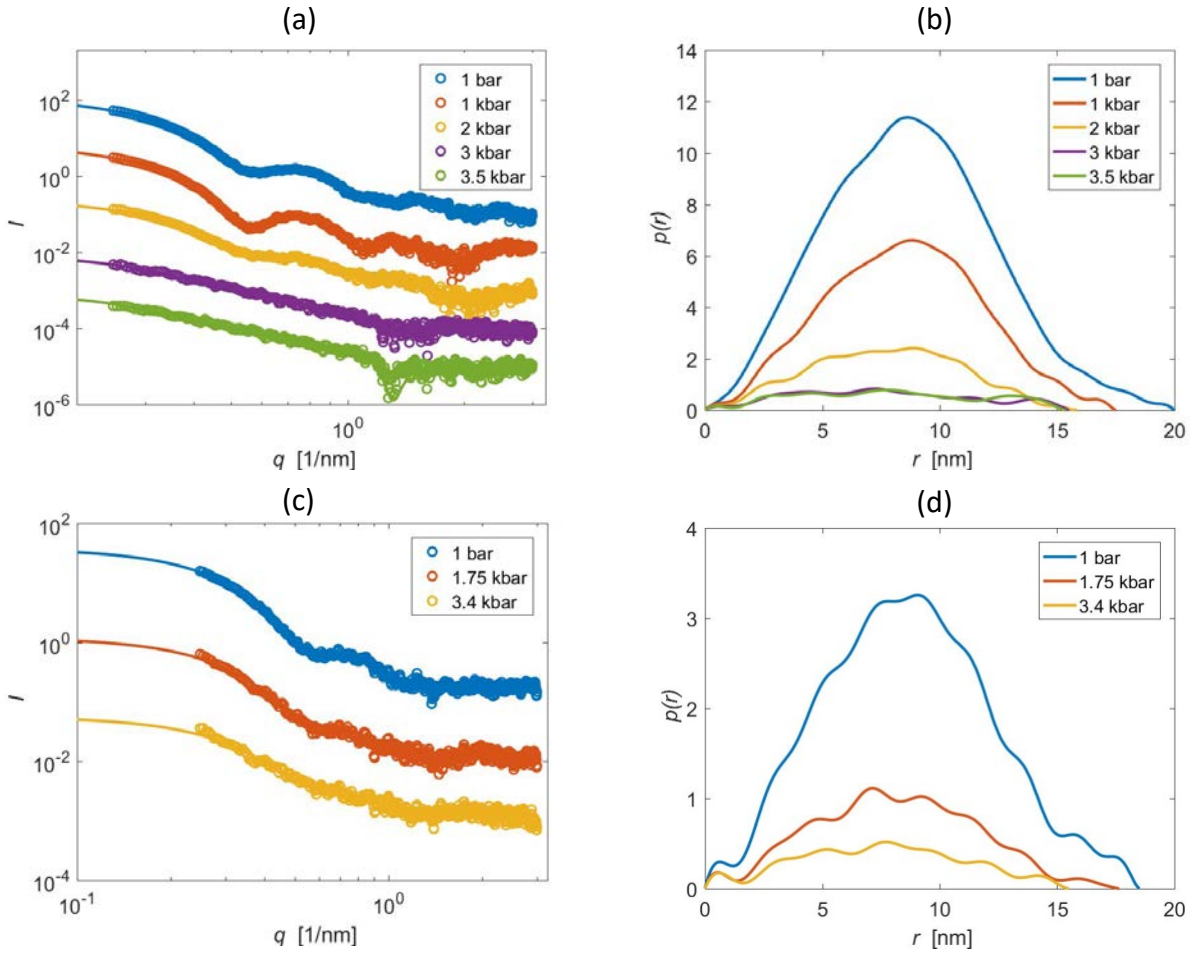

Fig. 1: SAXS curves of the GroEL/GroES complex (a) without and (c) with 3 mM ATP as a function of hydrostatic pressure. The lines represent refined scattering curves corresponding to pair-distance distribution functions $p(r)$ (b) in the absence and (d) in the presence of 3 mM ATP.

References

[1] F. U. Hartl, M. Hayer-Hartl, *Science* **2002**, *295*, 1852–1858.
[2] D. Balchin, M. Hayer-Hartl, F. U. Hartl, *Science* **2016**, *353*, aac4354.
[3] M. Panda, J. Ybarra, P. M. Horowitz, *Biochemistry* **2002**, *41*, 12843–12849.
[4] C. Krywka, M. Paulus, C. Sternemann, M. Volmer, A. Remhof, G. Nowak, A. Nefedov, B. Pöter, M. Spiegel, M. Tolan, *J. Synchrotron Radiat.* **2005**, *13*, 8–13.
[5] C. Krywka, C. Sternemann, M. Paulus, M. Tolan, C. Royer, R. Winter, *ChemPhysChem* **2008**, *9*, 2809–2815.

Acknowledgment :

The authors thank DELTA for experimental time at beamline BL9. Special thanks to M. Paulus and C. Sternemann for their support at the beamline and G. Surmeier with the high-pressure setup. We are grateful for experimental help by M. Manisegaran, J.-M. Knop, S. Bornemann and M. Herzog. IK thanks for financial support by the Cluster of Excellence RESOLV (EXC 1069).

$A^{I}SeC_2H$ with A^{I} = K, Rb, Cs: Crystalline Compounds with the Elusive $^{-}$Se-C≡C-H Anion

M. Hetzert, M. Werker, and U. Ruschewitz*

Department für Chemie, Universität zu Köln, 50939 Köln, Germany

**email: uwe.ruschewitz@uni-koeln.de*

Alkali metal acetylides of composition $A^{I}C_2H$ and $A^{I}_2C_2$ (A^{I} = Li-Cs) have been known for more than 100 years.[1] About 20 years ago it was our group that introduced ternary acetylides of composition $A^{I}_2M^{0}C_2$ and $A^{I}M^{I}C_2$ as a new class of compounds at the boundary between insulators and semiconductors.[2] Especially the compounds of composition $A^{I}_2PdC_2$ have attracted some attention in recent years as possible photocathode materials.[3] In these calculations even better workfunction values were calculated for ternary tellurium compounds.[3] Therefore we have started to react the acetylides $A^{I}C_2H$ and $A^{I}_2C_2$ with group 16 elements (S, Se, Te). By the reaction of $A^{I}C_2H$ (A^{I} = K, Rb, Cs) with selenium in liquid ammonia we obtained well-crystallized powders, which were indexed in orthorhombic unit cells.[4] The structural solution and refinement, which was based on synchrotron powder diffraction data obtained at BL 9 (*Pilatus 100K* detector) at ambient conditions (Figure 1a)), revealed the formation of a linear $^{-}SeC_2H$ anion (Figure 1b)), which is unprecedented in crystalline compounds up to now. In the crystal structure the cations and anions are arranged in a herringbone-type motif (*Cmc*2_1, *Z* = 4), see Figure 1b).

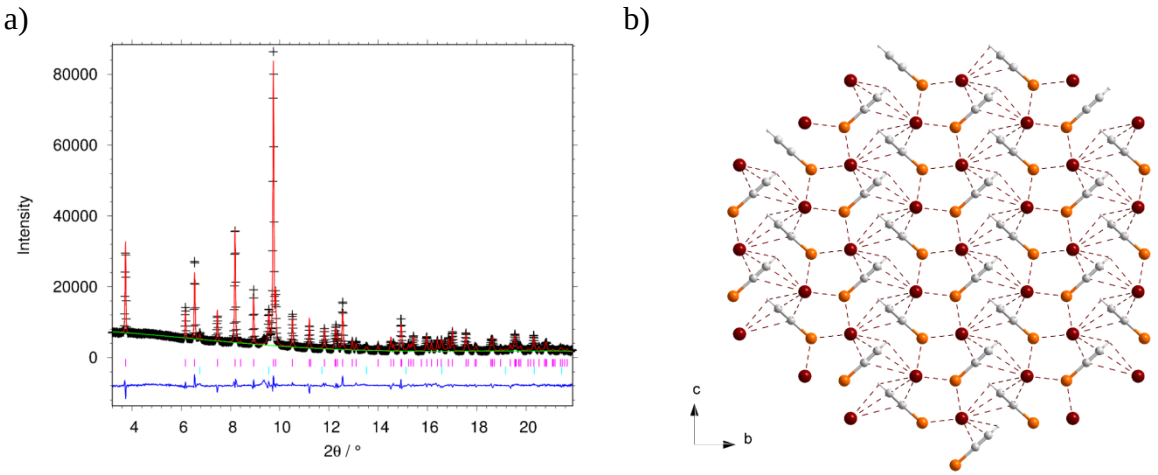

Figure 1: *a) Rietveld refinement of $KSeC_2H$ (BL 9 data); b) crystal structure of $KSeC_2H$.*

The formation of the linear $^{-}SeC_2H$ anion was confirmed by extensive IR spectroscopic investigations under inert conditions (the spectrometer was housed in a glovebox), as the $A^{I}SeC_2H$ compounds are highly sensitive to air and moisture. In Figure 2a) the resulting spectra are shown. The prominent bands at ~3250 cm^{-1}, ~1970 cm^{-1}, and ~540 cm^{-1} can be assigned to the C-H, C-C, and C-Se stretching vibrations, which is corroborated by DFT calculations of these spectra (cooperation with *Reber* group, Montreal). In Figure 2b)

exemplarily the DSC/TGA curves of $RbSeC_2H$ are shown. The mass loss is in excellent agreement with the release of one acetylene molecule according to:

$$2\ RbSeC_2H \rightarrow Rb_2Se_2(C_2) + C_2H_2(g).$$

The evolution of acetylene was also confirmed by GC analysis of the evolved gases. Similar results were obtained for $KSeC_2H$ and $CsSeC_2H$. However, the crystal structure of the reaction products $A^ISe_2(C_2)$ is still unsolved, although all compounds could be indexed in small cubic unit cells (e.g. $K_2Se_2(C_2)$: a = 4.203 Å). It is the intention to follow this decomposition reaction in situ in an upcoming beamtime at BL9 to shed some light upon the nature of these unusual compounds.

Furthermore the crystal structure of the sodium compound $NaSeC_2H$ needs to be clarified. The diffraction pattern was indexed in a cubic unit cell (a = 7.044 Å) and from the unit cell volume (V = 349.5 $Å^3$) Z = 4 was estimated. However, no reasonable structural model could be developed with cubic symmetry, so that disorder of the anions must be assumed. Low temperature measurements shall be conducted to confirm this assumption and to clarify the crystal structure of $NaSeC_2H$.

a) b)

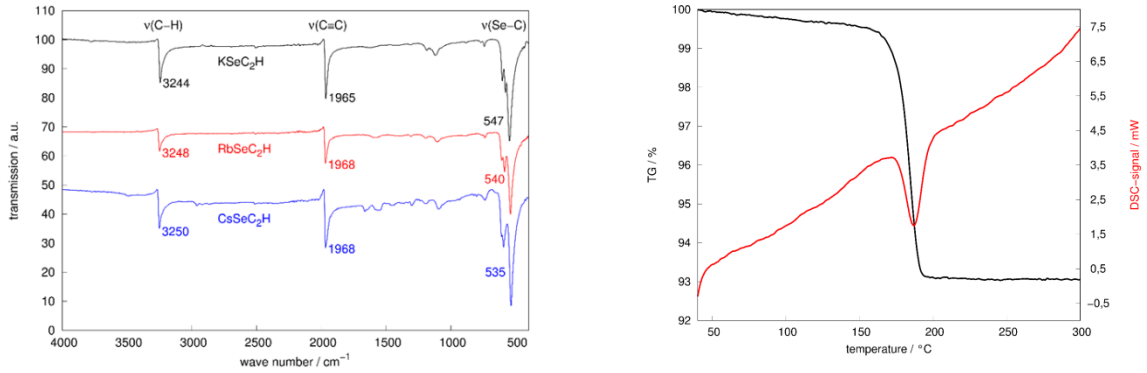

Figure 2: *a) IR spectra of A^ISeC_2H (A^I = K, Rb, Cs) recorded under inert conditions; b) DSC/TGA curves of $RbSeC_2H$.*

References

[1] U. Ruschewitz, *Coord. Chem. Rev.* **2003**, *244*, 115-136.

[2] U. Ruschewitz, *Z. Anorg. Allg. Chem.* **2006**, *632*, 705-719.

[3] J. Z. Terdik, K. Németh, K. C. Harkay, J. H. Terry, Jr., L. Spentzouris, D. Velázquez, R. Rosenberg, G. Srajer, *Phys. Rev. B* **2012**, *86*, 035142.

[4] M. Hetzert, M. Werker, U. Ruschewitz, *Angew. Chem.* **2018**, DOI: 10.1002/anie.201810910.

BL9-Publications U. Ruschewitz and Co-workers

Articles

[1] M. Hetzert, M. Werker, U. Ruschewitz
$A^{I}SeC_2H$ with A^{I} = K, Rb, Cs: crystalline compounds with the elusive $^{-}$Se-C≡C-H anion
Angew. Chem. **2018**, DOI: 10.1002/anie.201810910.

[2] C. Stastny, B. Dolfus, C. T. Brombach, D. Dresen, S. Disch, R. Glaum, U. Ruschewitz
New 2D and 3D Coordination Polymers by Dehydration of $^{1}_{\infty}[M^{II}(tF\text{-}BDC)(H_2O)_4]$ with $M^{II} = Zn^{2+}$, Co^{2+}, Ni^{2+} and *tF*-BDC^{2-} = tetrafluoroterephthalate
Z. Anorg. Allg. Chem. **2018**, DOI: 10.1002/zaac.201800228.

[3] M. Duchardt, S. Neuberger, U. Ruschewitz, T. Krauskopf, W. G. Zeier, J. Schmedt auf der Günne, S. Adams, B. Roling, S. Dehnen
The Superion Conductor $Na_{11.1}Sn_{2.1}P_{0.9}Se_{12}$: Lowering the Activation Barrier of Na^{+} Conduction in Quaternary 1-4-5-6 Electrolytes
Chem. Mater. **2018**, *30*, 4134-4139.

Poster contributions

[1] M. Hetzert, U. Ruschewitz, *Ternary Acetylides with Main Group Elements*, 19. Vortragstagung der Fachgruppe für Festkörperchemie und Materialforschung und der Wöhler-Vereinigung für Anorganische Chemie, Regensburg, 24.09.-27.09.2018 (poster presentation)..

[2] M. Werker, U. Ruschewitz, *Oxidative C-C Coupling in Solids*, 19. Vortragstagung der Fachgruppe für Festkörperchemie und Materialforschung und der Wöhler-Vereinigung für Anorganische Chemie, Regensburg, 24.09.-27.09.2018 (poster presentation).

[3] U. Ruschewitz, *Crystalline Compounds with the Unusual HC_2Se^{-} Anion*, 19. Vortragstagung der Fachgruppe für Festkörperchemie und Materialforschung und der Wöhler-Vereinigung für Anorganische Chemie, Regensburg, 24.09.-27.09.2018 (oral presentation).

Doctoral thesis

[1] H. A. Schwartz, *Metal-Organic Frameworks as Crystalline Porous Hosts for Photoactive Molecules*, Köln **2018**.

[2] C. Stastny, *Synthese und Charakterisierung von MOFs mit fluorierten Biphenyltetracarboxylat-Linkern*, Köln **2018**.

High-pressure effects on protein-modified polyelectrolyte multilayers studied by X-ray reflectometry

Artem Levin,[a] Süleyman Cinar,[a] Hasan Cinar,[a] Michael Paulus,[b] Julia Nase,[b] Claus Czeslik[a]

[a] Fakultät für Chemie und Chemische Biologie, Technische Universität Dortmund, D-44221 Dortmund, Germany.

[b] Fakultät Physik / DELTA, Technische Universität Dortmund, D-44221 Dortmund, Germany.

Polyelectrolyte multilayers (PEMs) are easily prepared by the layer-by-layer deposition technique [1]. A protein can replace the polycation or polyanion layers depending on its net charge. Here, we use calmodulin (CaM), which has a strong negative net charge of -15 at neutral pH values and can thus be combined with a polycation, such as poly(allylamine hydrochloride) (PAH) [2] and poly(diallyldimethylammonium chloride) (PDDA) (Fig. 1). Each PEM has been prepared with Ca^{2+} saturated CaM (holo-CaM). The successful build-up of the PEMs has been verified by X-ray reflectivity data (Fig. 2).

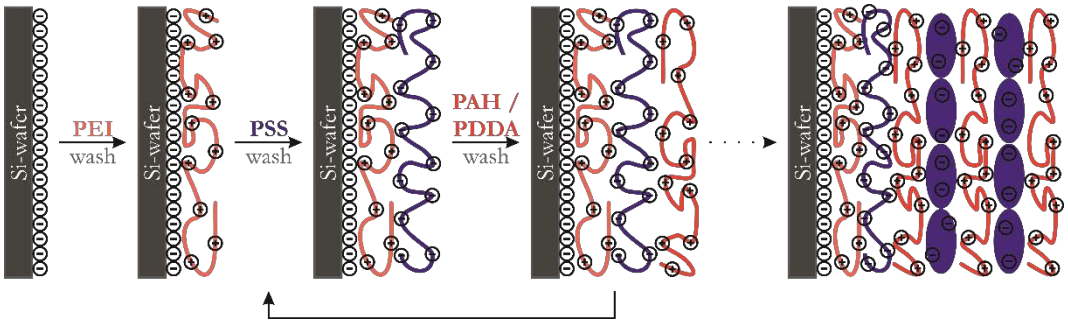

Fig. 1. Build-up of polyelectrolyte multilayers. The polyanion has been replaced by the negatively charged calmodulin.

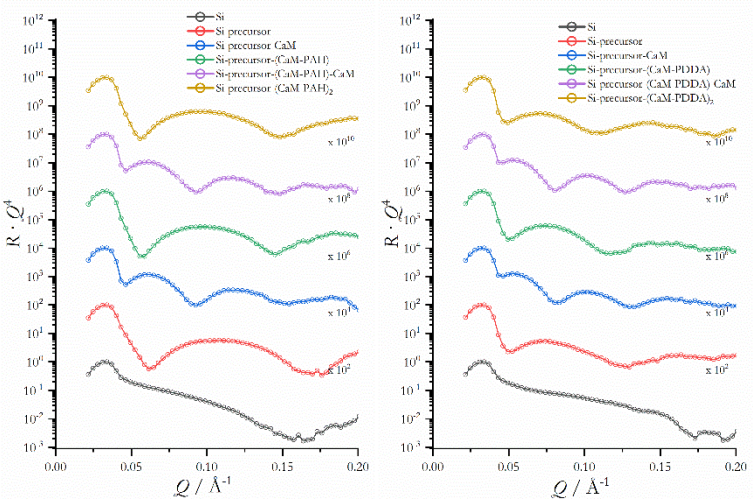

Fig. 2. X-ray reflectivity data showing the step-wise build-up of the PEMs with embedded calmodulin. Data were obtained in water-saturated air.

High pressure X-ray reflectivity data of PEMs were obtained at the Dortmund synchrotron DELTA at beamline BL9 using a home-built high pressure sample cell [3] (Fig. 3). All PEMs are characterized by strong electrostatic interactions, which are known to be weakened under

pressures up to 2000 bar [4]. Thus, when holo-CaM is embedded in a PEM, it can be expected that the interaction of the protein with the surrounding polyelectrolyte chains is weakened upon pressurization inducing a larger conformational freedom of the embedded holo-CaM protein molecules. We have also studied a holo-CaM-containing PEM in the presence of TFP, which is a strongly binding ligand of holo-CaM (Fig. 3). Upon binding TFP, holo-CaM, in aqueous solution, undergoes a conformational transition from a dumbbell-shaped to a globular conformation.

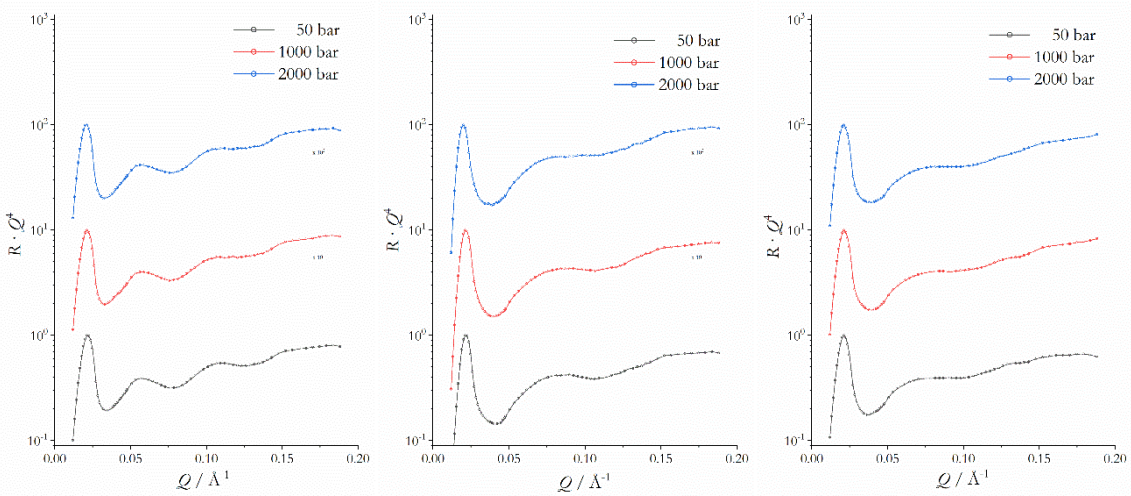

Fig. 3. Selected high pressure X-ray reflectivity data obtained at BL9 of the Delta synchrotron. A PEM without CaM (left), with embedded CaM (middle), and with embedded CaM in the presence of the ligand TFP (right) have been studied.

The data in Fig. 3 show Kiessig fringes that are consistent with approximate PEM thicknesses of 124 Å in the absence of holo-CaM, 97 Å when holo-CaM is embedded, and 98 Å when holo-CaM is embedded and the ligand TFP is present in the solution. However, overall, there are little pressure effects on the structure of the investigated samples. A slight flattening of the minima at about $Q = 0.12$ Å^{-1} can be observed as the pressure is increased that is likely related to an increased roughness of the multilayers. It might also point to a pressure-induced conformational change of the embedded protein molecules. A more detailed analysis yielding the electron density profiles is currently performed.

[1] G. Decher, Science, 277, 1997, 1232-1237

[2] S. Cinar, S. Möbitz, S. Al-Ayoubi, B.-K. Seidhofer, C. Czeslik, Langmuir, 33, 2017, 3982-3990

[3] F. J. Wirkert, M. Paulus, J. Nase, J. Möller, S. Kujawski, C. Sternemann, M. Tolan, J. Synchrotron Radiat., 21, 2014, 76-81

[4] B.B. Boonyaratanakornkit, C.B. Park, D.S. Clark, Biochim. Biophys. Acta 1595, 2002, 235–249

Crystal structure of poly(3-hexylthiophene):*N*-alkylated naphthalene diimide blends thin films

Dorota Chlebosz[1,2*], Adam Kiersnowski[1,3], Krzysztof Janus[1], Kinga Danielewicz[1], Markus Mezger[2]

[1]Faculty of Chemistry, Wroclaw University of Science and Technology, Wroclaw, Poland
[2]Max Planck Institute for Polymer Research, Mainz, Germany
[3]Leibniz Institute for Polymer Research, Dresden, Germany
[*]correspondence: dorota.chlebosz@pwr.edu.pl

The aim of this project was to investigate the crystal structure of thin films of poly(3-hexylthiophene):N-alkylated naphthalene diimide blends. Such blends are relevant for, e.g. applications in polymer-based solar cells[1] or transistors[2]. In our studies, we used poly(3-hexylthiophene) (P3HT) with the molar mass of 65 kg/mol (RR=95.7%; Ossila) and three different *N,N'*-substituted naphthalene diimides (NDI) with either n-butyl- (NDInC4), n-hexyl- (NDInC6) or n-octyl- (NDInC8) alkyl chains. The films were deposited using two different methods: spray coating (SC) or Laser-Assisted Zone Evaporation-Casting (LAZEC). As the LAZEC is not a commonly used technique, its basic principle is shown in Fig. 1.

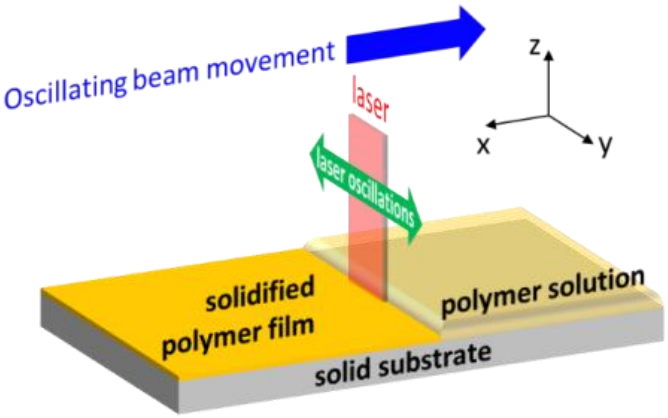

Figure 1. The principe of the LAZEC technique.

Results of our experiments indicated that crystallization of both P3HT and NDI is hindered in the blends. Sharp diffraction peaks visible in the GIWAXAS patterns of P3HT (Fig. 2m-o) and an exemplary NDI (NDInC6, Fig. 2a-c) suggest that both the pure P3HT and the pure NDI form crystalline layers. In the case of blends the intensities coherently scattered by crystalline domains of P3HT and NDInC6 are noticeably reduced, which, considering comparable film thicknesses of all the systems, indicates reduced crystallinity of the blend components in the films. Such an observation suggests that interactions between NDI and P3HT either in solution or during the solidification process lead to a decreased crystallinity of the components. An

intriguing question that remains open at this point, is the nature of these interactions. This problem will be further studied with the NMR technique.

A preliminary analysis of the orientation of P3HT crystals in the films indicates that the SC-deposited films reveal both so-called "edge-on" and "face-on" orientation, and the latter orientation seems dominating[3]. Such a conclusion can be drawn based on the distribution of intensity in the GIWAXS pattern shown in Fig. 2m. The highest intensity of 100 peaks is clearly visible at the equatorial line at q~0.38 $Å^{-1}$. There is, however, also a clearly increased intensity visible on the horizon, also at q~0.38 $Å^{-1.}$ Followed, the weak diffuse-like intensities at q~1.6 $Å^{-1}$ that can be associated with the 120/020 group of reflections[4] (they are often referred to as pi-stacking reflections) are visible at the horizontal and equatorial positions in Fig. 2m. Presence of the Debye-Scherrer ring at q~0.38 $Å^{-1}$, suggests that the P3HT film contains also a certain amount of the randomly oriented crystals. Upon addition of NDInC6, the relative intensities of reflections related to 100 series remain unchanged. However, surprisingly somewhat, the "pi-stacking reflections" disappear from the horizon (Fig. 2j) after adding the smallest amount of NDInC6 tested in the 5:1 blend. This may suggest disruption or loss of perfection of the "edge-on" oriented P3HT crystals caused by NDI molecules.

The orientational structure of films formed by the LAZEC technique is more complex. The LAZEC controls not only the orientation of crystals with respect to the substrate, but also with respect to the deposition direction (the x-axis in the Fig. 1). Based on the intensity and azimuthal distribution of the 100 peak recorded for the film of the pure P3HT with the x-axis oriented along (Fig. 2n) and perpendicular (Fig. 2o) to the beam one can conclude that P3HT crystallizes with chains extended along the deposition direction. That directional order of P3HT crystals seems lost after blending P3HT with NDInC6 (Figs. 2e,f,h,i,k,l) and is visibly less dependent on the orientation of the deposition direction against the X-ray beam. The orientation of crystals in the blends containing more than 75 wt. % of NDI in the films deposited by LAZEC was stronger than in the sprayed films. For the other blends, the deposition method has no effect on the orientation of the crystals in the film.

In the end, let us make a final remark on the data quality. Our GIWAXS experiments (13 keV; beam width ~1 mm; exposure time 600-900 s) were performed with the samples films in the ambient air. In the case of 100 nm films the quality of all patterns (i.e. the signal-to-background ratio) was satisfactory and enabled quantitative analysis. In the case of thinner films (~50 nm, deposited with LAZEC) the scattering from the samples was quite often in the range of the intensity from the background which made the data analysis more difficult.

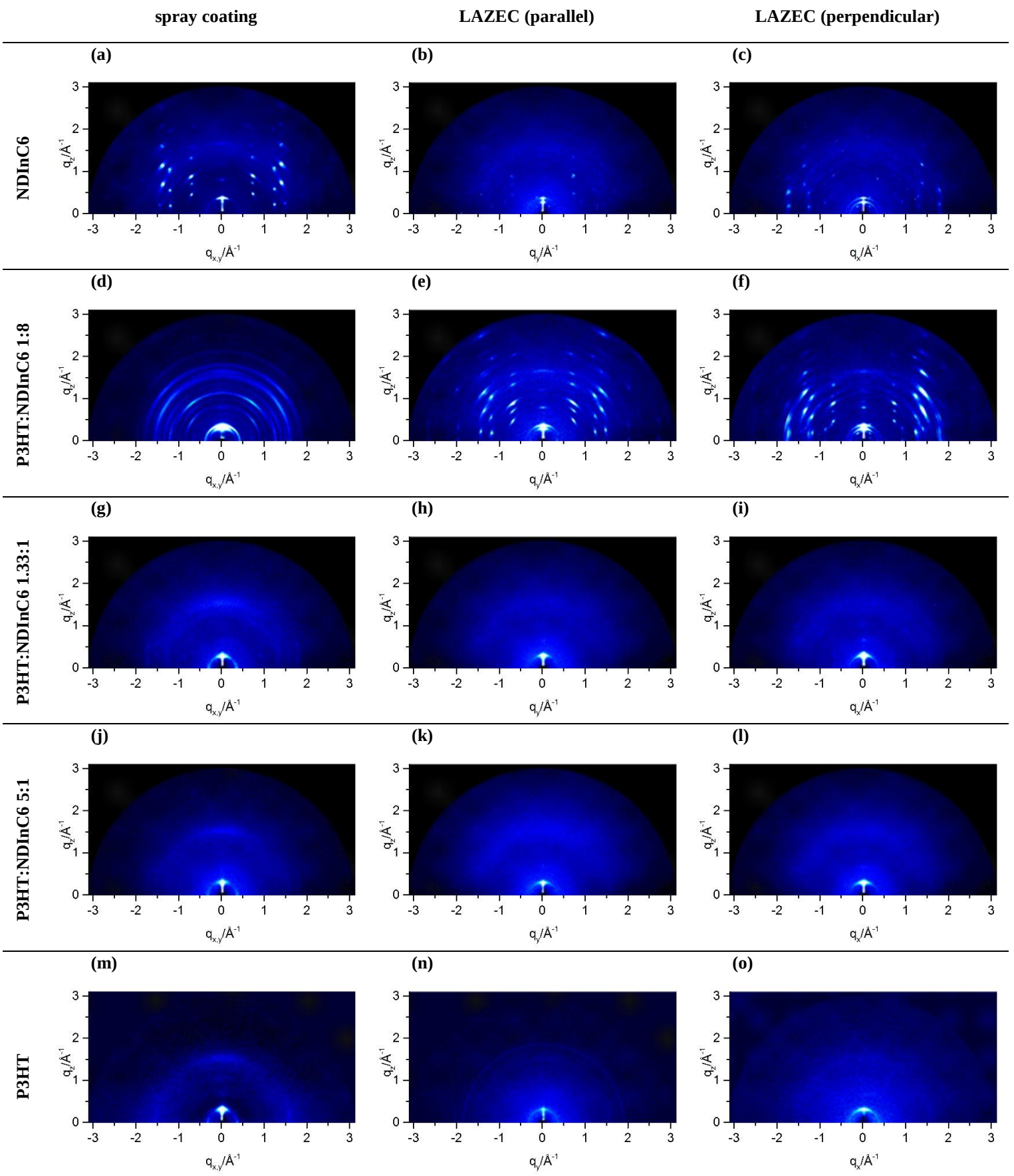

Figure 2. Exemplary GIWAXS patterns recorded for NDInC6, P3HT and their blend. The films were obtained by spray coating and Laser-Assisted Zone Evaporation-Casting (LAZEC). GIWAXS patterns of LAZEC films were recorded with the X-ray beam incident parallel and perpendicular to the deposition direction. The q_z scale is valid for the zero q_x or q_y.

Acknowledgement

The project was supported through the grants 2016/22/E/ST5/00472 (National Science Centre Poland) and 0402/0104/17 (Ministry of Science and Higher Education). The access to the BL9 beamline (11-13.07.2018) granted by a scientific council of DELTA synchrotron facility is gratefully acknowledged. The researchers involved in this project express their gratitude to Dr. Christian Sternemann and Dr. Michael Paulus for their help in the experiments.

References

1 Dai, S. X. *et al.* Perylene and naphthalene diimide polymers for all-polymer solar cells: a comparative study of chemical copolymerization and physical blend. *Polymer Chemistry* **6**, 5254-5263, doi:10.1039/c5py00665a (2015).

2 Janasz, L. *et al.* Ultrathin film heterojunctions by combining solution processing and sublimation for ambipolar organic field-effect transistors. *Journal of Materials Chemistry C* **6**, 7830-7838, doi:10.1039/C8TC01502C (2018).

3 Chlebosz, D., Janasz, Ł., Pisula, W. & Kiersnowski, A. Relationship between crystalline structure of poly(3-hexylthiophene) blends and properties of organic thin-film transistors – a brief review. *Polimery* **61**, 433-441, doi:10.14314/polimery.2016.433 (2016).

4 Dudenko, D. *et al.* A Strategy for Revealing the Packing in Semicrystalline π-Conjugated Polymers: Crystal Structure of Bulk Poly-3-hexyl-thiophene (P3HT). *Angewandte Chemie International Edition* **51**, 11068-11072, doi:10.1002/anie.201205075 (2012).

Impact of the osmolyte TMAO on the barotropic phase behavior of single- and three-component multilamellar lipid membranes

Magiliny Manisegeran, Mimi Gao, Roland Winter, Irena Kiesel
Physikalische Chemie 1, TU Dortmund

Biological cells use compatible osmolytes against various environmental stress factors. Generally, stress factors include low and high temperature, desiccation, shear, and osmotic pressure. Trimethylamine-*N*-oxide (TMAO) (fig. 1) is an osmolyte known also for its pronounced stabilizing effect on proteins against high hydrostatic pressure stress in deep sea fish. Besides the stabilization against pressure, it protects proteins also against denaturation at high temperatures or destabilizing agents such as urea.[1] Little is known about the effect of TMAO on other bimolecular systems, such as lipid membranes.[2,3] In this experiment, we have investigated the influence of TMAO on two lipid systems: a one-component phospholipid bilayer system (DMPC) and a heterogeneous three-component lipid system (DOPC:DPPC:cholesterol 1:2:1). The structure of the lipid membranes and their barotropic phase behavior have been studied applying high hydrostatic pressure small-angle X-ray scattering (SAXS) complementary to FTIR and fluorescence spectroscopy as well as calorimetry studies.

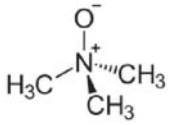

Fig. 1: TMAO Trimethylamine-*N*-oxide

The experiment was performed at beamline BL9 using a home built high hydrostatic pressure SAXS cell with diamond windows.[1,4] The energy used was 10 keV, which corresponds to a wavelength of λ = 0.12 nm. The sample detector distance was calibrated with silverbehenate. The scattering curves were recorded with an image plate detector MAR345 (d = 345 mm, 100 µm pixel size) and with an exposure time of 10 min. The pressure range covered was 1 to 3500 bar. The temperature was 40°C for DMPC and 60°C for the three component system. Multilamellar vesicles (MLVs) were prepared by hydration of a lipid film with 10 mM Tris buffer (pH 7.4) and five freeze-thaw cycles with a final lipid concentration of 100 mg/mL.

The results are shown in Figure 3 for (a) DMPC and (b) three component MLVs, both for 3 M TMAO and increasing hydrostatic pressure. The positions of the Bragg peaks are used to calculate the repetitive lamellar distance d (fig. 2). Comparable to *Sukenik et al*.[2], the repetitive lamellar distance decreases with increasing TMAO concentration. With increasing pressure, the phase transitions of DMPC bilayers occur from the liquid-like state L_α to the gel state $P_{\beta'}$ to the gel state $L_{\beta'}$.[5] The three-component system has a phase transition from l_d (liquid-disordered, cholesterol depleted) to a mixture of l_d and l_o (liquid ordered and cholesterol enriched).[6] The solid ordered (s_o) phase reported in literature was not observed. The phase transition pressure is slightly decreased with increasing TMAO concentration. Especially at high TMAO concentrations, several Bragg peaks appear, indicating formation of phase coexistence regions.

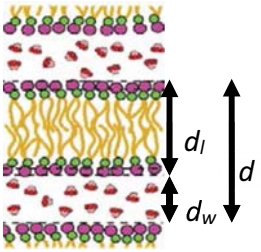

Fig. 2: Mulilamellar lipid-bilayer with TMAO (red): d_w water layer thickness, d_l lipid bilayer thickness, d repetitive lamellar distance ($d = d_w + d_l$).

In conclusion, corroborated by results from calorimetry, FTIR and fluorescence spectroscopy (not shown here), we can conclude that TMAO influences the repetitive lamellar distance of lipid bilayers, probably due to dehydration of the interlamellar water layer d_w. The barotropic phase

behavior is slightly shifted owing to a stabilizing effect of the gel state imposed by TMAO. The $P_{\beta'}$ state seems to be unfavorable in the presence of TMAO. Phase coexistence regions appear at high TMAO concentrations.

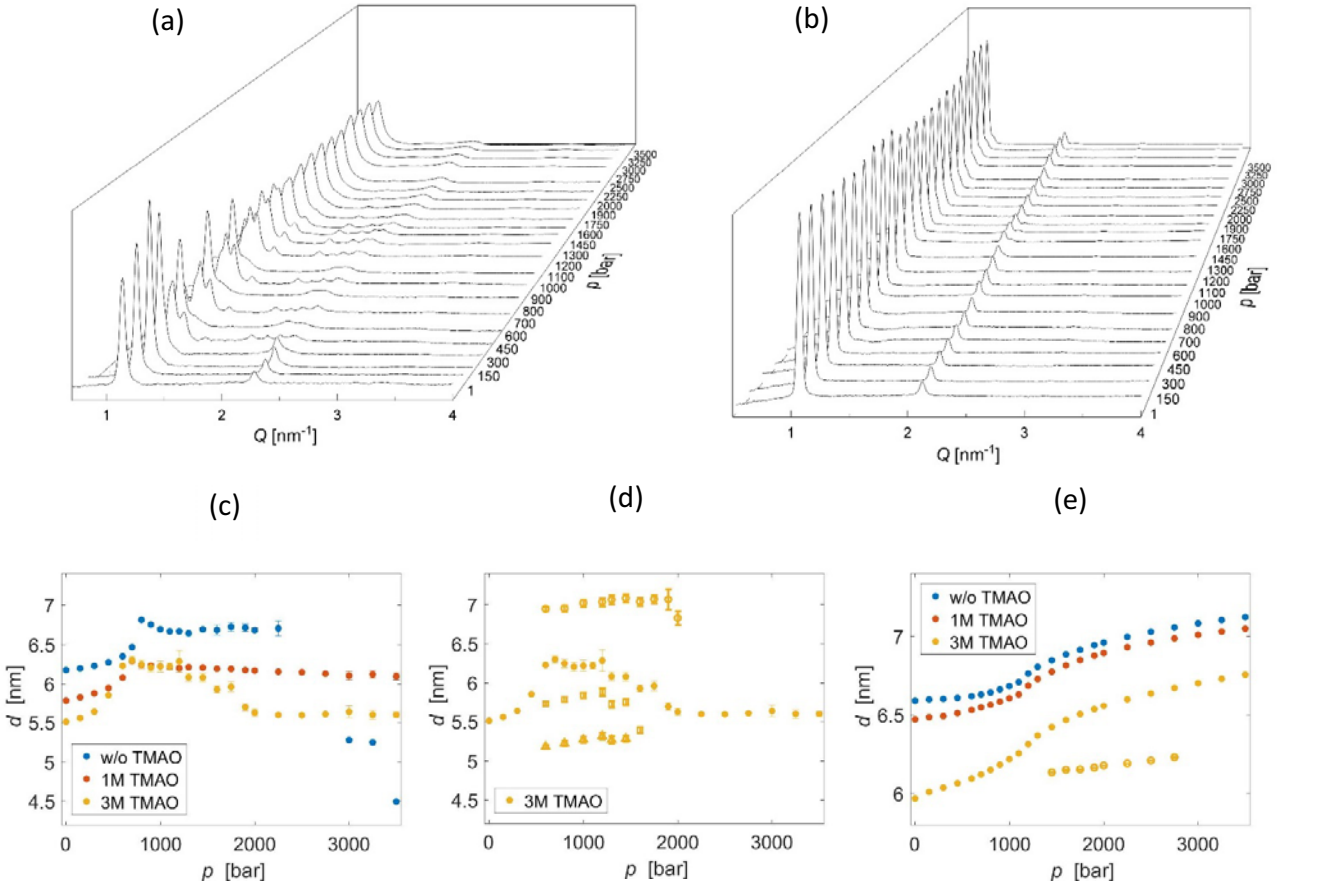

Fig. 3: Representative SAXS curves of (a) DMPC and (b) DOPC:DPPC:cholesterol 1:2:1 in the presence of 3 M TMAO as a function of hydrostatic pressure. The Bragg peak positions are used to calculate the repetitive lamellar distance *d*.
(c) The calculated distance *d* of the main peak for DMPC with no TMAO (blue), 1 M TMAO (red) and 3 M TMAO (yellow). Up to four Bragg peaks appear in the presence of high TMAO concentrations in the case of (a) DMPC MLVs, the corresponding lamellar distances are shown in (d) for DMPC with 3 M TMAO. The observed *d*-spacings for DOPC:DPPC:cholesterol MLVs with increasing hydrostatic pressure and for three different TMAO concentrations are shown in (e). A second Bragg peak appears in the presence of 3 M TMAO, indicated by unfilled yellow circles. Error bars are calculated by the goodness of determining the peak positions.

References

[1] C. Krywka, C. Sternemann, M. Paulus, M. Tolan, C. Royer, R. Winter, *ChemPhysChem* **2008**, *9*, 2809–2815.
[2] S. Sukenik, S. Dunsky, A. Barnoy, I. Shumilin, D. Harries, *Phys. Chem. Chem. Phys.* **2017**, *19*, 29862–29871.
[3] Q. D. Pham, A. Wolde-Kidan, A. Gupta, A. Schlaich, E. Schneck, R. R. Netz, E. Sparr, *J. Phys. Chem. B* **2018**, DOI 10.1021/acs.jpcb.8b02159.
[4] C. Krywka, M. Paulus, C. Sternemann, M. Volmer, A. Remhof, G. Nowak, A. Nefedov, B. Pöter, M. Spiegel, M. Tolan, *J. Synchrotron Radiat.* **2005**, *13*, 8–13.
[5] J. Eisenblätter, R. Winter, *Biophys. J.* **2006**, *90*, 956–966.
[6] C. Jeworrek, M. Pühse, R. Winter, *Langmuir* **2008**, *24*, 11851–11859.

Acknowledgements:
We would like to thank DELTA for the awarded beamtime. Furthermore, we are thankful for support at beamline BL9 by M. Paulus and Ch. Sternemann and with the high pressure setup by G. Surmeier. Special thanks to S. Bornmann, M. Herzog, M. Jaworek and J.-M. Knop for the experimental support during the experiment. IK thanks the Cluster of Excellence RESOLV (EXC 1069) for financial support.

Comparing destabilizing factors on lysozyme adsorption on solid/liquid interfaces

Justin Sonneck, Göran Surmeier, Michael Paulus, Metin Tolan and Julia Nase

Fakultät Physik / DELTA, Technische Universität Dortmund
D-44221 Dortmund, Germany

The adsorption of proteins plays a major role in a vast number of systems in contact with aqueous natural environments. For example, protein adsorption is an important initial step for the formation of biofilms at interfaces in contact with aqueous solutions, decreasing thus the lifetime of medical equipment. Protein adsorption depends on a large number of environmental parameters like pH, temperature, van der Waals interaction with the surface and also on the hydrophobic or hydrophilic character of the surface. Because of this high complexity, the field is continuously attracting the interest of physicists, chemists, biologists and engineers alike. It is of particular interest to understand the interplay between protein denaturation and the formation of an adsorption layer.

During adsorption to hydrophobic surfaces, proteins lose their native conformation and partially unfold at the interface due to strong hydrophobic interactions. Additionally, the application of pressure stress (HHP) to proteins can destabilize them. Destabilizing cosolvents like urea can drastically lower the adsorption of proteins at water-air interfaces. In this study, we aimed at investigating the interplay of different destabilizing factors, urea and HHP, on the well-known model protein lysozyme. We studied the adsorption of lysozyme from aqueous (urea) solutions to the hydrophilic and hydrophobic solid/liquid interface with X-ray reflectivity (XRR) while pressurizing the system to 4000 bar. Lysozyme solutions were prepared in a concentration of 0.1 mg/mL. Urea solutions were prepared in a concentration of 1 M/L. The aqueous medium was pressure-stable BisTris buffer (20 mMol) at a pH of 7.1. Experiments were performed at BL9 of DELTA at a beam energy of 27 keV.

In general, we must state the data quality was intermediate due to unknown problems with the sample preparation. Thus, we show in the following reflectivity data without fit and discuss merely tendencies in the data set.

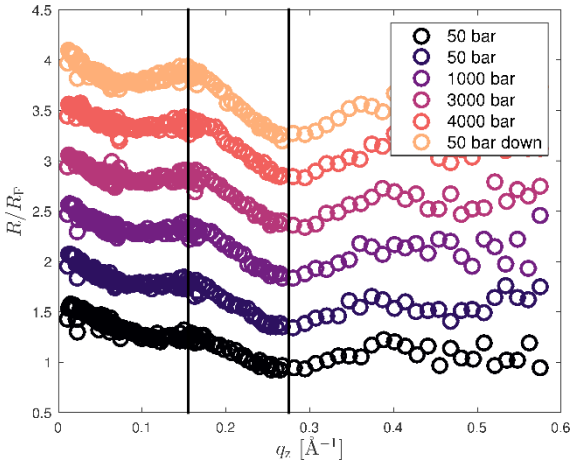

Figure 1 Electron density profiles and XRR data of the interface between aqueous Lysozyme solutions and a Si/SiO₂ wafer. XRR data are shifted vertically for better visibility [1].

Figure 1 shows the results for experiments performed in pure Lysozyme solution in contact with hydrophilic Si/SiO_2 wafers. Visible from the oscillations in the reflectivity curve, we detected an adsorption layer at the silicon oxide surface. Increasing the pressure, the layer thickness remained essentially constant for two different samples, which is visible from the solid vertical lines in Figure 1. They indicate that the positions of the maxima/minima do not move.

However, comparing the upper and the lower curve, measured at 50 bar and at 50 bar after the pressure increase, it becomes clear that the system experiences an irreversible effect. This phenomenon remains to be further explored and a more profound data analysis is currently ongoing.

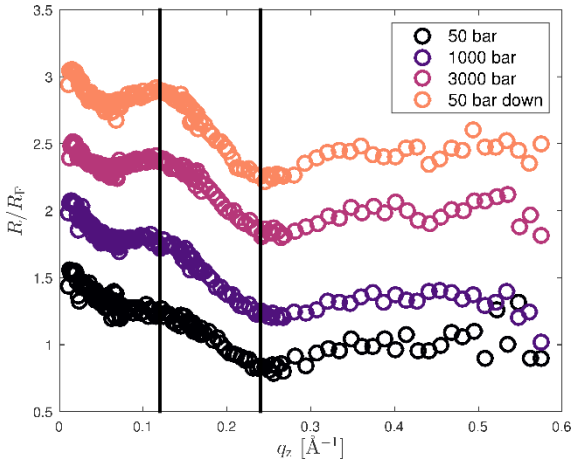

Figure 2 Electron density profiles and XRR data of the interface between aqueous Lysozyme solutions with 1 M/L of urea and a Si/SiO_2 wafer. XRR data are shifted vertically for better visibility [1].

Figure 2 shows corresponding results for a system in a 1 M/L urea solution. The smaller q_z – values of the positions of maximum and minimum indicate that the layer thickness is higher than in the experiments without urea. This might hint to an additional adsorption of denatured protein.

We performed similar experiments at hydrophobic interfaces (data not shown). In absence of urea, the average layer thickness was below the dimensions of the native protein, indicating thus the expected denaturing effect of hydrophobic interfaces. The data of hydrophobic interfaces in urea solutions were unfortunately too noisy to yield reliable results, but they hint to an increased layer thickness at low pressure as compared to the case without urea. This effect remains to be further explored.

Acknowledgement: We thank the DELTA team for providing synchrotron radiation and the DFG-FOR1979 for funding.

[1] J. Sonneck, Einfluss von Hochdruck und Urea auf die Adsorption von Lysozym an Grenzflächen, Bachelorarbeit, TU Dortmund, 2018.

Structural properties of conjugated polymers and blends on a stretchable substrates

M.Y.Aliouat[a], S.Escoubas[a], O, Thomas[a] and S.Grigorian[b]

[a] Aix Marseille Univ, Univ Toulon, CNRS, IM2NP, Campus de St-Jérôme, 13397, Marseille, France

[b] Institute of Physics, University of Siegen, Walter-Flex-Strasse 3, D-57068 Siegen, Germany

With the development of flexible/stretchable organic electronics such as OLEDs [1], OFETs [2] and OPV [3], π-conjugated semiconducting polymers and oligomers received more and more attention because they are the main elements who compose these devices. For stretchable OPV applications, PffBT4T-2OD (PCE11) is a promising polymer with a high power conversion efficiency (PCE = 11%) and good crystallinity [4] [5]. In the current work we have studied the evolution structure of PCE11 and PCE11: PCBM blend (with 3% of DIO additive) under tensile test. After improving the wettability, polymer inks were spin coated on glass substrates (as a reference) and on stretchable PDMS substrates. For this study, in situ grazing incidence X-ray diffraction (GIXRD) at the BL9 at Delta synchrotron are carried out in order to probe the structural properties of polymer films, in other words to know how polymer chains are ordered and oriented and how they evolve under stretching. We used an image plate 2D detector (MAR3450) to see the diffracted peaks both along out-of-plane (q_z) and in-plane (q_{xy}).

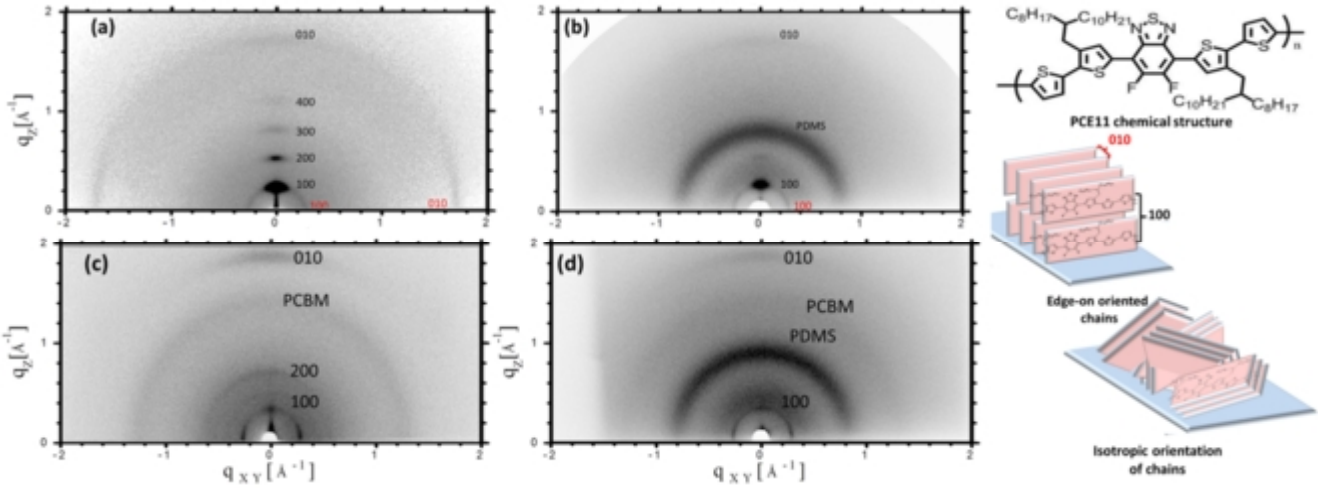

Figure 1. 2D GIXD pattern of: PCE11 spin coated on (a) Glass (b) PDMS, PCE11: PCBM spin coated on (c) Glass (d) PDMS

Figure 1.a and b shows the 2D GIXD patterns of PCE11 spin coated on glass and PDMS (respectively). As we can see both of them shows most of the scattering intensity along q_z . The pattern in figure 1.a reveals a highly edge-on oriented PCE11 film coated on glass, with

the strongest 100 peak until the fourth order along (q_z). And the 100 peak along both the out-of-plane (q_z) and the in-plane (q_{xy}). On the other hand, the pattern of PCE11 coated on PDMS (figure 1.b) reveals a less edge-on oriented film, with the 100 peak until the second order along q_z and a weak peak along (q_x), with contribution of the PDMS amorphous ring.
Figure 1.b and c shows the 2D GIXD patterns of the blend PCE11:PCBM spin coated on glass and PDMS (respectively), we can see clearly the diffracted ring of the 100 peak for both of them .The pattern in figure 1.c reveals an isotropic orientation of polymer chains whether for the PCE11 or PCBM peaks. On the other hand, the pattern of PCE11: PCBM coated on PDMS (figure 1.d) reveals almost the same isotropic orientation with less intense peaks, and the contribution of PDMS ring.

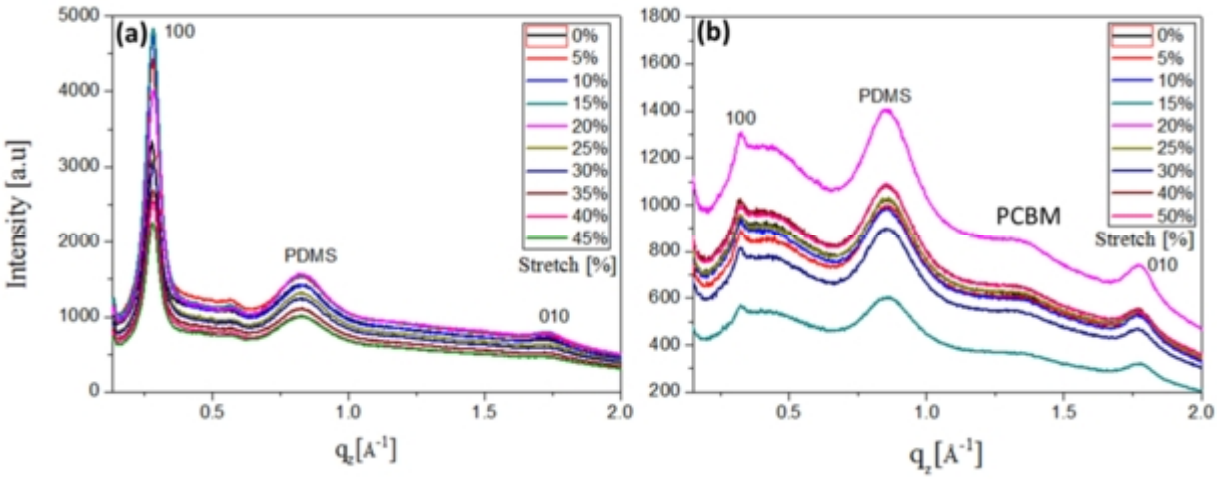

Figure 2. Out-of-plane profiles of (a) PCE11 (b) PCE11:PCBM spin coated on PDMS, under stretching up to 50 %.

Figure 2 shows the out-of-plane profiles of PCE11 (a) and PCE11: PCBM (b) under stretching with a step of 5 %, respectively. To better understand the mechanical behaviour, we plotted the deformation (ε_z) of polymer chains for the most remarkable peaks along q_z, in order to know how the deformation of polymer chains change at different stretching values. $\varepsilon_z(\%) = \frac{d-d_0}{d_0} \times 100$. These results were correlated with optical microscopic observations by following a propagation of the cracks. We also noticed a very weak mechanical charge transfer from support to polymer layer with shows that the applied strain strongly dissipated in the amorphous regions of the polymer.

[1] Akira Sugimoto, Hideo Ochi, Soh Fujimura, Ayako Yoshida, Toshiyuki Miyadera, and Masami Tsuchida. IEEE Journal of Selected Topics in Quantum Electronics, **10**, 107-114, (2004)
[2] Tianlei Sun, Joshua I. Scott, Ming Wang, Regis Joseph Kline, Guillermo C. Bazan, and Brendan T. O'Connor, Adv. Electron. Mater, **3**, 1600388, (2017)
[3] Darren J. Lipomi , Benjamin C.-K. Tee , Michael Vosgueritchian , and Zhenan Bao, Adv. Mater, **23**, 1771–1775,(2011)
[4] Jiao Zhao, Suling Zhao, Zheng Xu,Bo Qiao,Di Huang,Ling Zhao,Yang Li, Youqin Zhu,and Peng Wang, ACS Appl. Mater. Interfaces, **8**, 18231−18237, (2016)
[5] Wei Ma , Guofang Yang , Kui Jiang , Joshua H. Carpenter , Yang Wu , Xiangyi Meng ,Terry McAfee , Jingbo Zhao , Chenhui Zhu , Cheng Wang , Harald Ade , and He Yan. Adv. Energy Mater, **5**, 1501400,(2015)s

X-ray reflectivity study on metal cation binding to phospholipid bilayers

[1+]Dogan, Susanne; [2]Kulig, Waldemar; [1]Paulus, Michael; [1]Sternemann, Christian; [1]Moron, Mike; [2]Moron, Marc; [1]Tolan, Metin; [2]Huotari, Simo

[1]Technische Universität Dortmund, Fakultät Physik / DELTA, 44221 Dortmund, Germany
[2]Department of Physics, University of Helsinki, Finland
[+]susanne.dogan@tu-dortmund.de

The chemical and physical properties of biological membranes is crucial for the understand membrane functions. The main biological role of bilayers is to provide a barrier that divides electrolytic solutions into different compartments. Therefore, the investigation of electrolytic solutions on membranes is of great importance and has generated wide research [1]. However, ion binding affects the stability of proteins and their process of binding to membranes [2], and it is also mainly responsible for lipid vesicle fusion [3, 4].

The physical origin for diverse effects of ions on lipid bilayers is not well understood. Despite the vast amount of experimental and theoretical studies on the interaction with cations and phospholipid bilayers, the role of the interaction and the quantitative affinity as well as the binding locations are mostly uncharted and highly controversial.

To shine light on the binding properties, we combine state-of-the-art molecular dynamics (MD) simulations [5; 6] and experimental X-ray reflectivity (XRR) data which were obtained at BL9 at DELTA [7]. The XRR technique is widely used for interface characterization with angstrom resolution. It provides information on layer thickness, roughness, and electron density.

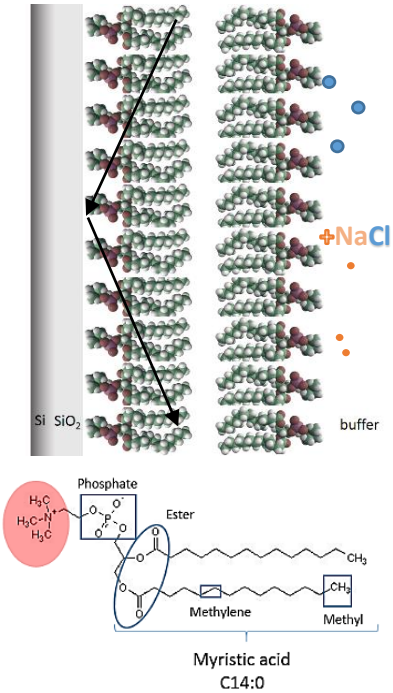

Fig. 1: Measured model system (top): Si, SiO_2, DMPC bilayer. Addition of salt solution (NaCl) and dissolution in anions and cations. DMPC structure (bottom).

We measured the XRR profiles of highly oriented bilayers of 1,2-dimyristoyl-sn-glycero-3-phosphocholine (DMPC) lipid supported on a Si single crystal wafer by spin-coating [8], the wafers were immersed in aqueous solution of relevant salts, which introduces the binding of cations. Figure 1 shows the measured model system. XRR allows us to measure the electron density profile along the layer normal to determine the binding location of the cations within the layer. To maximise the cation electron density contrast with respect to the lipid, we studied the binding of the relatively high-Z cations Na^+ (monovalent, $[c]_{eukaryotic\ cell}$: 150 mM) and Ca^{2+} (divalent, $[c]_{eukaryotic\ cell}$: 15 mM). Sodium in the form of the Na^+ cation is one of the most important extracellular electrolytes in terms of quantity (electrolyte balance). Calcium is an important intercellular second messenger [9].

We prepared the samples on site and use NaCl and $CaCl_2$, which are highly soluble in water, as providers of the cations. The concentration was varied between 0 M and 1 M. The binding depends strongly on the temperature. To mimic a realistic biological system we heated the sample to 37°C (L_α phase of DMPC). Therefore, we applied a custom-made PTFE-XRR cell - that can be temperature controlled up to 80°C with a temperature stability of 0.2°C.

The XRR patterns were detected with the PILATUS 100k detector as a function of the incident angle up to 1.2° and angular resolution of 0.002° at a photon energy of 27 keV. A reflectivity curve from the water-solid-supported DMPC bilayer systems without salt was recorded as a reference. In the following the salt concentration in the sample

system was adjusted by adding consecutively salt solution from a stock solution into the cell without affecting the wafer. We reached a resolution of ~1 Å in the electron density profile map, precise enough to detect the binding location of the cations within the lipid.

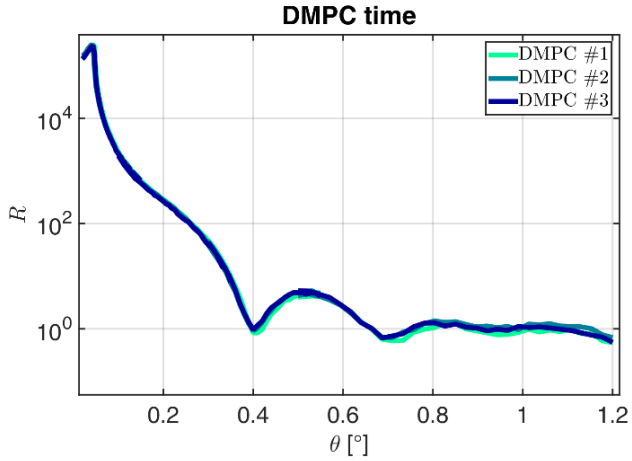

Fig. 2: Fig. 2: X-ray reflectivities of solid-supported DMPC bilayer on Si/SiO₂ (raw data, unprocessed).

First, we tested the temporal stability and thickness of the solid-supported DMPC bilayer. The results show that there are no significant changes and the thickness is 47 ±1 Å (profiles not shown, first analysis). The system is stable at the chosen experimental conditions over a longer period of time of 4 hours. The reflectivity curves with their characteristic oscillations are shown in fig. 2. Figure 3 presents the raw XRR measurements of solid-supported DMPC bilayer with increasing salt concentrations (left: NaCl, right: $CaCl_2$). As can be seen, there are changes in the reflectivity curves. Above a NaCl concentration of 0.0125 M the oscillations shifted towards higher angles. This means a reduction of the bilayer thickness. Sodium may cause this change by complexation of the phosphate region of the lipids. An interaction between Na and phosphate moieties of lipids were shown in [10]. In contrast to that, $CaCl_2$ acts as a light membrane stabiliser at lower concentrations and leads to a shift of the reflectivity curve at the highest concentration at 0.5 M to smaller angles. The assumption that Ca^{2+} adsorb at the DMPC membrane surface over 0.5 M is appropriate at the highest concentration. Moreover, a dripping of ions into the bilayer structure at this concentration can be probable.

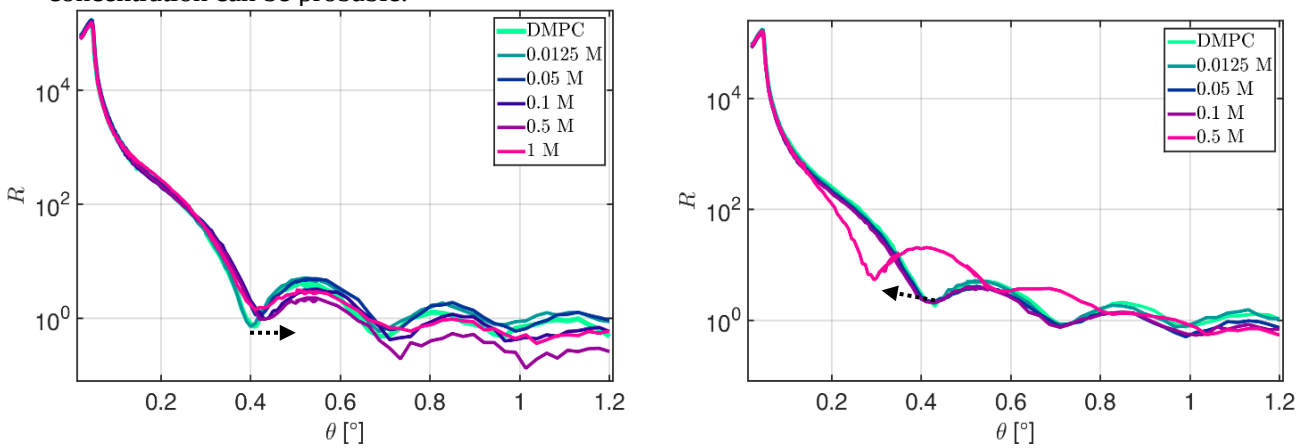

Fig. 3: X-ray reflectivities of solid-supported DMPC bilayer with increasing NaCl (left) and $CaCl_2$ concentration (right).

The exact analysis and final interpretation of the electron density profiles are in progress. Furthermore, we used all-atom MD simulations to study the ion binding to DMPC bilayer computationally and the electron density profiles from XRR can be directly compared with similar profiles extracted from MD simulations for each system component (e.g., ions and lipids).

References

[1] G. Cevc, Membrane electrostatics, Biochim. Biophys. Acta, 1031 (1990), pp. 311-382.
[2] H. Binder et al., The effect of metal cations on the phase behavior and hydration characteristics of phospholipid membranes, Chem. Phys. Lipids, 115 (2002), pp. 39-61.
[3] S. Ohki, et al., Phospholipid vesicle aggregation: effect of monovalent and divalent ions, Biochemistry, 21 (1982), pp. 2127-2133
[4] S. Ohki et al., Monovalent cation-induced phospholipid vesicle aggregation: effect of ion binding, Biochemistry, 23 (1984), pp. 6126-6132.
[5] Hub, J. S.et al., Short-range order and collective dynamics of DMPC bilayers: a comparison between molecular dynamics simulations, x-ray, and neutron scattering experiments. Biophysical Journal, 93(9), (2017), 3156-3168.
[6] W. Kulig et al., private communication
[7]Paulus, M. et al., An access to buried interfaces: the X-ray reflectivity set-up of BL9 at DELTA. Journal of synchrotron radiation, 15(6), (2008) 600-605.
[8] U. Mennicke et al., Preparation of Solid-Supported Lipid Bilayers by Spin-Coating, Langmuir, (2002), pp. 8172–8177.
[9] Berg, J. M. et al., Biochemistry. WH Freeman and Company (2017), 5, 306-307.
[10] Garcia-Manyes et al., Effect of ion-binding and chemical phospholipid structure on the nanomechanics of lipid bilayers studied by force spectroscopy. Biophysical journal, 89(3), (2005), 1812-1826.

Acknowledgments

We want to thank the DELTA machine group for providing synchrotron radiation.

Role of alkyl substituents on the microstructure and charge carrier transport in thin organic semiconductor films

Hanna Makowska[1], Michal Borkowski[1], Izabela Krygier[1], Witold Waliszewski[1], Tomasz Marszalek[1,2,*] and Wojciech Pisula[1,2,*]

[1] Department of Molecular Physics, Faculty of Chemistry Lodz University of Technology, Zeromskiego 116, 90-924 Lodz (Poland)

[2] Max Planck Institute for Polymer Research, Ackermannweg 10, 55128 Mainz, Germany

* Email: marszalek @mpip-mainz.mpg.de, pisula@mpip-mainz.mpg.de

Low molecular weight organic molecules offer some advantages as compared to their high molecular (polymeric) counterparts: i) they can be more easily purified and processed into technologically useful forms and ii) they show no dispersion of their molecular mass, thus they more easily form ordered supramolecular structures that are crucial for electrical transport properties. As a result, they can serve as active layers in organic field-effect transistors (OFETs) exhibiting high charge carrier mobilities.[1] Among the variety of low molecular weight semiconductors, heteroacenes deserve a special interest as candidates for application in OFETs.[2]

During our beam time at the BL9 of the DELTA electron storage ring in Dortmund in 2017-2018 we performed investigations on the influence of the attached substituents in heteroacene structures on the charge carrier mobility. The obtained results have been published as a two publications: a[4]) ACS Omega 2018, 3, 6513 – 6522, b[5]) Organic Electronics - DOI: 10.1016/j.orgel.2018.11.004.

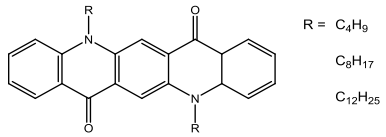

Scheme 1. Chemical structure of dialkyl substituted quinacridones.

We would like to put you attention on the second project (*described in Organic Electronics[5], dedicated to molecules presented in Scheme 1*) in which some contradiction to the current literature[3] has been observed. Earlier reports indicated that dialkyl derivatives of quinacridone showed no field-effect response in the transistors configuration. It was suggested that, in the case of long alkyl chains (longer than C4), highly disordered structures are obtained which significantly reduce the charge carrier transport. Based on the obtained results during our beam-time at the Delta synchrotron, it was found that **QA-C4** forms a hexagonal organization of columnar structures a_{hex} = 2.35 nm as derived from the small-angle reflections (Fig. 1a), which is in agreement with current literature. The packing of the molecules in the stacks is poor as evidenced from the low intensity in-plane π-stacking reflection at q_{xy} = 1.73 $Å^{-1}$ (π-stacking distance of 0.37 nm). However. In comparison to **QA-C4**, the structural order is increased in films of **QA-C8** and **QA-C12** whose diffraction patterns exhibit distinct reflections (Fig. 1b,c). The diffractograms of both films show an identical molecular order and organization. The d-spacing of the out-of-plane reflection increases from 1.38 nm for **QA-C8** to 1.69 nm for **QA-C12** manifesting the increase of the substituent length. A similar π-stacking distance of 0.36 nm is found for **QA-C12** as for the other two compounds.

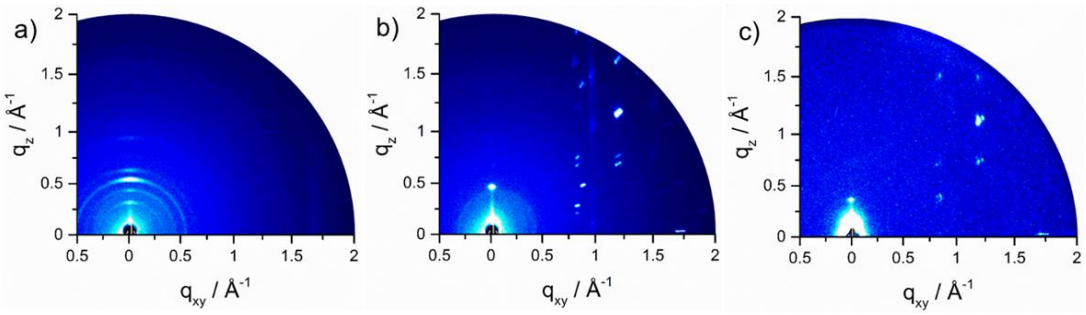

Figure 1. GIWAXS patterns of films of a) **QA-C4**, b) **QA-C8**, and c) **QA-C12**. The compounds are deposited on substrate at 120 °C.

Based on the obtained results it can be concluded that high mobility might be obtained for the same molecules with long alkyl chains when the deposition method is fully optimized. Our results experimentally proved these claims for two types of low molecular weight semiconductor (**QA-C8** and **QA-C12**).

In parallel to the investigation for the low molecular weight semiconductor, role of the heteroatoms in donor-acceptor polymer has been additionally investigated. Our studies indicated that naphthalene diimide – benzothiadiazole copolymers with "H" and "F" atoms have a similar organization in thin films but their electrical properties have been modified.[6]

Acknowledgement

This work was partially prepared as part of the „*Self-standing, flexible and solution processable organic field effect transistors for complementary inverter applications*" project that is carried out within the First Team programme of the Foundation for Polish Science co-financed by the European Union under the European Regional Development Fund (*First TEAM/2017-3/26*). I.K. and W.P. acknowledge the National Science Centre, Poland, through the grant UMO-2015/18/E/ST3/00322. The researchers involved in these projects express their gratitude to Dr. Christian Sternemann and Dr. Michael Paulus for their help in the experiments.

References

1. a) L. Yu, X. Li, J. Smith, S. Tierney, R. Sweeney, B. K. C. Kjellander, G. H. Gelinck, T. D. Anthopoulos, N. Stingelin, J. Mater. Chem. 22 (2012) 9458; b) Y. Yuan, G. Giri, A. L. Ayzner, A. P. Zoombelt, S. C. B. Mannsfeld, J. Chen, D. Nordlund, M. F. Toney, J. Huang, Zhenan Bao, Nat. Commun. 5 (2014) 3005; c) H. Jeong, S. Han, S. Baek, S. H. Kim, H. S. Lee, ACS Appl. Mater. Interfaces 8 (2016) 24753.
2. a) J. KIm, AR. Han, J.H. Seo, J.H. Oh, C. Yang, Chem. Mater. 24 (2012) 3464; b) T. Mori, T. Nishimura, T. Yamamoto, I. Doi, E. Miyazaki, I. Osaka, K. Takimiya, J. Am. Chem. Soc. 135 (2013) 13900; c) U.H.F. Bunz, Acc. Chem. Res. 48 (2015) 1676;.,
3. Z.-X. Xu, H.-F. Xiang, V. A. L. Roy, S. S.-Y. Chui, Y. Wang, P. T. Lai, C.-M. Che, Appl. Phys. Lett. 95 (2009) 123305
4. **T. Marszalek**, **I. Krygier**, A. Pron, Z. Wrobel, P. M. W. Blom, I. Kulszewicz-Bajer, and **W. Pisula**, Organic Electronics, DOI: 10.1016/j.orgel.2018.11.004
5. A. Keerthi, **W. Waliszewski**, C. An, A. Jaber, D. Xia, K. Müllen, **W. Pisula**, **T. Marszalek** and M. Baumgarten, „ Molecular Ordering of Dithieno[2,3-d;2',3'-d]benzo[2,1-b:3,4-b']dithiophenes for Field-Effect Transistors" *ACS Omega*, *3* (2018) 6513
6. C. An, **H. Makowska**, B. Hu, R. Duan, **W. Pisula**, **T. Marszalek** and M. Baumgarten, *RSC Adv*. 8 (2018) 16464 – 16469

In-situ monitoring of reversible guest-uptake in ultrathin films of Hofmann-type coordination polymers

Víctor Rubio-Giménez,[1] Sergio Tatay,[1] Carlos Bartual-Murgui,[1] Jose A. Real,[1] Christian Sternemann[2] and Carlos Martí-Gastaldo[1]

[1]Instituto de Ciencia Molecular, Universitat de València, Catedrático José Beltrán 2, 46980 Paterna, Spain.
[2]Fakultät Physik / DELTA, Technische Universität Dortmund, Maria-Goeppert-Mayer-Str. 2, D-44227 Dortmund, Germany.

The nanostructuration of coordination polymers (CPs) can substantially modify their electronic properties and their structural response to guests due to surface/interface effects.[1] Thanks to the advanced ultrathin film fabrication methodologies,[2] we can analyse these changes as a function of structure, composition, thickness and crystallinity. The structural changes need to be studied through equally powerful characterization techniques like synchrotron X-ray diffraction (XRD) due to the low electronic density and nanometric thickness of CP ultrathin films. Hofmann-type coordination polymers (HCPs) are a class of metal-organic materials composed by layers of alternating octahedral Fe^{II} and square planar Pt^{II} centers connected via cyanide groups.[3, 4] The Fe^{II} ions also are coordinated to two additional pillaring ligands which stack the metal-cyanide sheets to form a 2D or 3D structure depending on their denticity. The layers of a 3D HCP are covalently bonded, whilst 2D HCPs stack thanks to π-π interactions and form an interdigitated structure with a general formula $[Fe(L)_2\{Pt(CN)_4\}]$. In contrast to their 3D counterparts, 2D CPs are not intrinsically porous in the bulk form. However it was recently demonstrated for the HCP $[Fe(pyridine)_2\{Pt(CN)_4\}]$, that only ultrathin films of less than 20 nm are capable of adsorbing solvent molecules thanks to a gate-opening phenomenon.[5] The bulk form has excessively large crystalline domains and is not flexible enough to present this dynamic guest adsorption. Based on this first report we prepared ultrathin films of a similar 2D HCP by changing the axial pyridine for an extended pillaring ligand: isoquinoline, aiming at enhancing the adsorption effect. We investigated this effect at BL9 using surface XRD with the Pilatus100K detector at a wavelength of 0.82 Å (15 keV). Ultrathin film samples were placed into a closed cell and out-of-plane diffraction was measured under a continuous of different solvent-He mixtures as shown in Figure 1.

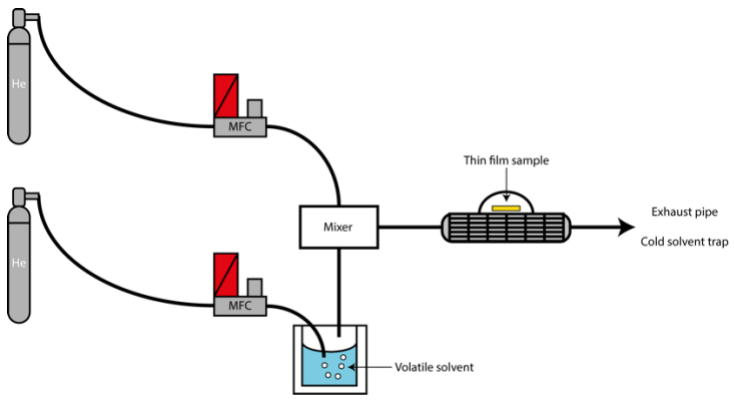

Figure 1. Scheme of the experimental set-up for the in-situ XRD measurements of $[Fe(isoquinoline)_2\{Pt(CN)_4\}]$ thin films under volatile solvents. This features two He currents, the dilution gas (top) and the carrier gas (bottom). The latter flows through a bubbler that contains the volatile solvent, yielding a solvent-saturated He mixture, which will later mix with the carrier gas and then pass through the sample in the doomed stage.

Figure 2 shows the experiment results for a maximum relative pressure ($P/P_0 = 1$) of solvent vapours. The out-of-plane lattice expansion was probed by measuring the displacement of the (001) peak for [Fe(isoquinoline)$_2${Pt(CN)$_4$}]. Unfortunately, the observed effect was considerably lower than what was reported in the original publication for [Fe(pyridine)$_2${Pt(CN)$_4$}]. Our films showed a maximum peak displacement of just 0.3% while the shift of the previously reported system was of 1.5%. In any case the effect seems to be slightly smaller for the bulkier solvent molecules.

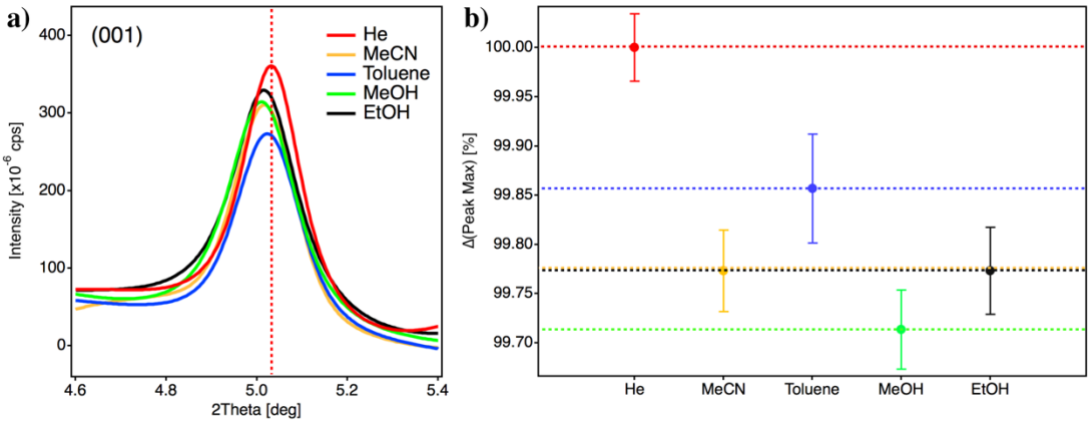

Figure 2. a) Out-of-plane XRD profile around the (001) peak of a [Fe(isoquinoline)$_2${Pt(CN)$_4$}] ultrathin film (20 nm) under different He-solvent atmospheres (He stands for a pure He without solvent). b) Peak displacement percentages for the different He-solvent mixtures.

---

[1] S. Sakaida, T. Haraguchi, K. Otsubo, O. Sakata, A. Fujiwara, H. Kitagawa, *Inorg. Chem.* **2017**, *56*, 7606-7609.
[2] F.-X. Xiao, M. Pagliaro, Y.-J. Xu, B. Liu, *Chem. Soc. Rev.* **2016**, *45*, 3088-3121.
[3] M. C. Muñoz, J. A. Real, *Coord. Chem. Rev.* **2011**, *255*, 2068-2093.
[4] K. Otsubo, T. Haraguchi, H. Kitagawa, *Coord. Chem. Rev.* **2017**, *346*, 123-138.
[5] S. Sakaida, K. Otsubo, O. Sakata, C. Song, A. Fujiwara, M. Takata, H. Kitagawa, *Nat. Chem.* **2016**, *8*, 377-383.

In in situ X-ray diffraction study of phase-transitions upon CO_2 adsorption in an amine-functionalized porous coordination polymer.

Víctor Rubio-Giménez,[1] Carlos Bartual-Murgui,[1] Javier Castells-Gil, Sergio Tatay,[1] Carlos Martí-Gastaldo,[1] Christian Sternemann[2] and Jose A. Real,[1]

[1]Instituto de Ciencia Molecular, Universitat de València, Catedrático José Beltrán 2, 46980 Paterna, Spain.
[2]Fakultät Physik / DELTA, Technische Universität Dortmund, Maria-Goeppert-Mayer-Str. 2, D-44227 Dortmund, Germany.

The introduction of amine functionalities in porous coordination polymers (PCPs) has been a successful strategy to promote the selective absorption of CO_2.[1] Hofmann-type coordination polymers (HCPs) are a class of metal-organic materials composed by layers of alternating octahedral Fe^{II} and square planar Pt^{II} centers connected via cyanide groups.[2, 3] The Fe^{II} ions also are coordinated to two additional pillaring ligands, which stack the metal-cyanide sheets to form a 2D or 3D structure depending on their denticity. The layers of a 3D HCP are covalently bonded creating rectangular pore channels that run along the metal-cyanide sheets. We prepared a mixed ligand 3D HCP with an amine functionalized axial ligand which shows an irreversible magnetic transition after the first CO_2 absorption cycle. To investigate if this was due to a crystal phase transition we performed synchrotron in-situ powder X-ray diffraction (PXRD) studies at BL9 under variable CO_2 pressure.

We used a 20 keV XRD setup of BL9 with a MAR345 image plate detector. A sample-detector distance of 351 mm was determined after calibration with LaB_6. Powder samples were placed inside a sealed temperature-controlled chamber and CO_2 pressure was adjusted with a vacuum pump/needle valve/CO_2 canister and monitored with a manometer.

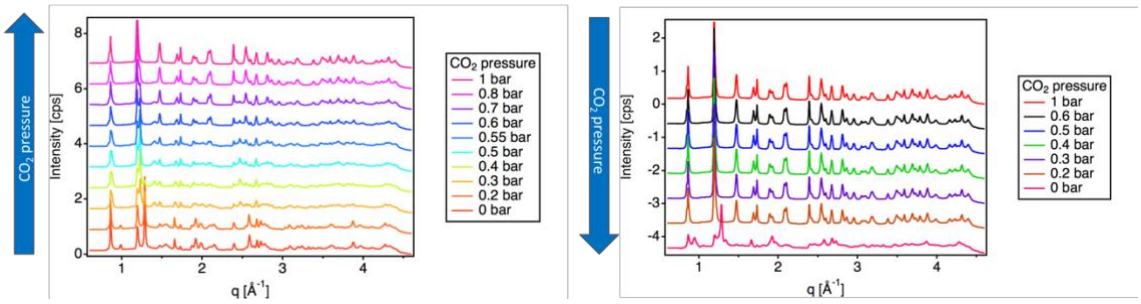

Figure 1. PXRD diffractograms of CO_2 absorption (left) and desorption (right) cycles for the amine-functionalized HCP.

As visible in Figure 1, upon the first exposure to CO_2 there is a dramatic change at 0.2-0.4 bar and then a more progressive transition until stabilization at 0.7 bar. In the desorption cycle, there is no change until 0 bar (vacuum) is reached. The initial diffractogram is not recovered after desorption, but after the sample is exposed again to a pressure of CO_2, there is another phase transition that is now fully reversible after desorption (Figure 2). Single crystal XRD studies are underway to try to precisely uncover the role of CO_2 in this structural transition.

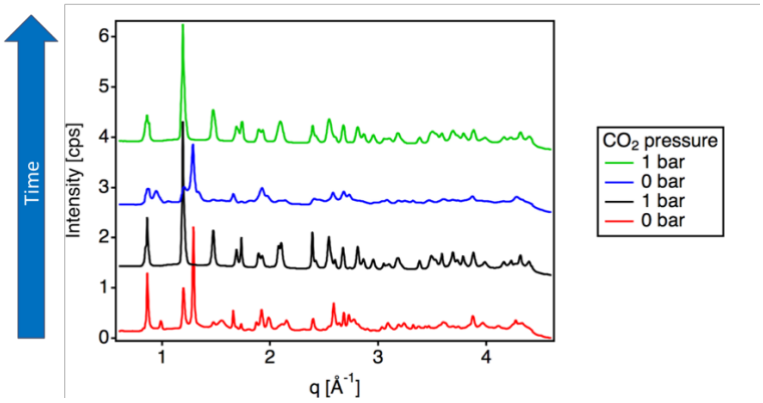

Figure 2. PXRD diffractograms of two consecutive CO_2 absorption/desorption cycles for the amine-functionalized HCP.

---

[1] A. J. Emerson, A. Chahine, S. R. Batten, D. R. Turner, *Coord. Chem. Rev.* **2018**, *365*, 1-22.
[2] M. C. Muñoz, J. A. Real, *Coord. Chem. Rev.* **2011**, *255*, 2068-2093.
[3] K. Otsubo, T. Haraguchi, H. Kitagawa, *Coord. Chem. Rev.* **2017**, *346*, 123-138.

Variable Temperature Powder X-ray Diffraction Study of Responsive Isoreticular Metal-Organic Frameworks

Roman Pallach, Louis Frentzel-Beyme, Sebastian Henke*

Anorganische Chemie – TU Dortmund, Otto-Hahn-Str. 6, 44227 Dortmund

Thanks to their potential application in a wide range of fields, metal-organic frameworks (MOFs), a young class of porous coordination compounds, have been in focus of much research effort in recent years. Notably, flexible MOFs, which are able to change their structure reversibly in response to external stimuli (e.g. guest adsorption, temperature changes, mechanical pressure, etc.), attract considerable attention because of their unique responsive properties.[1,2] Reversible switching between two different crystalline MOF phases as a function of guest adsorption is nowadays a well-understood phenomenon of flexible MOFs. Nevertheless, reversible crystalline-to-amorphous transitions remain rare and only barely understood. Despite being well-known for its structural rigidity[3,4], ether-functionalised derivatives of MOF-5 (abbreviated MOF-5(**CX**); with **X** corresponding to the number of carbon atoms of the substitutent; composition $Zn_4O((\mathbf{R}O)_2\text{-bdc})_3$; $(\mathbf{R}O)_2\text{-bdc}^{2-}$ = 2,5-dialkoxy-functionalised benzenedicarboxylate; **R** = linear alkyl group, C_XH_{2X+1}) undergo reversible phase transitions upon adsorption or desorption of guest molecules, such as *N,N*-dimethylformamide (DMF).[5]

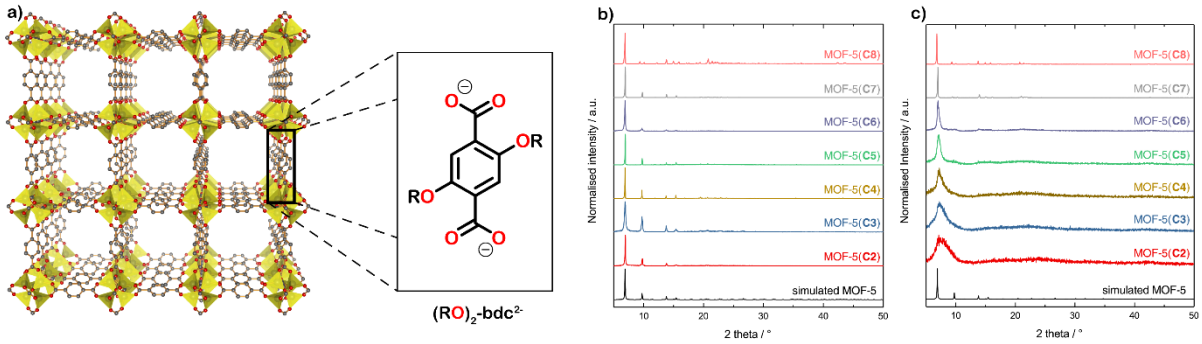

Fig. 1: a) Schematic representation of the crystal structure of the prototypical MOF-5 and the chemical structure of the utilized ether-functionalised bdc^{2-} linkers. Zn, O and C atoms are shown in yellow, red and grey. H atoms are omitted. b) Powder X-ray diffraction data of *as-synthesised* (DMF-containing) MOF-5(**C2**) to MOF-5(**C8**) in comparison with a simulated pattern of conventional MOF-5. c) Powder X-ray diffraction data of *dried* (guest-free) MOF-5(**C2**) to MOF-5(**C8**) in comparison with a simulated pattern of conventional MOF-5.

As subsequent studies on this phenomenon revealed, the degree of structural flexibility and responsiveness strongly depends on the length of the carbon chain implemented into the organic linker unit, giving either a switching between a cubic and a rhombohedral phase (from **C7** to **C8**) or a highly unusual switching between a cubic and a poorly crystalline, disordered phase (from **C2** to **C6**) (see Fig.1 a)). Further experiments (IR spectroscopy, single crystal XRD and X-ray pair distribution function analysis) indicate, that the observed phase behaviour is a result of concerted (**C7** to **C8**) or randomly occurring (**C2** to **C6**) structural distortions of the inorganic nodes of the framework, which most likely arise from weak dispersion interactions between the alkoxy chains attached to the organic linker and the backbone of the framework.

To further proof this theory, we collected variable temperature X-ray powder diffraction (VT-XRPD) data of our MOF-5(**CX**) samples at Beamline BL 9 of DELTA using an X-ray beam with an energy of 20 keV, a beamsize of 0.2 x 1 mm^2 and the MAR345 detector. Samples were heated from ambient temperature up to 500 K either applying the CryoStream or the Huber capillary heating setup. We were able to observe phase transitions of the rhombohedrally distorted MOF-5(**C7**) and MOF-5(**C8**) to the non-distorted cubic phase at elevated temperature (>350 K for MOF-5(**C7**) and >450 K for MOIF-5(**C8**); (Fig. 2). In contrast to this, the poorly crystalline, distorted framework of MOF-5(**C6**) transforms in a continuous manner to the cubic phase during heating up to 500 K. Counterintuitively, this suggests that the crystallographically ordered cubic phase appears to be entropically favoured over the disordered (but enthalpically favoured) X-ray amorphous phase. We interpret this as a result of a higher vibrational amplitude of the implemented alkyl chains at high temperatures, which counterbalance dispersion interactions between this groups and the backbone of the framework. For the highly distorted MOF-5(**C2**), however, no transition to the cubic phase could be observed upon heating the sample to 500 K. It is likely that the required transition temperature cannot be reached because the decomposition temperature of the sample is below the 'virtual' amorphous-to-cubic transition temperature.

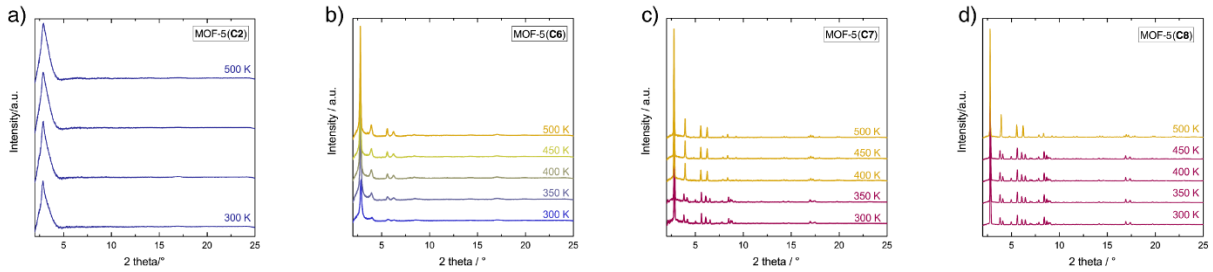

Fig. 2: VT-XRPD data from 300 to 500 K collected at BL9 of DELTA. Blue, magenta and yellow coloured XRPD patterns correspond to the amorphous / poorly crystalline, rhombohedrally distorted and cubic phases, respectively. a) MOF-5(**C2**), b) MOF-5(**C6**), c) MOF-5(**C7**), d) MOF-5(**C8**).

Our results demonstrate that linker functionalization can be a powerful tool to generate new interesting materials properties and even initiate flexible behaviour in a compound that was deemed to be rigid, such as MOF-5. We will now focus on a more detailed analysis of the observed structural transitions, e.g. by creating structural models to fit our data.

The authors thank the DELTA group for granting beamtime and the beamline scientists of BL9, C. Sternemann and M. Paulus, for their valuable support during these experiments.

References

[1] A. Schneemann, V. Bon, I. Schwedler, I. Senkovska, S. Kaskel, R. A. Fischer, *Chem. Soc. Rev.* **2014**, *43*, 6062–6096.
[2] Z. Chang, D. H. Yang, J. Xu, T. L. Hu, X. H. Bu, *Adv. Mater.* **2015**, *27*, 5432–5441.
[3] G. Férey, C. Serre, *Chem. Soc. Rev.* **2009**, *38*, 1380–1399.
[4] L. Sarkisov, R. L. Martin, M. Haranczyk, B. Smit, **2014**.
[5] S. Henke, R. Schmid, J. D. Grunwaldt, R. A. Fischer, *Chem. Eur. J.* **2010**, *16*, 14296–14306.

High Temperature X-ray Powder Diffraction to Investigate Melting of a Series of Porous Zeolitic Imidazolate Frameworks

Louis Frentzel-Beyme, Marvin Kloß, Roman Pallach, Sebastian Henke*

Anorganische Chemie – TU Dortmund, Otto-Hahn-Str. 6, 44227 Dortmund

Scientific context

Metal-organic frameworks (MOFs), a young class of porous coordination compounds, have in recent years been in focus of much research effort, thanks to their potential application in a wide range of fields. Much work has concentrated on the synthesis of new compounds for applications in gas storage and separation, while the inherent structural phase behaviour of MOFs as a function of fundamental thermodynamic variables, such as temperature or pressure, is only barely explored.[1,2] Investigations on the thermal behaviour of MOFs, however, are particularly important for their technological application. Typically, MOF compounds collapse at elevated temperature (200 – 600 °C) and their building units irreversibly decompose. However, some zinc-based zeolitic imidazolate frameworks (ZIFs), a subset of MOFs, feature high thermal stability and were recently shown to melt before decomposition.[3–5]

The ZIF exhibiting the lowest melting point (T_m ~ 435 °C) up to this point is a compound named ZIF-62(Zn) exhibiting the approximate chemical composition $Zn(im)_{1.75}(bim)_{0.25}$ (see Fig. 1 for structural details). We have recently synthesized the so far unknown isostructural cobalt derivative ZIF-62(Co) by simply replacing Zn^{2+} ions by Co^{2+} ions in the synthetic procedure. Thermogravimetric analysis / differential scanning calorimetry (TGA/DSC) experiments under an argon atmosphere of ZIF-62(Co) revealed a melting temperature of 432 °C (see Fig. 1c). We further found that T_m of ZIF-62(M) materials of the general composition $M(im)_{2-x}(bim)_x$ (with M^{2+} = Co^{2+} or Zn^{2+}) can be tuned by adjusting the concentration (x) of bim^- in these compounds. For ZIF-62(Co) T_m decreases from 432 °C for x = 0.30 to only 387 °C for x = 0.10. For ZIF-62(Zn) T_m decreases to only 372 °C for the composition $Zn(im)_{1.95}(bim)_{0.05}$. This is by far the lowest melting point ever reported for a MOF material.

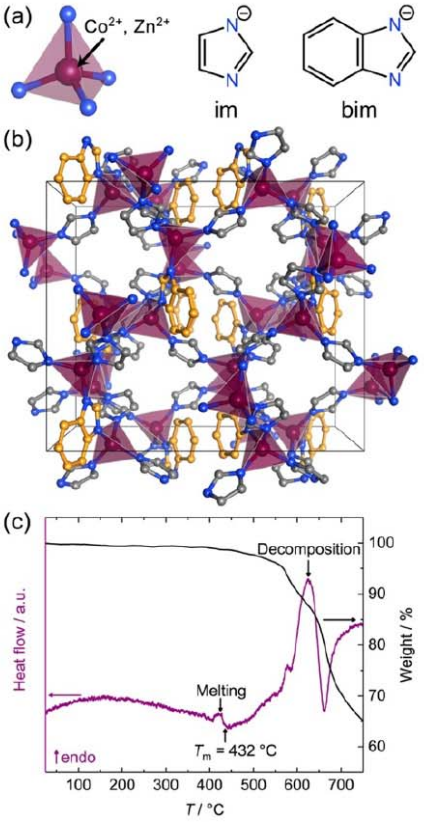

Fig. 1. (a) Scheme of the inorganic and organic building units of ZIF-62(M) materials. (b) Representation of the crystal structure of ZIF-62(M) based on its cobalt derivative viewed along the crystallographic b axis. The unit cell is shown with black lines. The positions of half-occupied bim^- linkers are highlighted in orange. (c) TGA/DSC data of ZIF-62(Co) with x = 0.30.

Experimental setup and aims

To further analyse the phase behaviour of the ZIF-62(M) compounds, high temperature X-ray powder diffraction (HT-XRPD) experiments were performed on seven compounds with varying $M(im)_{2-x}(bim)_x$ compositions (with M^{2+} = Co^{2+}, Zn^{2+}; x = 0.03 – 0.35) at beamline BL9 at DELTA with λ = 0.6199 Å using a MAR345 image plate scanner detector. The samples were

loaded in quartz glass capillaries and placed on an Anton Paar DHS1100 hot stage under a polyether ether ketone (PEEK) dome. With these experiments we can follow the melting process and correlate the X-ray scattering data with corresponding TGA/DSC data.

Results

All investigated samples showed a loss of Bragg scattering and the emergence of diffuse scattering characteristic for the ZIF liquid upon heating. We find a clear dependence of the amorphisation temperature (T_a) on the concentration (x) of the bim$^-$ in the framework (see Fig. 2). Nevertheless, T_a observed by HT-XRPD differs significantly from T_m as determined by TGA/DSC. Exemplarily, the HT-XRPD experiments revealed an amorphisation for ZIF-62(Zn)-bim$_{0.35}$ at approx. 360 °C (Figure 2, top-left), which is about 80 °C lower than T_m as detected in TGA/DSC.

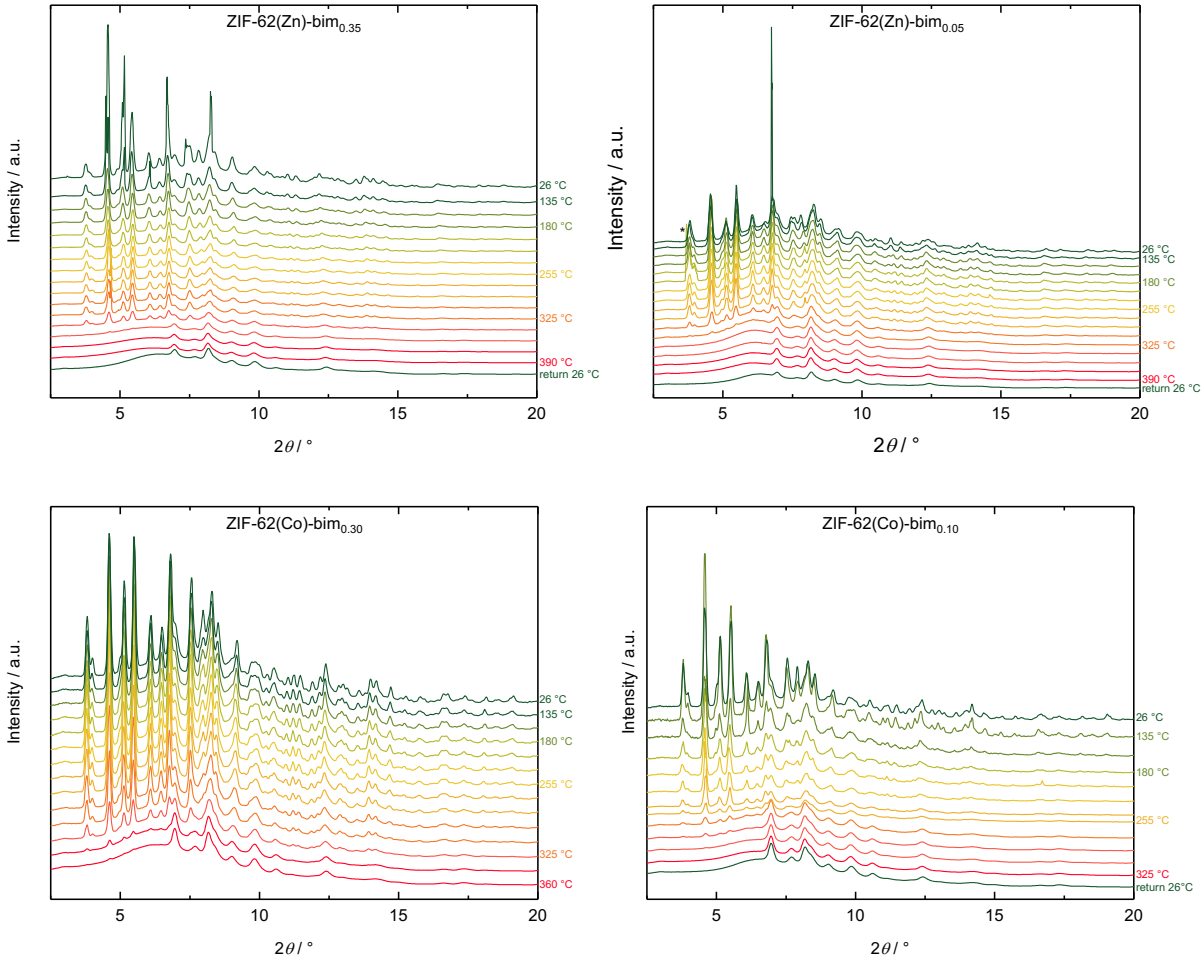

Fig. 2. Compilation of HT-XRPD patterns of four ZIF-62(M)-bim$_x$ materials. The patterns are not normalised but vertically offset for clarity. Unidentified artefacts are marked with an asterisk (*). In the case of ZIF-6(Co)-bim$_{0.30}$ a pattern after returning to ambient temperature has not been collected because of time constrains. The series of broader peaks from 2θ = 6.5° - 12.5° originate from the PEEK dome of the Anton Paar DHS1100 heating stage.

These differences could be explained by the dissimilar temperature-time profiles of the HT-PXRD (slow heating and holding T for several minutes for data collection) and TGA/DSC experiments (dynamic heating by 10 °C/min). It is also possible that bond breaking and rearrangement before melting results in an amorphous material, which is similar in energy to the original crystalline framework since no calorimetric signal is observed before the melting peak.

Importantly, when cooling the melted framework back to room temperature, a recrystallisation of the crystalline framework is not observed. This strongly suggests the formation of MOF glasses of similar composition to the crystalline ZIFs, but with a continuous random network topology analogous to silicate glasses.
The HT-XRPD data obtained during this beamtime are part of a publication, which has been submitted to a journal and is currently under revision.

The authors thank the DELTA group for the granted beamtime and the beamline scientists of BL9, C. Sternemann and M. Paulus, for the valuable support during the experiments.

References

[1] U. Mueller, M. Schubert, F. Teich, H. Puetter, K. Schierle-Arndt, J. Pastré, *J. Mater. Chem.* **2006**, *16*, 626–636.
[2] O. M. Yaghi, M. O' Keeffe, N. W. Ockwig, H. K. Chae, M. Eddaoudi, J. Kim, *Nature* **2003**, *423*, 705–714.
[3] R. Gaillac, P. Pullumbi, K. A. Beyer, K. W. Chapman, D. A. Keen, T. D. Bennett, F.-X. Coudert, *Nat. Mater.* **2017**, *16*, 1149–1154.
[4] H. Tao, T. D. Bennett, Y. Yue, *Adv. Mater.* **2017**, *29*, 1601705.
[5] T. D. Bennett, J. C. Tan, Y. Yue, E. Baxter, C. Ducati, N. J. Terrill, H. H. M. Yeung, Z. Zhou, W. Chen, S. Henke, et al., *Nat. Commun.* **2015**, *6*, 8079.

Investigating Narrow to Large Pore Phase Transitions of Pillared-Paddlewheel Frameworks as a Function of Temperature

Roman Pallach, Louis Frentzel-Beyme, Sebastian Henke*

Anorganische Chemie – TU Dortmund, Otto-Hahn-Str. 6, 44227 Dortmund

The term metal-organic frameworks (MOFs) refers to a young class of porous coordination compounds, which have been in focus of much research effort within the last years, since their intrinsic properties offer potential applications in a wide range of fields. If exposed to external stimuli, such as adsorption of gas or solvent molecules or changes in temperature and pressure, some MOFs undergo reversible structural transitions. This exceptional flexible behaviour makes these materials a fruitful target of research, aiming at future technological applications within the scope of sensing, gas separation/storage and heat storage or transfer.[1,2] Reversible switching between two different crystalline MOF phases as a function of guest adsorption is nowadays a well-understood phenomenon of flexible MOFs. Reversible phase transitions only as a function of temperature, however, are rare and barely understood.

We synthesised a series of novel pillared paddlewheel frameworks (PPFs) of the general chemical composition $Zn_2(R_2\text{-bdc})_2(dabco)$ (with $R_2\text{-bdc}^{2-}$ = 2,5-*dialkyl*-functionalised 1,4-benzenedicarboxylate; R = Me, Et, ^{n}Pr; dabco = 1,4-diazabicyclo[2.2.2]octane), which transform from a guest-containing large pore (***lp***) phase to a contracted narrow pore (***np***) phase upon removal of the guest molecules (Fig. 1). A similar behaviour was observed for related PPFs bearing a *dialkoxy*-functionalisation.[3,4]

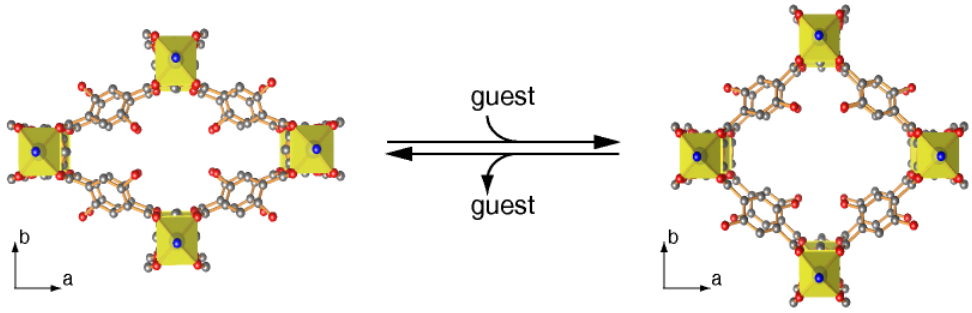

Fig. 1: Graphical representation of the reversible guest-induced narrow pore (***np***) to large pore (***lp***) transition of $Zn_2(R_2\text{-bdc})_2(dabco)$ (R = linear alkyl group) PPF materials. M, O, N and C atoms are shown in yellow, red, blue and grey. H atoms are omitted for clarity.

Typically, in these compounds the guest-free ***lp*** phase is entropically favoured at higher temperatures, since it allows for increased rotational and vibrational degrees of freedom of the side-chains. Therefore, we studied the phase behaviour of these novel *alkyl*-functionalised PPFs as a function of temperature by use of X-ray powder diffraction (XRPD) at beamline BL9 of DELTA. The samples were investigated in a temperature range from 300 to 500 or 600 K (depending on the utilized setup; either the CryoStream or the Huber capillary heating setup). An X-ray beam with an energy of 20 keV, a beamsize of 0.2 x 1 mm^2 and the MAR345 detector were used.

We observed significant variations in the phase behaviour of the investigated compounds as a function of the carbon chain-length of the alkyl substituents (see Fig. 2). The *dimethyl*-derivative does not contract to an ***np*** phase upon guest removal. It rather stays in the ***lp*** phase. The lp phase is stable up to 500 K. Upon further heating the material decomposes and forms a

different, so far unidentified phase at higher temperatures. The *diethyl*-functionalisation yields a PPF that features an ***np*** form at room temperature. At 423 K the materials starts to transform to the ***lp*** phase. The transition is completed at 523 K. At 573 K another transformation to a so far unidentified phase occurs. For the PPF derivative featuring the longer *dipropyl*-chains the np phase is stable up to 500 K (CryoStream heating setup). A pattern recorded at 500 K with the Huber capillary heating setup clearly shows a transition from the ***np*** to the ***lp*** phase. We speculate that the ***np-lp*** transition temperature for the *dipropyl*-PPF is slightly higher than 500 K, so that the transition could be initiated by an overshooting of the Huber heating setup.

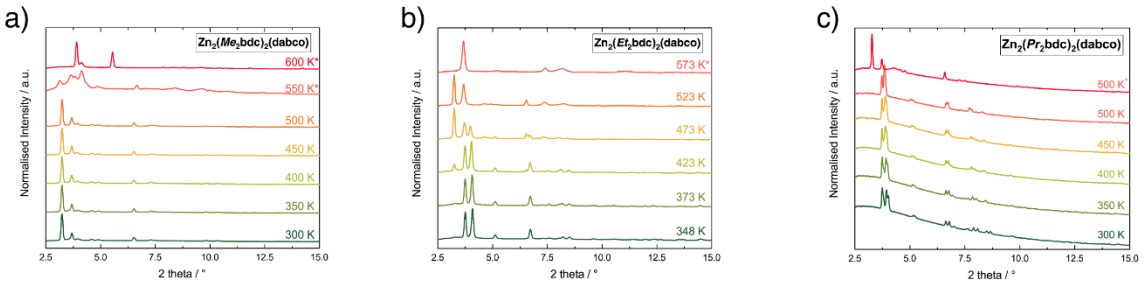

Fig. 2: Variable temperature XRPD data of $Zn_2(R_2\text{-bdc})_2$(dabco) with R = *methyl* (a), *ethyl* (b) or *propyl* (c) at BL9 of DELTA. If marked with an asterisk (*), measurements were performed using the Huber heating setup, otherwise the CryoStream setup was used. Above 550 K the *methyl*-compound (a) suffered from sample decomposition.

We will now evaluate the detailed crystallographic structures of the individual ***np*** and ***lp*** phases of these PPFs as well as their corresponding thermal expansion coefficients by sequential profile fitting (Pawley method) and Rietveld refinement.

The authors thank the DELTA group for granting beamtime and the beamline scientists of BL9, C. Sternemann and M. Paulus, for their valuable support during these experiments.

References

[1] A. Schneemann, V. Bon, I. Schwedler, I. Senkovska, S. Kaskel, R. A. Fischer, *Chem. Soc. Rev.* **2014**, *43*, 6062–6096.
[2] Z. Chang, D. H. Yang, J. Xu, T. L. Hu, X. H. Bu, *Adv. Mater.* **2015**, *27*, 5432–5441.
[3] S. Henke, A. Schneemann, A. Wütscher, R. A. Fischer, *J. Am. Chem. Soc.* **2012**, *134*, 9464–9474.
[4] I. Schwedler, S. Henke, M. T. Wharmby, S. R. Bajpe, A. K. Cheetham, R. A. Fischer, *Dalt. Trans.* **2016**, *45*, 4230–4241.

Temperature dependent behaviour of chromium nitride-based coatings

Jan Latarius[1], Dominic Stangier[2], Christian Albers[1], Kristina Berger[1], Alina Sparenberg[1], Michael Paulus[1], Wolfgang Tillmann[2], and Metin Tolan[1]

[1]Fakultät Physik / DELTA, TU Dortmund, University, Germany 44221
[2]Institute of Materials Engineering, TU Dortmund, Germany 44227 Dortmund, Leonhard-Euler-Straße 2

Modern production is in need for efficient high performance coatings to increase resilience against wear, fatigue and corrosion for tools and products [1]. Possible candidates are transition metal ceramics applied to the surface via physical vapor deposition (PVD). Our experiments employ X-ray diffraction (XRD) and take a look at the microscopic structure of chromium nitride (CrN) doped with aluminum and silicon.

Our samples were produced as an approximately $3\,\mu m$ thick top layer via PVD. Both a ceramic (WCCo) and steel (ASP 2023) substrate were chosen to compare their influence on the coating. In the course of the experiment at beamline 9, the samples were heated *ex-situ* from room temperature up to $900\,°C$.

As residual stress and grain size alter microscopic length scales in the affected lattice, their effects become visible in the gathered diffractograms. Global residual stress changes the positions of peaks whereas micro strains and grain size change their size and shape.

The XRD setup employing the MAR345-detector has been used and the beam energy was set to 20 keV. Different incident angles have been used ranging from 0.5 to 7.5 °.

Select results can be seen in figures 1 to 3. The Bragg reflections have been fitted with Pseudo-Voigt functions, as being displayed in figure 1. Albeit being noticeable the WC Eta phase has been neglected due to its inconsistent appearance.

The main phases have been identified as CrN in P1 structure (simple cubic) and WC in $P\bar{6}m2$ structure (trigonal prismatic). When taking a look at the CrN contribution in figure 2, a texture is noticeable in the caked detector images as can be seen in figure 2.

Skipping the inhomogeneities leads to well aligned fits and looking at the full-width half-maximum (FWHM) one can find contradicting trends for the CrN 111 and 200 reflex compared to the 220 reflex. These might be caused by an annealing process of the coating leading to preferred orientations.

These are only preliminary results and need further examination. For future experiments on this topic it might prove worthwhile to heat *in-situ* and explore the texture through microscopy.

References

[1] B Navinšek, P Panjan, and I Milošev. Industrial applications of CrN (PVD) coatings, deposited at high and low temperatures. *Surface and Coatings Technology*, 97(1):182 – 191, 1997.

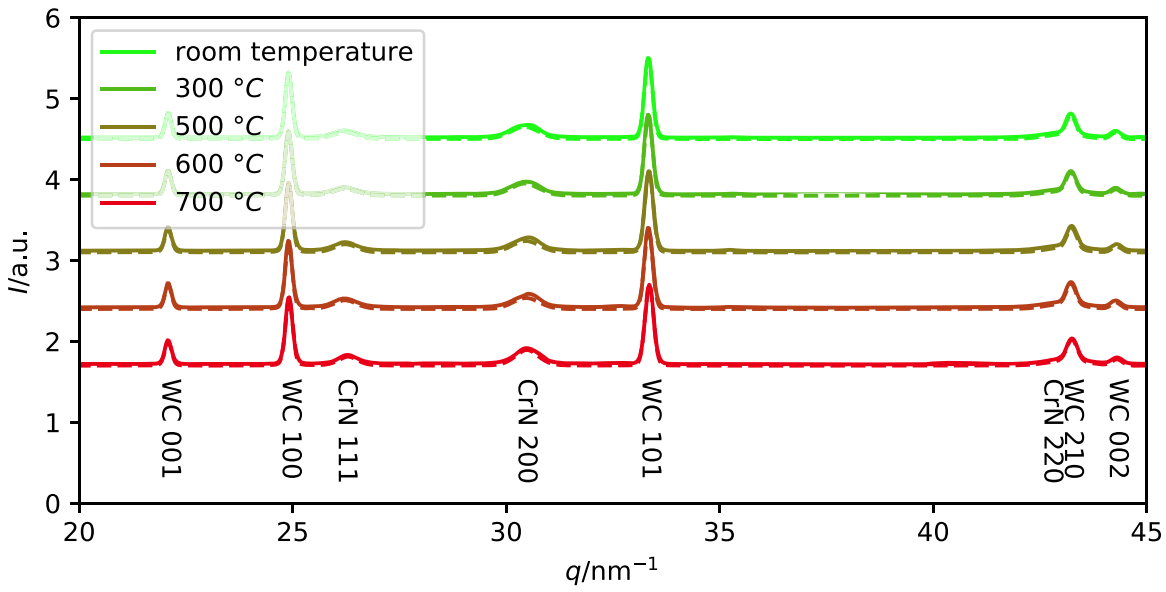

Figure 1: Diffractograms of CrAlN coatings on a WCCo substrate (solid) and the corresponding fits (dashed) at different temperatures at 20 keV and 5° incident angle. All graphs have been shifted vertically for clearance. The different reflections of the two main phases have been identified and annotated. Notice the protrusions on the CrN peaks likely caused by macroscopic crystallites.

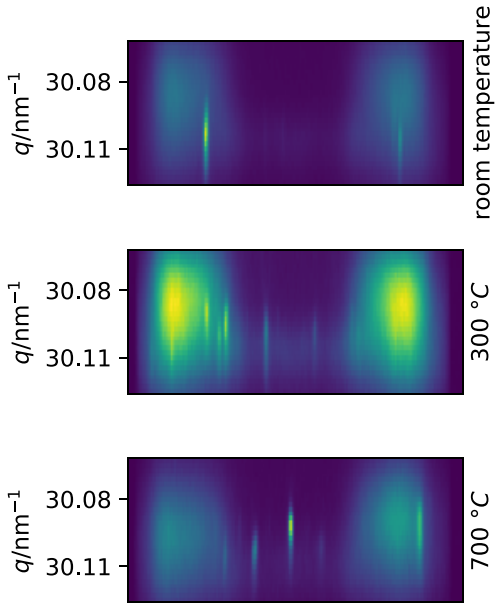

Figure 2: The top three sections show the hkl = 200 peak of CrN for three different temperatures after caking. Already here the delimited grains of CrN are identifiable.

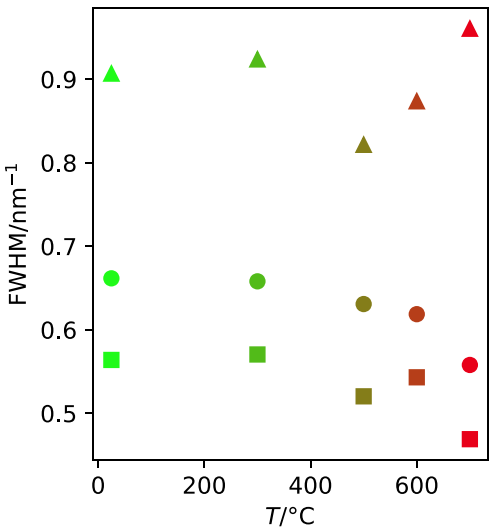

Figure 3: Full-width half-maximum of CrN peaks versus the temperature. Both, the 111 reflexes (squares) and the 220 reflexes (circles), follow a similarly decreasing trend towards higher temperatures. The 220 reflex (triangles) on the other hand do not adhere to it.

Small Angle X-Ray Scattering on Nanoporous Alumina

Mona Erfani, Ullrich Pietsch, Holger Schönherr, Universität Siegen

In our study we investigated polymer-filled nanoporous aluminum oxide using small angle X-ray scattering (SAXS) experiment in order to obtain information on characteristic sizes and filling state inside the pores after filling with a polymer. The results can be used to find optimum condition of sample preparation. Samples are disc-like alumina films with the diameter of 1 cm and thickness of 100 to 200 microns with pores prepared by anodic oxidation and are arranged hexagonally. As one can estimate from SEM images, the interpore distance is either 110 nm or 65 nm with pore diameter 70 nm and 40 nm, respectively. At first, pores were filled with PNIPAM with concentrations of 0.1 w%, 1 w% and 3 w% in solution. Measurements of filled and empty samples are done at room temperature. By adding water and increasing the temperature above 30°C, the polymer is expected to swell changing the scattering density of the nanoporous alumina. Data were analyzed modelling the intensity at central maximum I_0 and 2nd and 3rd local maximum I_2 and I_3 [1] and results are summarized in Fig.1. The model considers a gratings with material constants c_1 and c_2 and an *effective diameter ratio* $\frac{r}{d}$. However, the interpore distances are evaluated to be 101,3 nm and 67,3 nm and pore diameters are calculated as 68,46 nm and 45,31 nm for empty samples.

$$I_0 = \left(\frac{r}{d}\right)^2 + \left(1-\frac{r}{d}\right)^2 c_1^2 + 2\frac{r}{d}\left(1-\frac{r}{d}\right)c_1 c_2 \qquad (1)$$

$$I_m = \left(\frac{\sin\left(m\pi\frac{r}{d}\right)}{m\pi}\right)^2 (1 + c_1^2 - 2c_1 c_2) \qquad (2)$$

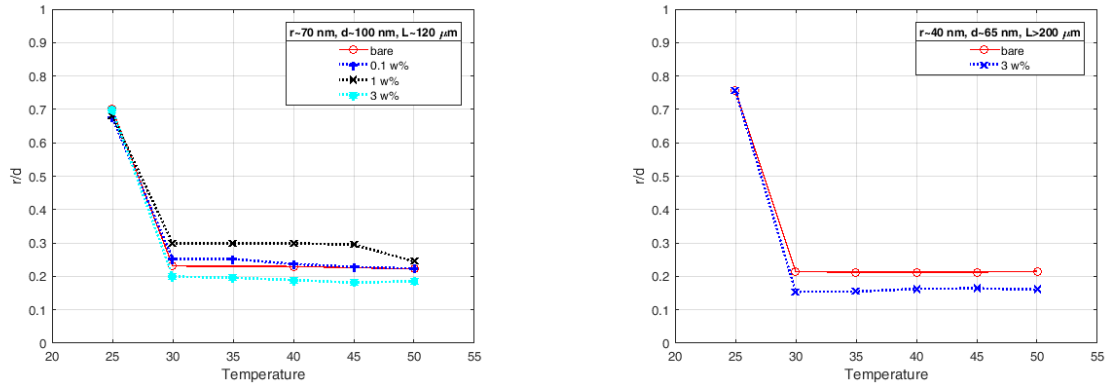

Fig.1. Effective diameter ratio as function of temperature for large (left) and small (right) samples

The low contrast makes a robust conclusion difficult and as this might affect the analysis, we added iron to polymer in order to increase the contrast and repeated the experiment at BL10. But as the physical conditions of the beamline is not appropriate for our measurements, a reliable calibration could not be reached. Therefore the experiment will be done again at BL9.

[1] L. E. Ruggles, M. E. Cuneo, J. L. Porter, D. F. Wenger, and W. W. Simpson, Rev. Sci. Ins. **72**, 1218 (2001)

In-situ GIXRD study of Cr-Ni steel surfaces heat treated under N_2/ SiH_4

D. Wulff[a], U. Holländer[a], D. Lützenkirchen-Hecht[b], B. Bornmann[b], R. Frahm[b], H.J. Maier[a]

a) Institut für Werkstoffkunde, Leibniz Universität Hannover, An der Universität 2, 30823 Garbsen
b) Fakultät 4 - Physik, Bergische Universität Wuppertal, Gaußstr. 20, 42097 Wuppertal

Introduction

In brazing technology the joining of components made of Cr-Ni steel is conducted under vacuum or inert gas atmospheres at temperatures above 900 °C. Appropriate gas atmospheres consist of inert N_2 or Ar and a reducing components like H_2 or SiH_4. The reducing agent is necessary to remove residual oxygen in the atmosphere so that an oxidation of the workpiece surface during the process is prevented. Previous investigations showed that under pure N_2 atmosphere different types of Cr and Fe oxides formed on 1.4301 at 1045 °C [1]. Nevertheless only a few publications deal with the behavior of Cr-Ni steel surfaces under N_2 doped with reducing SiH_4 [2, 3]. Further investigations were performed in this work, in order to analyze the temperature dependent interactions between steel surface and SiH_4-containing process atmosphere.

The measurements were run using circular samples made of 1.4571 (X6CrNiMoTi17-12-2 EU grad alloy) and 1.4301 (X5CrNi18-10, EU grad alloy). The stainless steel samples were polished to a final grading of 3 µm by diamond suspensions before the measurements to ensure reproducible starting conditions. The in-situ GIXRD measurements were performed at beamline 10 of the synchrotron radiation facility DELTA in a high temperature heater cell [4] under a N_2/SiH_4 atmosphere. The data were collected at an energy of 10 keV with a PILATUS 100K detector and a detector threshold of 8.5 keV. First of all the samples were examined at room temperature. Therefore a sequence of 12 single patterns (three incidence angles 1 °, 2 ° and 4 ° and four diffraction angles 25 °, 32.5 °, 40 ° and 48 °) were taken. A good data quality could be achieved by an integration time of 30 s per pattern. After the measurement at room temperature every sample was heated up to 1045 °C with a heating rate of 50 °C/ min. When the samples reached the measuring temperature they were aligned again to compensate the thermal expansion. After the collection of the second sequence of patterns at 1045 °C the samples were cooled to room temperature and were measured in this final state.

Results

In Fig. 1, GIXRD patterns of a 1.4301 and a 1.4571 sample heat treated under Ni/SiH_4 are shown. The data were collected at an incident angle of $\Theta = 2$ °. Before the heat treatment the patterns of both samples show three reflexes at room temperature with homogenous intensity distributions. The reflexes at 34.9 ° (♥1) and 40.4 ° (♥2) can be clearly assigned to γ-Fe. The third reflex belongs to α-Fe or martensite (♣1) and gets less intensive when the incident angle is increased, indicating that α-Fe or martensite exits near the surface only.

At 1045 °C the reflexes of the base material (♥1) and (♥2) show a slight shift of the peak positions induced by the thermal expansion of the lattice (see blue arrows in Fig 1.). The appearance of these reflexes also changed. A grain growth of 1.4301 was detected during heat treatment, which leads to inhomogeneous intensity distribution of the reflexes. Although the residual oxygen partial pressure was almost identical during both thermal treatments because of the same amount of SiH_4 doping (225 ppmv) the 1.4571 shows a less distinct grain growth than the 1.4301. The reflex (♣1) cannot be detected any longer at 1045 °C at both samples, so the surface-near α-Fe or martensite degenerated during the heat up period. Beside the reflexes of the base material serval additional reflexes are observed. On the 1.4571 seven new reflexes can be identified. Most of these reflexes belong to a mixture of Cr_2MnO_4 and $CrMnFeO_4$ (28.1 ° (♠1), 24.0 ° (♠2), 49.0 ° (♠3), 44.7 ° (♠4), 29.4 ° (♠5) and 42.0 ° (♠7)). One less intensive reflex can be assigned to Cr_2O_3 (♦).

On the other hand only two additional reflexes can be identified on the 1.4301 (28.1 ° (♠1) and 24.0 ° (♠2)). Both belong to a mixture of Cr_2MnO_4 and $CrMnFeO_4$. So it can be concluded that on 1.4571 much more oxide has formed during the heat up period than on the 1.4301 despite of the almost identical residual oxygen partial pressure. After the cooling down the peak positions of the reflexes are located at the room temperature position again. The intensity of the base material reflexes and the oxide reflexes have slightly increased. This can be traced back to the weakening of the intensity at higher temperature caused by the higher lattice vibrations of the atoms.

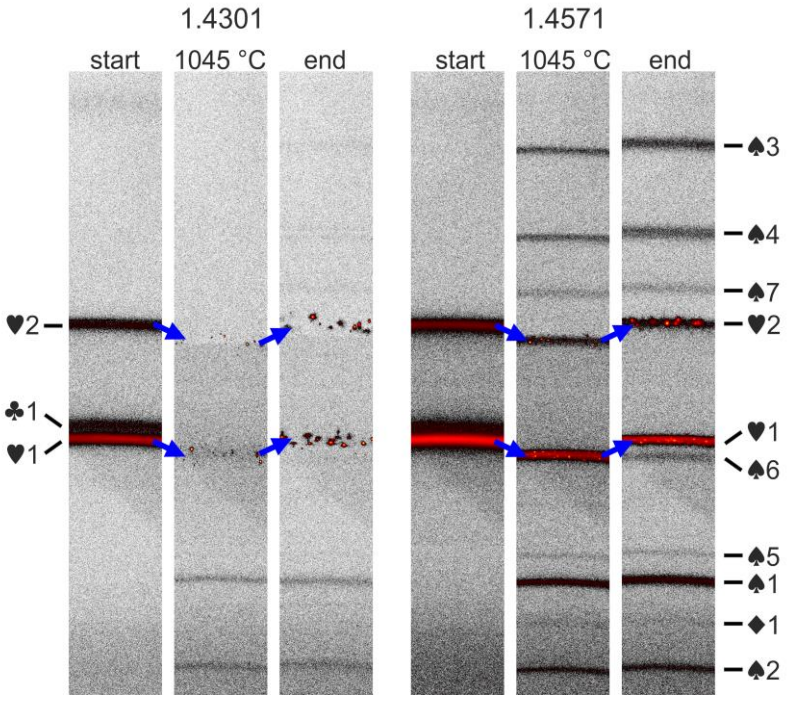

Figure 1: In-situ GIXRD investigation of a 1.4301 and a 1.4571 sample heat treated under N_2/SiH_4. The patterns were collected at an incident angle of Θ = 2 ° at room temperature before (start) and after (end) the heat treatment and at 1045 °C during the process. The peaks have been assigned as followed: γ-Fe (♥), α-Fe or martensite (♣), $Cr_2MnO_4/CrMnFeO_4$ (♠) and Cr_2O_3 (♦).

The pattern of the 1.4571 also shows an additional Cr_2MnO_4 /$CrMnFeO_4$ reflex at 34.2 ° (♠6). After the cooling phase several Cr_2MnO_4/ $CrMnFeO_4$ reflexes (♠3, ♠4, ♠5, ♠6 and ♠7) can be identified on the 1.4301 pattern as well, although their intensities are very low. It can be concluded, that most of the oxide species have grown in the heat-up and in the holding phase at 1045 °C, because the oxide reflex intensity of both samples do not strongly increase during the cooling phase.

In summary the performed GIXRD in-situ measurements are appropriate to study the oxidation processes on Cr-Ni steels under N_2/SiH_4 atmosphere at high temperatures. Further investigations should concentrate on the variation of the carrier gas (Ar instead of N_2), the variation of the residual oxygen partial pressure by variation of the SiH_4 content and the examination of the influence of the heat up and cooling time.

Acknowledgements

The research has been funded by the German Research Foundation (DFG, grant numbers MA1175/48-1 and FR1388/8-1). The authors gratefully thank the DELTA machine group for providing reliably synchrotron radiation.

References

[1] D. Wulff et al., In: Sternemann, C.; Wagner, R.; Lützenkirchen-Hecht, D. (Hrsg.): 13th DELTA User Meeting & Annual Report 2017. Dortmund, 29.11.2017, S. 43-44.
[2] D. Lützenkirchen-Hecht et al., J. Mater. Sci. 49 (2014) 5454-5461.
[3] D. Lützenkirchen-Hecht et al., Phys.: Conf. Ser. 712, 2016, 12047.
[4] B. Bornmann et al., In: Sternemann, C.; Wagner, R.; Lützenkirchen-Hecht, D. (Hrsg.): 12th DELTA User Meeting & Annual Report 2016. Dortmund, 30.11.2016, S. 11-13.

Tribological characteristics of newly developed PVD and Thermal Spray hard coatings at elevated temperatures

W. Tillmann[a], D. Kokalj[b] D. Stangier[c], L. Hagen[d]

Institute of Materials Engineering, TU Dortmund University, Germany
44227 Dortmund, Leonhard-Euler-Straße 2

[a]wolfgang.tillmann@uni-dortmund.de, [b]david.kokalj@uni-dortmund.de,
[c]dominic.stangier@uni-dortmund.de, [d]leif.hagen@uni-dortmund.de

Introduction

In terms of surface engineering, transition metals such as Ti, V, and Mo have attracted particular attention due to the formation of self-lubricous oxides. Using thermal spray technology and physical vapor deposition techniques, we recently determined an approach to deposit hard and wear resistant coatings incorporating V or Mo which act as oxide forming agents and thus favor tribo-oxidation phenomena at elevated temperatures in dry sliding experiments. As shown in [1], for tribologically stressed AlCrVxN coatings sliding against an inert counterbody, the reduction of the friction was attributed to different types of vanadium oxides at certain operating temperatures. With regard to PVD coatings, our major objective was the development of V-containing hard coatings incorporating V as a solid solution [1] as well as MoNx hard coatings [2]. In the field of arc spraying, a first attempt has very recently been made to produce a V-containing CoCr-based coating, using a non-commercial feedstock. We demonstrated that the produced CoCr-based coating, which additionally contains 21.75 wt.% of V, exhibited an improved wear resistance and a reduced friction in dry sliding tests at 750 °C compared to room temperature [3]. The sample exposed to 750 °C features an increased amount of $Co_3V_2O_8$ and elementary V, as well as some traces of VO_2 (or $Cr_{0.024}V_{0.976}O_2$) and $Cr(VO_4)$, respectively.

Experimental

Within this study, a newly developed arc sprayed CoCr-based coating which contains approximately 15.5 wt.% of V was tribologically examined with regard to its friction behavior. Wear mechanisms across the tribologically stressed surfaces were analyzed using electron microscopy. Afterwards, the coating surfaces were investigated by means of X-ray diffraction (XRD) at the beamline BL9 of the synchrotron light source DELTA. The photon energy was set to 13 keV (wavelength λ = 0.9537 Å) and a PILATUS detector system was used for the detection. The beam size was set to 0.1 x 1.0 mm^2 (v x h) and the angle of incidence was 3°. To distinguish between the temperature-induced phase transformation processes and the tribo-oxidation phenomena caused by sliding against the counterbody, the XRD measurements were carried out within as well as outside the wear track.

Results

For the tribologically stressed coating at 750 °C, the XRD analysis indicates that the coating surface is prone to form $Co_3V_2O_8$, $CoCrO_4$, and Co_3O_4 (Fig. 1), as well as some traces of CoO. In contrast, such spinel or mixed oxides cannot be found in the coating surface at room temperature within the experimental resolution. Furthermore, a hexagonal structure of the Co phase is detected in the produced coating at room temperature, i.e. without a heat treatment that is related to the as-sprayed conditions, respectively. In contrast, the Co phase of the heat treated coating exhibits a cubic structure. When compared to the coating surface, the XRD patterns reveal that no changes in the phase composition at the tribologically stressed surface occurs, i.e. the wear track.

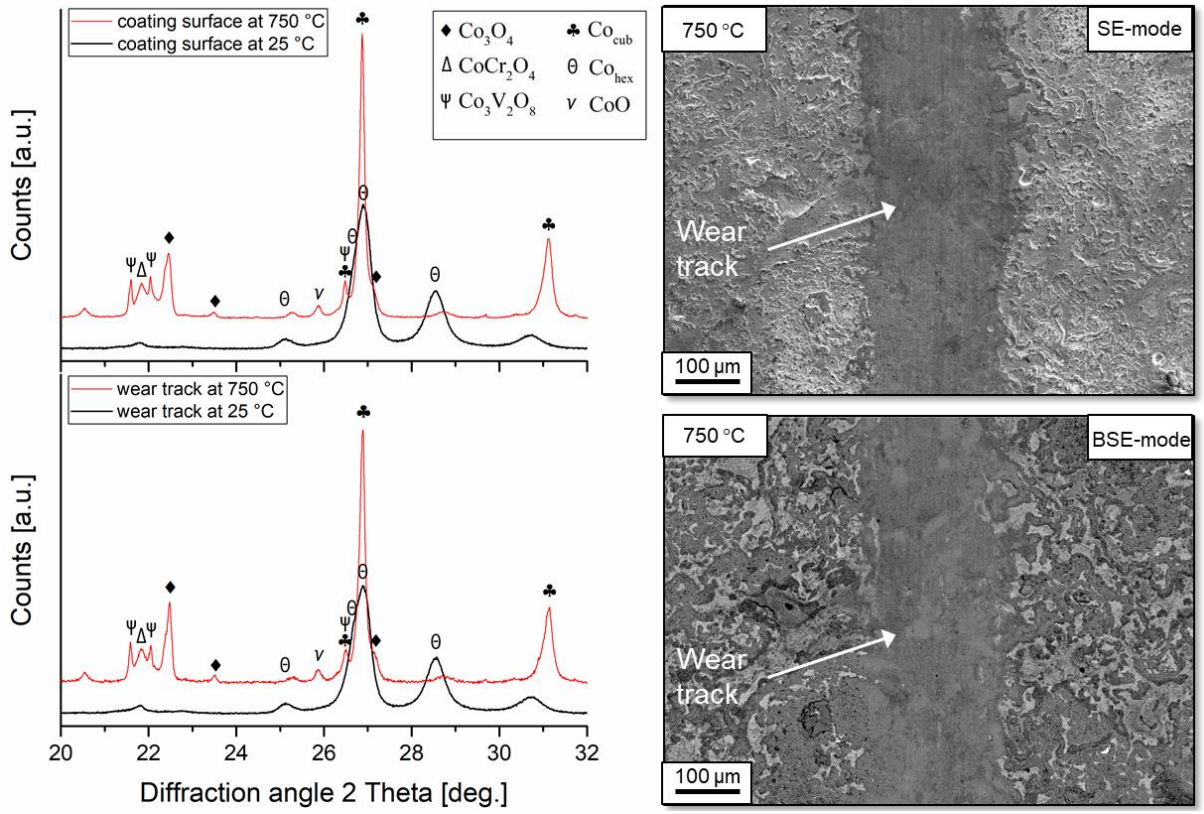

Fig. 1: XRD patterns that show the phase composition for different spots across the coating surface in dependency of the temperature applied during tribological testing (left); Scanning electron microscope images showing the tribologically stressed surface of the coating at 750 °C, detecting the signal of backscattered electrons (BSE-mode) and secondary electrons (SE-mode) (right)

Nevertheless, the phase evolution in arc sprayed deposits predominantly depends on inherent process characteristics such as constitutional supercooling during the rapid solidification of spray particles, which leads to a widely varying non-equilibrium state. In order to understand the phase transformation processes, further XRD analyses (ex-situ, in-situ) have to be conducted.

With regard to the resulting coating properties, it was revealed that the V-containing CoCr-based coating produced consists of a heterogeneous lamellar microstructure with chemically, individually composed lamellae, which corresponds with the previous observations for V-containing CoCr-based arc sprayed coatings with a high V content [3]. In terms of the newly developed arc sprayed V-containing CoCr-based coating, dry sliding experiments at different temperatures reveal that the coating possesses a severe-to-mild wear transition with an increase in temperature, whereas the coefficient of friction (COF) decreases significantly. Thus, a comparison of the measured values between room temperature and 750 °C shows that the COF decreases by more than 30 %. Electron microscopy (data not shown) demonstrates that the wear mechanism was gradually changed from abrasive wear at room temperature to tribo-oxidation at elevated temperatures. The surface oxidation was amplified at a temperature of 750 °C. Oxidation phenomena favored the development of a protective glaze in the contact zone, which was sliding against the counterbody (Fig. 1, right). After testing at 750°C, a small amount of material adheres onto the wear flat of the counterbody (data not shown). In contrast, after testing at room temperature, it was revealed that the wear flat of the counterbody is worn abrasively. To substantiate the occurrence of oxidation phenomena (e.g. thin oxide films) that leads to a self-lubricating behavior, further surface-sensitive methods need to be used.

Acknowledgement

We gratefully acknowledge the support of DURUM Verschleissschutz GmbH for providing the vanadium-containing feedstock material. The authors thank the DELTA machine group for providing the synchrotron radiation.

References

1. Tillmann, W.; Kokalj, D.; Stangier, D.; Paulus, M.; Sternemann, C.; Tolan, M.: Investigation on the oxidation behavior of AlCrVxN thin films by means of synchrotron radiation and influence on the high temperature friction. In: Applied Surface Science 427 (2018) S.511-521.
2. Tillmann, W.; Kokalj, D.; Stangier, D.: Influence of the deposition parameters on the texture and mechanical properties of magnetron sputtered cubic MoNx thin films. (2018), (submitted)
3. Tillmann, W.; Hagen, L.; Duda, D.: A Study on the Tribological Behavior of Arc Sprayed Vanadium doped Stellite Coatings. In: Proceedings of the International Thermal Spray Conference & Exposition, 2017, June 7-9, Düsseldorf, Germany

DELTA user report 2018
Proposer: Prof. Dr.-Ing. A. Ludwig
Co-Proposers: S. Salomon, P. Decker, M. Wambach

Investigation of phase formation and identification of impurity phases in a CoMnGe-Al-Si magnetocaloric thin film materials library using automated GI-XRD methods

S. Salomon
Werkstoffe der Mikrotechnik, Institut für Werkstoffe, Fäkultät Maschinenbau
Ruhr-Universität Bochum, D-44801 Bochum

Previous research focused on the ternary system Co-Mn-Ge [1] and quaternary derivatives including Al and Si (to be published) with respect to a so called giant magnetocaloric effect (GMCE). The GMCE leads to a change in the materials temperature upon a change in the magnetic field strength to which it is exposed. For it to occur, a coupling between a magnetic and a structural phase transition is necessary [2]. It is known that the CoMnGe phase undergoes a structural transition between the hexagonal CoMnGe high-temperature (HT) phase (space group P63/mmc) and the orthorhombic CoMnGe low-temperature (LT) phase (space group Pnma) [3] and a magnetic transition between a ferro- and a paramagnetic state [4], which can be coupled for a composition of $Co_{0.95}MnGe_{0.97}$ [5]. However, to enable fine tuning of the GMCE in terms of optimal working temperature, effect size and hysteretic behavior, a more thorough investigation of the ternary system as well as multinary derivatives is necessary.

To analyze a large variety of different compositions in high-throughput experiments, a CoMnGe-Al-Si thin film materials library (ML) was fabricated by sputter deposition (DCA Instruments, Finland) in a multilayer approach (nominal overall film thickness of 500 nm) on a (100) Si substrate with a 1.5 µm SiO_2 diffusion barrier. While Co, Mn and Ge were deposited as homogenous layers with a nominal atomic ratio of 1:1:1 for these three elements, a composition variation for Al and Si (~0 at.% up to ~5 at.% each; perpendicular to each other; compare Figure 1 a)) was achieved by using programmable shutter blades to grow wedge-type layers. The ML was annealed in Ar atmosphere at 600°C for 2 hours to facilitate diffusion and phase formation in the thin film. A preliminary phase analysis was performed based on EDX (INCA X-act detector, Oxford Instruments) and XRD (D8 DISCOVER, Bruker) mapping results of 342 individual measurement areas (see Figure 1 b)).

Prior research and the preliminary phase analysis showed the need for high quality diffraction data due to the possible presence of impurity phases that are difficult to identify alongside the desired CoMnGe phase. These difficulties are either caused by overlaps of the most prominent diffraction peaks (as is the case for Co_2MnGe together with CoMnGe) or very low intensity diffraction signals due to low fractions of impurity phases being present. To be able to reliably identify occurring impurity phases in the ML, grazing incidence diffraction experiments (GI-XRD) were performed at BL 9. Because of the low composition gradients across the ML for Al and Si, GI-XRD was

performed on every second measurement area of the 342 defined areas and some additional measurement areas selected during the beamtime based on the collected data. The experiments were performed with a beam energy of 20 keV, an irradiated area of approx. 1 mm x 1 mm and an incidence angle of $\Theta = 3°$ using a mar345 image plate detector.

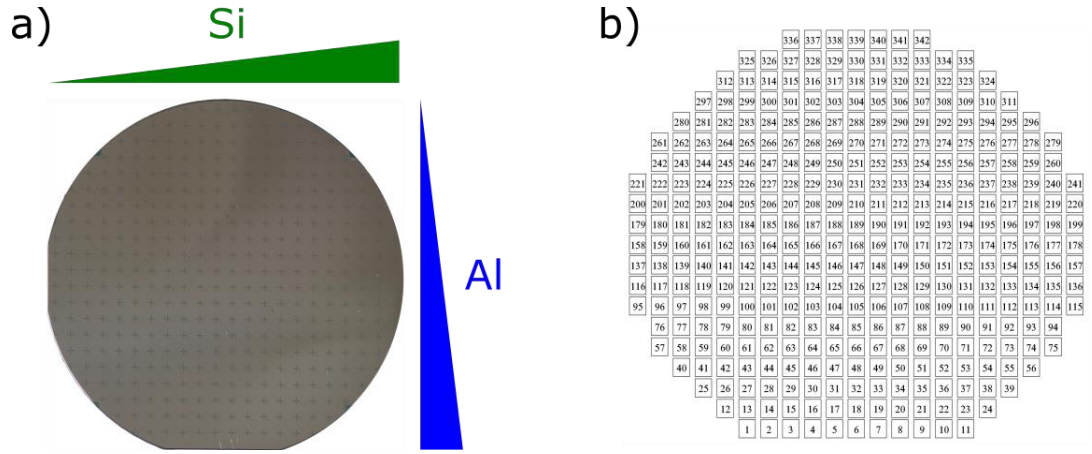

***Figure 1**: a) Photography of the annealed CoMnGe-Al-Si ML with schematic depiction of the Al and Si composition gradients. The cross pattern was created using a lift-off process and is used to easily identify the measurement areas b) that make up a grid defining 342 individual measurement areas.*

For high-throughput analysis, the 2D GI-XRD data was integrated and exported via macro using the FIT2D software [6,7]. To identify different phase regions from this data, cluster analysis was performed using the CombiView software [8]. Three different phases were identified in the ML, namely CoMnGe (HT), CoMnGe (LT) and Co_2MnGe. While CoMnGe (HT) is present across the whole ML, both CoMnGe (LT) and Co_2MnGe cannot be identified for high Si and Al contents (see Figure 2 a)). The boundary between those phase regions can roughly be defined by the combined contents of Al and Si. In this regard, Co_2MnGe is not stable for combined contents of Al and Si being > 8 at.%. Because the Co_2MnGe (space group Fm-3m) phase is mainly characterized by the (220) diffraction signal near 44.8° which coincides with the (110) signal from CoMnGe (HT), presence of this phase has to be inferred from the (400) diffraction signal at ~65° (compare Figure 2 b)). This signal can be identified well due to the high quality of the herein presented measurement data. However, because of its low relative intensity compared to the (220) signal, it is possible that Co_2MnGe is stable for a larger composition range than indicated here.

For high contents of both Si (~ 4 at.%) and Al (~ 6-7 at.%) combined, CoMnGe (HT) was identified exclusively (compare Figure 2 b)). This seems to imply that both Al and Si can stabilize the high temperature phase and probably influence the structural transition temperatures significantly. However, the ratio of Co, Mn and Ge slightly changes across the ML and thus deviates from the nominal ratio of 1:1:1. The influence of these deviations has to be carefully considered too. XRD(T) measurements are planned to test the aforementioned assumption and gather more detailed

information on the transition temperatures and the transition hysteresis widths, both important factors in regards to the GMCE, for different measurement areas.

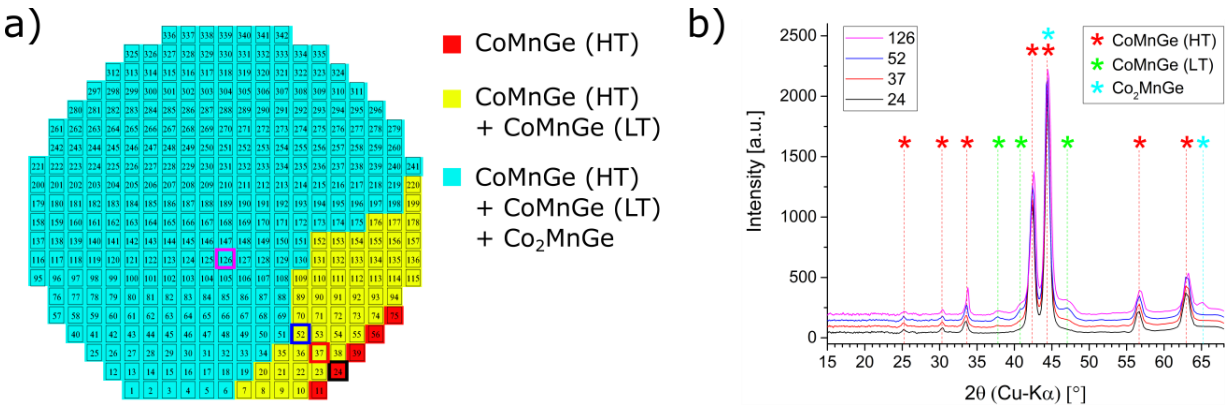

***Figure 2**: a) Identified phases in the ML correlated to the measurement areas. For high contents of Al and Si the CoMnGe phase exists exclusively, as indicated by the red and yellow areas. b) Integrated diffraction patterns for select measurement areas (as indicated by the colored boxes in a)) showing the occurrence of the different phases. The existence of Co_2MnGe needs to be inferred from the diffraction peak at ~65°.*

This research is part of the SPP 1599 funded by the DFG. The authors would like to thank the DELTA board for granting beamtime and Dr. C. Sternemann and Dr. M. Paulus for their support and help at the beamline.

References

[1] S. Salomon, S. Hamann, P. Decker, A. Savan, L. Meshi, A. Ludwig, Combinatorial synthesis and high-throughput characterization of the thin film materials system Co-Mn-Ge: Composition, structure, and magnetic properties, Phys. Status Solidi A 212 (2015), 1969–1974
[2] J. Liu, T. Gottschall, K.P. Skokov, J.D. Moore, O. Gutfleisch, Giant magnetocaloric effect driven by structural transitions, Nature materials 11 (2012), 620–626.
[3] V. Johnson, Diffusionless orthorhombic to hexagonal transitions in ternary silicides and germanides, Inorg. Chem. 14 (1975), 1117–1120
[4] S. Lin, O. Tegus, E. Bruck, W. Dagula, T.J. Gortenmulder, K. Buschow, Structural and Magnetic Properties of MnFe1-xCoxGe Compounds, IEEE Trans. Magn. 42 (2006), 3776–3778
[5] J. Liu, K. Skokov, O. Gutfleisch, Magnetostructural transition and adiabatic temperature change in MnCoGe magnetic refrigerants, Scripta Materialia (2012), 66, 642-645
[6] A. P. Hammersley, FIT2D: An Introduction and Overview, ESRF Internal Report (1997), ESRF97HA02T
[7] A. P. Hammersley, S. O. Svensson, M. Hanfland, A. N. Fitch, D. Häusermann, Two-Dimensional Detector Software: From Real Detector to Idealised Image or Two-Theta Scan, High Pressure Research (1996), 14, 235-248
[8] I. Takeuchi, C.J. Long, O.O. Famodu, M. Murakami, J. Hattrick-Simpers, G.W. Rubloff, M. Stukowski et al., Data management and visualization of x-ray diffraction spectra from thin film ternary composition spreads, Rev. Sci. Instrum. 76 (2005), 62223

Hard X-ray spectroscopy

EXAFS investigations of nanosized Co-electrodeposits

D. Lützenkirchen-Hecht[a], D. Hamulić[b], R. Wagner[a], I. Milošev[c]

(a) Fk. 4 – Physik, Bergische Universität Wuppertal, D-42097 Wuppertal, Germany.
(b) University of Ljubljana, Faculty of Chemistry and Chemical Technology, SI-1000 Ljubljana, Slovenia.
(c) Jožef Stefan Institute, Department of Physical and Organic Chemistry, *SI-1000 Ljubljana, Slovenia.*

Electrodeposition (ED) is a very versatile, but on the other hand very simple and easy to use technique for the preparation of thin films on conducting or semiconducting substrates. Film preparation by ED employs an electrolyte with positive cations of the element of interest. The deposition occurs if a cathodic voltage, negative with respect to the Nernst equilibrium potential, is applied to a conducting substrate electrode. In addition to the choice of the deposition potential which controls the thermodynamics of the deposition processes, ED offers manifold additional opportunities to control the film deposition, e.g. by the concentration of the anions and cations in the solution and additives which may promote certain growth modes, or by a variation of the temperature and the pH of the deposition solution (see e.g. ref. [1]). As a consequence, ED is not limited to the preparation of metals, but instead, a large variety of metals, alloys, semiconductors and insulators may be prepared, and thus ED became a frequently used technique for the preparation of materials with tailored properties.

Here we have investigated the structure of Co-deposits on Gold-coated, flexible polyimide (Kapton) substrates by means of X-ray absorption spectroscopy at DELTA beamline 10 [2], making use of a standard setup with gas-filled ionization chambers as detectors for the incident and transmitted X-rays. Cobalt-based materials are of high technological interest because of their manifold use e.g. in in magnetic storage devices [3], solid-oxide fuel cells [4], or batteries [5]. Previous experiments have shown that a deposition from $CoCl_2$-solutions leads to metallic deposits, the structure, thickness and morphology of which sensitively depends on the concentration of the solution, its temperature and the deposition time [6]. Here we present a more detailed analysis of the X-ray absorption fine structure data, i.e. quantitative fits of the experimental data. In order to achieve statistically meaningful results, we tried to keep the number of fit parameters as small as possible. In particular we have used the hcp space group no. 194, with lattice constants a = b = 2.505 Å and an elongated c axis with c = 4.0695 Å. The angles between the axis are $\alpha = \beta = 90°$, and $\gamma = 120°$. All atoms included in a radius of 5.0 Å around the central atom were considered in the fit, resulting in a cluster of 56 atoms and comprising a total of 13 different scattering paths, i.e. 5 single scattering and 8 multiple scattering paths. We have assumed a global lattice expansion parameter, meaning that all the bond distances calculated for the above mentioned hcp lattice were simply scaled by a single factor that turned out to be close to unity. Furthermore, a single values for the inner potential shift ΔE_0 and the amplitude reduction factor S_0^2 were used as fit variables. Finally, it was hypothesized that the mean squared relative displacement σ_1^2 is identical for all Cobalt atoms considered in the fit, which is a rather large simplification. However all those assumptions lead to only 4 independent fit parameters in relation to the number of independent data points $N_{idp} = 28$ that results from the large ranges in k- and R-space used for the fit, making the fits appear statistically meaningful. The fits presented here were performed using the Artemis software [7].

As can be seen in Fig. 1, the experimental data can be well described by such a simple fit model, i.e. the magnitude of the Fourier-transform of the k^3-weighted EXAFS function $|FT(k^3*\chi(k))|$ measured from a Co-film deposited at -1.11 V in 0.02M $CoCl_2$ for 300 s resulting in a film thickness of ca. 140 ± 5 nm [6] is well reproduced by the fit in the entire R-range considered here, i.e. from 1.1 Å to 5.0 Å, and also the back-transformed data match the experimental data well in the k-range from 2.7 $Å^{-1}$ to 14 $Å^{-1}$. A survey of the obtained fit results for the nearest neighbor bond distance R_1 and the related mean squared displacement σ_1^2 is presented in Fig. 2 as a function of the nominal Co film thickness. Compared to the Co-Co distance R_1 for the Co metal reference material of 2.488 Å ± 0.002 Å, R_1 seems to show a substantially larger bond distance about 2.502 Å ± 0.003 Å for a film thickness of 140 nm, that decreases to about 2.494 Å ± 0.002 Å for 3.2 μm thickness. In contrast, the values determined for σ_1^2 do not change systematically with film thickness with an average value of 0.007 $Å^2$. The results suggest that the lattice of the electrodeposits relaxes during film growth, with a substantially larger bond length for the smaller crystallites with needle-like shaped crystallites, and a smaller bond length for the larger, spherical particles for larger film thickness [6].

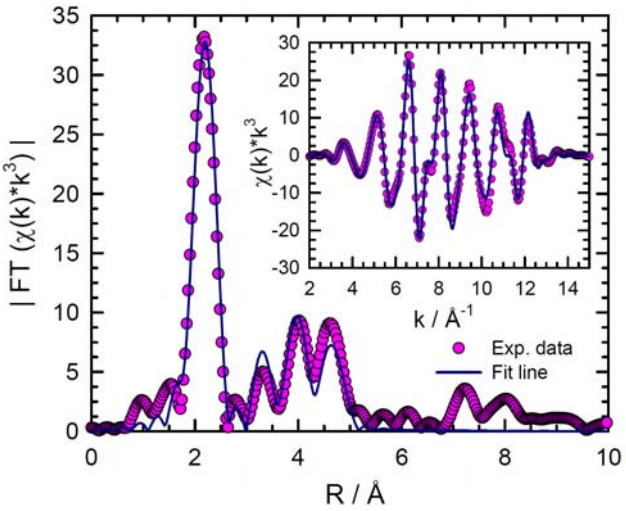

Fig. 1: Magnitude of the Fourier-transforms $|FT(k^3*\chi(k))|$ of the EXAFS data a Co-film deposited at -1.11 V in 0.02M $CoCl_2$ for 300 s, resulting in a film thickness of about 140 nm. The experimental data (•) as well as the fit (—) using the structure of hcp-cobalt are displayed (see text for details). In the insert, the back-transformed data in k-space are shown. The k-range for the Fourier-transform is 2.7 $Å^{-1}$ < k < 14.0 $Å^{-1}$ and the fit was performed in a radial distance of 1.1 Å – 5.0 Å.

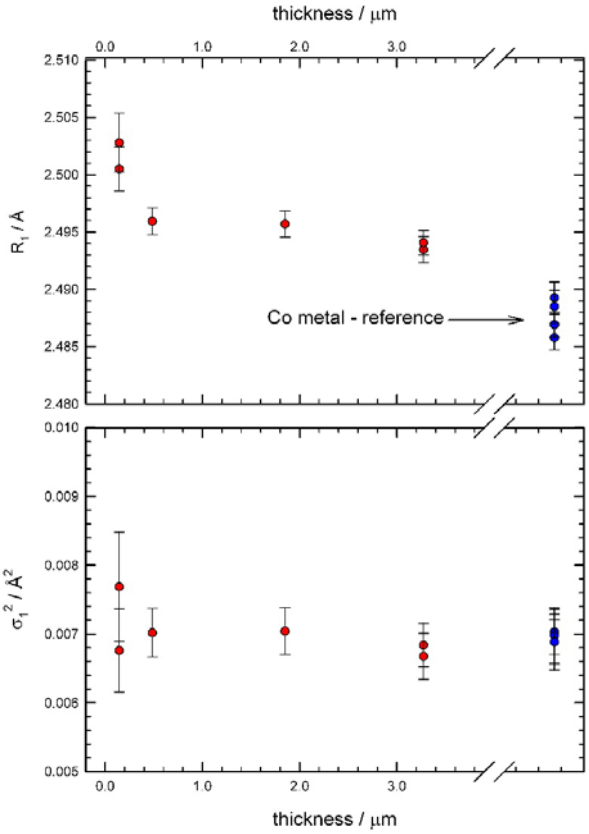

Fig. 2: Compilation of fit results obtained from a detailed analysis of the EXAFS data of Co deposits in 0.02M $CoCl_2$ as a function of the nominal film thickness: Evaluation of nearest neighbor bond distance R_1 and mean squared relative displacement σ_1^2.

Acknowledgements

D. Hamulić gratefully acknowledges the financial support from the ERASMUS student exchange program for his visit in Germany. We like to thank the DELTA machine group for providing synchrotron radiation for the presented experiments.

References

[1] E.M. Garcia, V.F.C. Lins, T. Matencio. "Metallic and Oxide Electrodeposition." In: Modern Surface Engineering Treatments. M. Aliofkhazraei (Ed.), IntechOpen (2013) DOI: 10.5772/55684.

[2] D. Lützenkirchen-Hecht, R. Wagner, S. Szillat, A.K. Hüsecken, K. Istomin, U. Pietsch, R. Frahm, J. Synchrotron Radiat. 21 (2014) 819.

[3] H. Yoon, A. Xu, G.E. Sterbinsky, D.A. Arena, Z. Wang, P.W. Stephens, Y.S. Meng, K.J. Carroll, Phys.Chem.Chem.Phys. 17 (2015) 1070

[4] T. Guo, X. Dong, M.M. Shirolkar, X. Song, M. Wang, L. Zhang, M. Li, H. Wang, ACS Appl. Mater. Interfaces 6 (2014) 16131.

[5] X. Zhao, L. Ma, X. Shen, J. Mater. Chem. 22 (2012) 277.

[6] D. Hamulic, I. Milosev, D. Lützenkirchen-Hecht, Thin Sol. Films 667 (2018) 11.

[7] B. Ravel, M. Newville, J. Synchrotron Radiat. 12 (2005) 537.

Surface characterization of orthopedic titanium implants by X-ray diffraction and X-ray fluorescence

K. Berger, M. Paulus, A. Sparenberg, C. Sternemann J. Latarius, C. Albers, M. Tolan

Fakultät Physik/ DELTA, TU Dortmund

Commercially pure titanium and its alloys truly have become the fundamental biomaterial used in orthopedic and dental applications due to their excellent biocompatibility. Biocompatibility is accomplished by a thin titanium oxide layer (TiO_2) which spontaneously forms on its surface when exposed to air or other oxygen containing environments. This protective layer is typically 5-10 nm thick and reduces the reactivity of the metal which is responsible for its excellent corrosion resistance. In case of damage the oxide layer immediately initiates the process of self-healing, if oxygen is present [1].

The purpose of the first experiment presented here is to investigate the elemental composition of oxide layer on implants made from commercially pure titanium and also from an alloy (TiAl6V4) by X-ray fluorescence analyses using synchrotron radiation. For this analysis, excitation with a polychromatic beam (BL2) and fluorescence detection by an *Aptek X-123* X-ray spectrometer is used. Four titanium implants (distal tibia plate, distal fibula plate, distal femur plate and proximal humerus plate) from different manufacturer are investigated. The distal tibia, distal fibula and proximal humerus plate are commercially pure titanium implants (Grade 2: 99.57%) whereas the distal femur plate represents the alloy TiAl6V4 [2].

Figure 1 shows the comparison of the normalized energy dispersed spectra of the measured titanium implants. The spectra show that titanium and iron are detected in all of the investigated samples. This result is in common with the producers specifications and DIN EN ISO 5832-2 (unalloyed titanium) DIN ISO 5832-3 (TiAl6V4). A comparison between commercially pure titanium and TiAl6V4 alloy reveals many similarities, but also some significant differences between the two materials, for instance the appearance of vanadium in the proximal humerus plate spectrum. Light elements, such as C, O, H or Al could not be detected by the experiment. In addition the peaks derived from zirconium are noted on all implants surfaces. Thus, we conclude that small amounts of zirconium oxides are present at the surface.

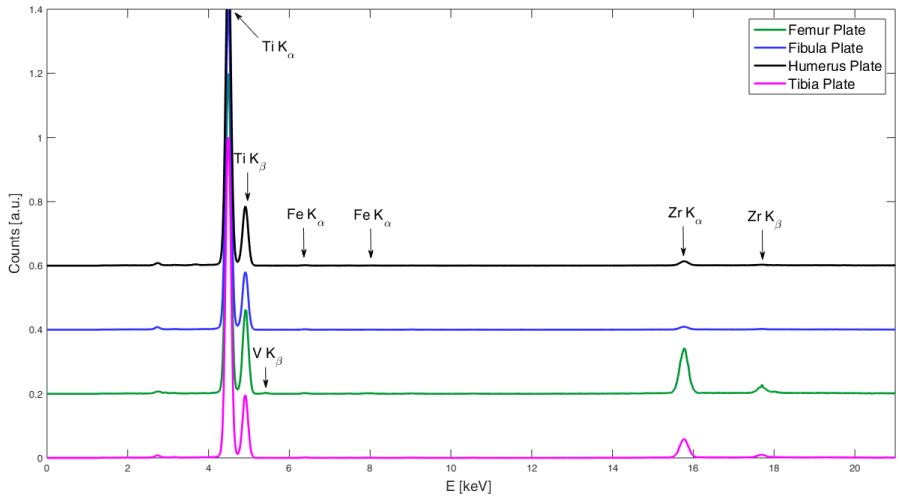

Figure 1: X-Ray Fluorescence spectrum of the four investigated orthopedic titanium implants. The spectra have been shifted vertically for clarity.

The aim of the second experiment is to analyze the effect of different heat treatment temperatures on titanium surface properties for orthopedic implants and to confirm the existence of zirconium oxides at the surface.

X-ray diffraction (XRD) is used to assess the crystalline composition of the samples as well as the types and phases of oxide formed after the different steps of treatment of the titanium implants (room temperature, 300 °C, 400 °C, 500 °C, 600 °C and 700 °C). In this experiment a 20 keV X-ray diffraction setup of BL9 with a mar345 imaging plate detector and 340 mm sample-detector distance is used. For examination, the samples have been dissected to it set up. Heating the samples (from room temperature to 700 °C) is performed by a heating stage DHS 1100 by Anton Paar. Three titanium implants (distal tibia plate, distal fibula plate and distal femur plate) are investigated. In addition a zirconium (ZrO_2) Wafer is analyzed by heat treatment using the same temperatures as the implants.

For instance figure 2 shows the x-ray diffraction pattern of the distal tibia plate at different temperatures. The typical peaks of titanium in the XRD patterns are detected for all of the implants. As the temperature increases the peaks width decreases which relates to crystal growth of titanium.

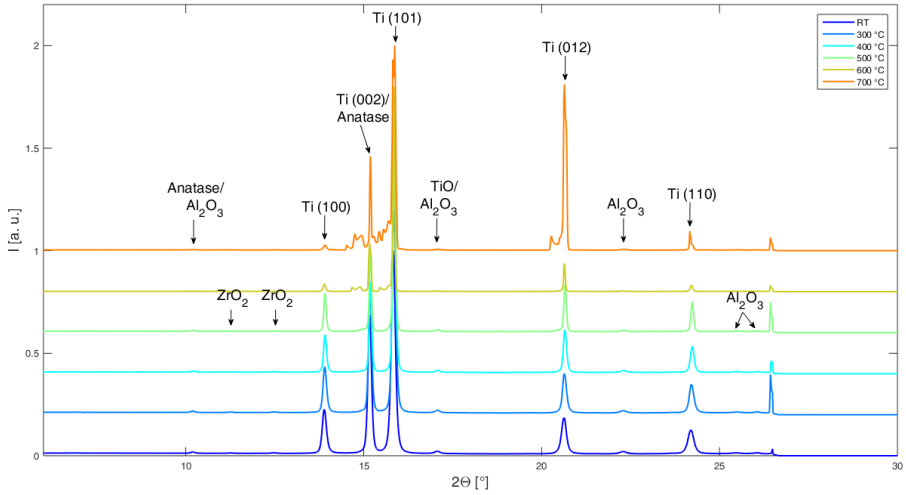

Figure 2: X-ray diffraction analysis of the distal tibia plate by different heat treatment. The spectra have been shifted vertically for clarity.

The diffraction pattern of the distal tibia plate also shows that the crystallized oxide structure is composed of anatase ($2\Theta = 10{,}19\,°C$, $13{,}89\,°C$) however those diffraction peaks disappear with higher heating temperature ($> T = 500\,°C$). The rutile TiO_2 phase does not emerge with characteristic diffraction peaks. Furthermore, diffraction peaks origination from ZrO_2 are clearly visible and confirm the mentioned hypothesis.

Additionally figure 2 proofs the existence of Al_2O_3. Some implant manufacturers are using Al_2O_3 to sand-blast the machine implant to modify the surface topography. Rough-surfaced implants provide an effective surface for bone implant contact and encourage cell proliferation [2]. However, some particles may not have been completely removed from the implant surface.

References

[1] D.M. Brunette, P. Tengvall, Marcus Textor, P. Thomsen, *Titanium in Medicine: Material Science, Surface Science, Engineering*, Springer-Verlag, Berlin and Heidelberg 2001.

[2] DIN EN ISO 5832-2:2012-08, *Chirurgische Implantate - Metallische Werkstoffe - Teil 2: Unlegiertes Titan*, (ISO 5832-2:1999).

[3] Yury G. Gogotsi, Irina V. Uvarova, *Nanostructured Materials and Coatings for Biomedical and Sensor Applications*, Springer Science+Business Media Dordrecht, 2003.

EXAFS study of lanthanide-doping borate glass material

N. Renten[a], Ö. Öztürk[a], U. Pietsch[a], C. Rimbach[b], St. Schweizer[b]

[a] *Solid State Physics Group, Faculty of Science and Technology, University of Siegen*

[b] *University of Applied Sciences, Soest*

The structure of amorphous materials is the most interesting branch in material science research. In this study, it is shown that one can obtain structural information for glass materials through X-Ray Absorption Fine Structure (XAFS). Borate glass is a non-crystalline (amorphous) solid material which has been widely used in electronic and optoelectronics applications.

Doping of glass with rare earth ions is very important for optoelectronic application of glasses. The characterization of the atomic structure of amorphous solid material has been investigated by Extended X-ray Absorption Fine Structure spectroscopy (EXAFS) technique. A detailed understanding of the crystallization in borate glasses and glass ceramics is essential for the optical properties of the borate glasses, e.g. the color impression, changes with the lanthanide-doping level. The main question to be answered is whether the lanthanide ions are diluted within or outside the thermally-induced crystallites. The accuracy of experimental and theoretical EXAFS has been used to determine the number of nearest neighbor scattering atoms (N) at a distance (R) beyond the ligating shell around the absorbing atom in glasses.

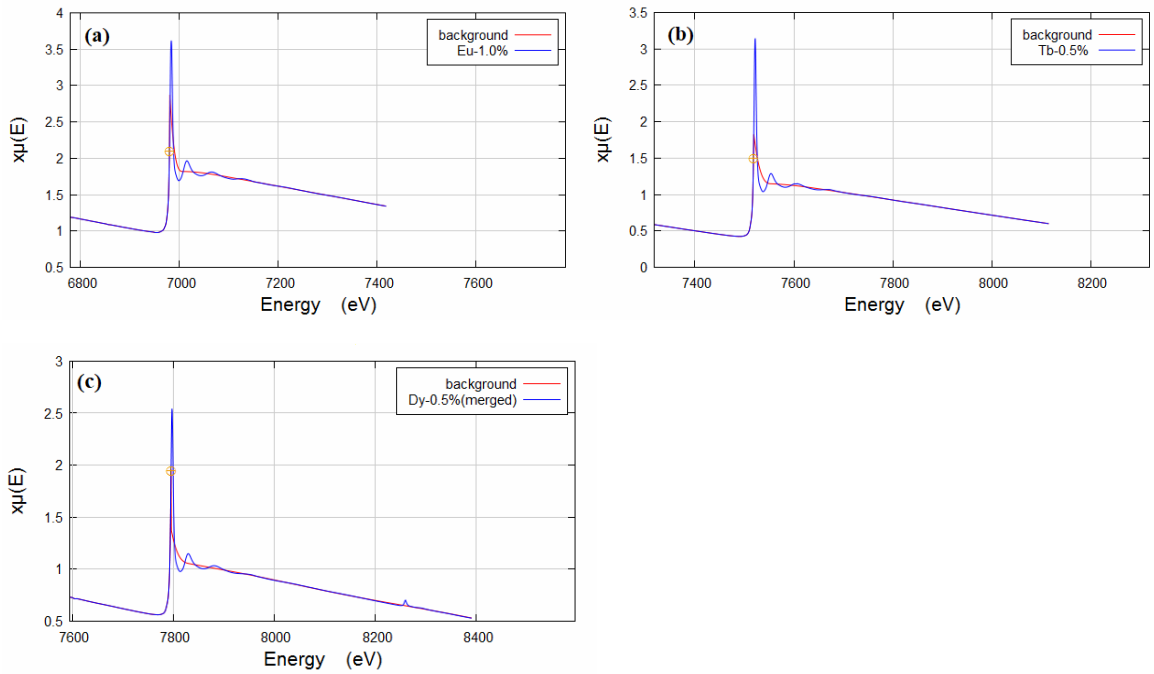

Fig. 1: Raw spectrum of lanthanide doped borate glasses. The useful energy range at the L_{III}-edge was limited by the presence of the L_{II} edge. (a) Europium doped sample measured at 6980 eV edge (b) Terbium doped sample measured at 7518 eV (c) Dysprosium doped sample measured at 7790 eV of their corresponding L_{III} absorption edge.

We have performed preliminary EXAFS experiment at 3 different glass samples doped with 0.5 mol % Tb_4O_7, 1.0 mol% Eu_2O_3 and 0.5 mol% Dy_2O_3. Samples were prepared as thin films and the experiments were performed at DELTA, BL10, which offers access to the entire energy range which is required for a study of the rare earth L_{III} absorption edges. The EXAFS spectra were recorded in transmission mode at room temperature.

In Fig. 1, EXAFS measurements of all three samples at respective energy edges; Eu (6980eV), Tb (7518eV), Dy (7790eV) are seen. The collected data were analysed and fitted using the Athena (background subtraction part) and Artemis (data analysing part) software packages.

The analysis for the first shell signal could be observed for the Eu doped sample in Fig.2. Only first shell signals are analysed as it is more observable and atoms in the first shell of amorphous material can give accurate information than other shells. Simulation of the EXAFS for the Eu−O scattering path was calculated by FEFF program. The calculated spectrum was compared with the experimental results from the known B_2EuO_4 crystal to find the optimum over-all parameters.

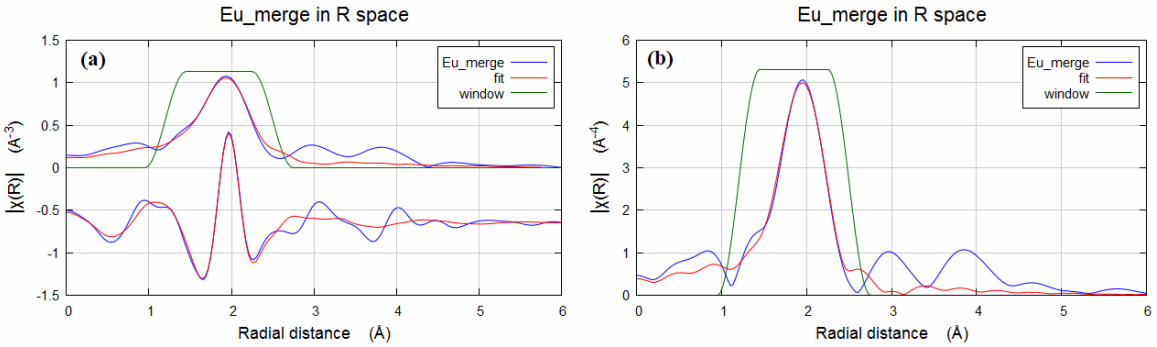

Fig. 2: First shell fit to the EXAFS of Eu_2O_3. (a) Real (top) and magnitude (bottom) parts of χ(R) measured data is shown. (b) As we see, one peak at R_{1st} = 1.93 Å is clearly visible. This peak corresponds to the Eu−O distance (R_{1st}) in the sample.

Analysis of the lanthanide L_{III}-edge EXAFS spectra suggested that most of lanthanide ions are surrounded by oxygen atoms and their bond lengths, also the mean-square displacement factors σ^2 of the different bonds are similar in all three amorphous materials (see Table. 1). This means that the static disorder is similar in all three materials. We expect similar samples to have similar bond lengths, structural and thermal disorder, and number of nearest neighbours.

Shell	CN	S_0^2	R (Å)	σ^2 (Å^2)	ΔE_0 (keV)
Eu-O	2	3.86(0.38)	2.42(0.01)	0.013(0.001)	5.64(0.83)
Tb-O	3	3.37(0.44)	2.38(0.01)	0.016(0.002)	5.38(1.02)
Dy-O	1	9.32(0.99)	2.35(0.04)	0.015(0.002)	1.95(0.83)

Table 1: Best-fit results for the experimental data using the theoretical references and their uncertainties (in parentheses) for the refined first shell parameters for Eu, Tb, and Dy.

Structural investigations of the garnet $Ho_3Al_5O_{12}$

D. Petrov[a], R. Wagner[b], D. Lützenkirchen-Hecht[b]

[a]*Department of Physical Chemistry, Plovdiv University "Paisii Hilendarski", Tsar Asen Str. 24, 4000 Plovdiv, Bulgaria*
[b]*Fakultät 4-Physik, Bergische Universität Wuppertal, Gaußstr. 20, 42097 Wuppertal, Germany*

Garnets are a class of oxide materials that are interesting because of e.g. their magnetic [1-4] and optic properties [4-6], which are in particular used in lasers for medical applications (see for example refs. [7-10]). Garnets in general contain a metal (M) and a rare earth metal (R), and posses a composition $R_3M_5O_{12}$. Well-known, -investigated and -used examples are the Yttrium-Aluminium-Garnet (YAG), Yttrium-Iron-Garnet (YIG), Terbium-Iron-Garnet (TbIG) or Europium-Iron-Garnet (EuIG). The unit cell of the lattice is cubic (space group Ia-3d, no. 230) and contains 8 formula units. The 24 rare earth cations usually occupy the dodecahedral c-sites, while 2/5 of the metal cations are on octahedral a-sites and the remainder on the tetrahedral d-site [11]. In the past, several different preparation routes for the garnets such as pyrolysis [12], solid-state reaction routes [13-15] and sol-gel synthesis [15] have been successfully applied. Here we will focus on $Ho_3Al_5O_{12}$ particles prepared by a modified sol-gel reaction using in-situ polyesterification between malic acid ($C_4H_6O_5$) and ethane-1,2-diol. The gel was prepared with stoichiometric amounts of analytical grade, high-purity sesquioxide Ho_2O_3 (99.99 %), $Al(NO_3)_3 \cdot 9H_2O$ and malic acid, with a molar ratio between $Ho_2O_3 : Al_2O_3$ of 3 : 5, according to the desired structure formula $Ho_3Al_5O_{12}$. In a first step, Ho_2O_3 was dissolved in 0.5M malic acid, then 0.1M aluminium nitrate was added to this clear solution, and the resulting mixture was stirred for 2 hours at 353 K. After addition of 6 ml ethane-1,2-diol, the solution was slowly evaporated under constant magnetic stirring to obtain a transparent gel, which was subsequently oven-dried for 2 h at 383 K until it turned into a black powder in the next step. Finally, the sample was heated in air for 10 h at 1070 K to ensure a complete reaction.

The structure and the morphology of the samples have been investigated using scanning electron microscopy and EDX, typical examples of which are presented in Fig. 1. The sample obeys crystallites with a typical size between 1 and 10 μm, and a platelet-like morphology. Besides carbon contaminations at 275 eV, EDX only shows oxygen, aluminium and holmium signatures as expected, and a detailed quantitative evaluation gave a composition of 55.7 ± 0.6 % O, 18.2 ± 0.4 % Al and 26.1 ± 0.5 % Ho, which would imply an excess of Holmium and an Aluminium deficiency in the garnet.

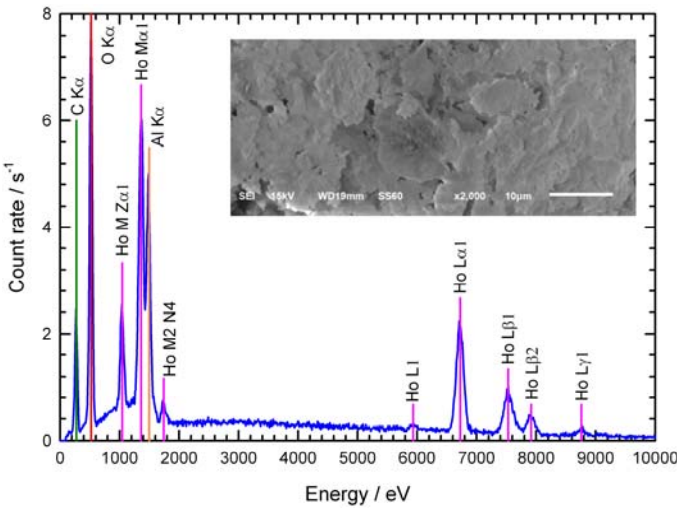

Fig. 1: Energy dispersive X-ray spectrum and scanning electron microscopy image (inset) of the investigated $Ho_3Al_5O_{12}$ – garnet sample. The identified spectral contributions of the different elements are indicated. According to the EDX quantification, a composition of $Ho_{5.22}Al_{3.64}O_{11.4}$ was determined.

Ho L_3-edge EXAFS of the synthesized Ho-containing garnet samples were measured in transmission mode at DELTA beamline 10 using a Si(111) channel-cut monochromator and ionization chambers as detectors [16]. The samples were homogeneously distributed on self-adhesive tape, and several tapes were stacked in order to obtain a sufficient absorption at the Ho L_3-edge (8071 eV). For comparison and in order to judge the chemical valence of the Ho within the garnet, a Ho_2O_3 sample was measured for comparison. Results of the X-ray absorption measurements are presented in Fig. 2. Obviously, the white line position and the edge of both spectra coincide quite well, indicating that Holmium is present in a 3+ valence state as expected.

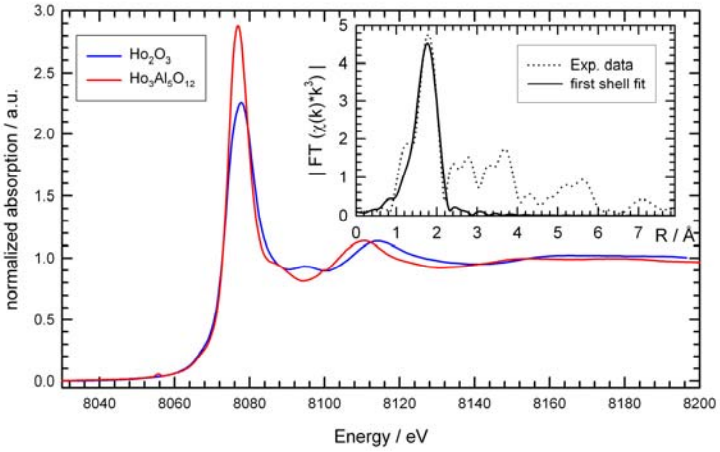

Fig. 2: Normalized Ho L_3-edge near edge X-ray absorption spectrum of the synthesized Ho-garnet in comparison to Ho_2O_3. The magnitude of Fourier-transform $|FT(\chi(k)*k^3)|$ as well as a fit of the first Ho-O shell are presented in the inset.

From the fit of the extracted EXAFS fine structure $\chi(k)$, the nearest neighbor bond distance as well as the disorder in the first shell were determined. According to our results, 8 nearest oxygen neighbors are distributed in the first shell, as expected for Ho on a dodecahedral c-site [11], with a Ho-O bond distance of 2.29 ± 0.06 Å, a value which is substantially smaller compared to e.g. YIG with about 2.38 Å [17]. However, this decrease in bond distance may be explained by the smaller ionic radius of the Al^{3+} ions on the a- and d-sites of the garnet structure compared to Fe^{3+}, and the resulting larger lattice constant of YIG with a value of 12.38 Å [17, 18] in comparison to about only 12.01 Å found for $Ho_3Al_5O_{12}$ [18]. From this lattice constant, a Ho-O bond distance of 2.33 Å can be calculated – this value is close to that derived from the EXAFS data analysis here. Additional peaks in the Fourier-transform may originate from Al neighbours in a distance range from about 3 Å to 4 Å as well as to the nearest Ho-Ho interaction at about 3.8 Å.

X-ray diffraction experiments have already been performed to support this interpretation. Those measurements show the presence of diffraction peaks belonging to a garnet structure, however, additional Bragg peaks could also be detected. Therefore a phase identification as well as a Rietveld refinement are necessary, together with a more elaborate analysis of the EXAFS data to elucidate all details of the synthesized Ho-containing oxides.

Acknowledgement

We gratefully acknowledge the DELTA machine group for providing synchrotron radiation reliably.

References

[1] G.S. Krinchik, M.V. Chetkin, Sov. Phys. JETP 13 (1961) 509.
[2] S. Iida, Phys. Lett. 6 (1963) 165.
[3] J. Felsteiner, S.K. Misra, Phys. Rev. B 24 (1981) 2627
[4] M. Guillot, A. Marchand, F. Tchou, H. Le Gall, Z. Phys. B Cond. Matter 49 (1982) 221.
[5] Dubnikova, E. Garskaite, A. Beganskiene, A. Kareiva, Opt. Materials 33 (2011) 1179-1184. (XRD, IR, SEM)
[6] A.M. Kalashnikova, V.V. Pavlov, A.V. Kimel, A. Kirilyuk, T. Rasing, Low Temp. Phys. 38 (2012) 863.
[7] H.A. Razvi, J.D. Denstedt, S.S. Chun, J.L. Sales, J. Urol 156 (1996) 912.
[8] R.L. Kuo, P. Aslan, P. Zhong, G.M. Preminger, J. Endourology 12 (1998) 523.
[9] A.P. Patel, B.E. Knudsen, Curr. Urol. Rep. 15 (2014) 397.
[10] P.Kronenberg, O. Traxer, World J. Urology 33 (2015) 463.
[11] M.A. Gilleo, Ferromagnetic Insulators: Garnets, Ferromagnetic Materials, Vol. 2, ed. E.P. Wohlfarth (North-Holland, Amsterdam, 1980).
[12] J. Marchal, T. John, R. Baranwal, T. Hinklin, R.M. Laine, Chem. Mater. 16 (2004) 822.
[13] L. Pavasaryte, B.J. López, A. Kareiva, Mendeleev Commun. 25 (2015) 384.
[14] X. Li, H. Liu, J. Wang, H. Cui, S. Yang, I.R. Boughton, J. Phys. Chem. Solids 66 (2004) 201.
[15] Y. Zhou, J. Lin, M.Yu, S. Wang, H. Zhang, Mater. Lett. 56 (2002) 628.
[16] D. Lützenkirchen-Hecht, R. Wagner, S. Szillat, A.K. Hüsecken, K. Istomin, U. Pietsch, R. Frahm, J. Synchrotron Rad. 21 (2014) 819.
[17] M. Bonnet, A. Delapalme, H. Fuess, M. Thomas, Acta Cryst. B31 (1975) 2233.
[18] P.K. Tien, R.J. Martin, S.L. Blank, S.H. Wemple, L.J. Varnerin, Appl. Phys. Lett. 21 (1972) 207.

X-ray fluorescence spectroscopy investigation of Cu nanoparticle uptake in pea plants

P. Mathiak, R. Wagner, R. Frahm, D. Lützenkirchen-Hecht

Fakultät 4-Physik, Bergische Universität Wuppertal, Gaußstr. 20, 42097 Wuppertal, Germany

Nanoparticles (NPs) of different compositions and sizes are nowadays commercially produced for manifold applications. With dimensions of typically less than 100 nm, especially metallic nanoparticles are thought to have antimicrobial properties, and accordingly a potential risk of a phyto-toxicity. Cu NPs and its oxides are especially used in the agricultural sector [1]. Therefore, there is a large potential risk to introduce NPs into the food chain, for example through contamination of food crops [2, 3]. Up to now it is not well understood if the toxicity of CuNPs and its oxides is a result of chemical speciation/transformation in the plants or not, as only few studies have been carried out on the biotransformation and speciation of metal nanoparticles in plants, and there is a huge lack of information especially for CuNPs (e.g. [4-6]). As a continuation of a previous study [7], the present experiments are meant to investigate the uptake and location of Cu NPs in peas, and to provide information about the influence of Cu NPs on micronutrients in the exposed pea plants.

For this purpose, commercial seeds of a regional German cultivar „kleine Rheinländerin“ peas (Pisum sativum) were grown in soils with well-defined loads of CuNPs. The soils were a mixture of sand (500 g dry mass per pot) and garden mould (400 g dry mass per pot). The experiments were performed using concentrations of 125, 250, 500, and 1000 mg/kg of nCu powder in 1.8 kg air-dried potted soil (P1 - P4), respectively. In the present study, two different sizes of the Cu NPs were used, i.e. 25 nm and 60-80 nm, as obtained from Iolitec (IoLiTec-Ionic Liquids Technologies GmbH, Heilbronn, Germany), so that in total 8 different soils were used, plus an additional control sample without without CuNPs. The maximum concentration used here appears to be reasonable in comparison the maximum concentration recommended for ecotoxicological tests in the ISO guideline 11269-2 [8]. The pea-plants were cultivated for 11 weeks in an open greenhouse and irrigated with rainwater. After five weeks they bloomed and fruits could be observed one week later. After 11 weeks the plants were harvested and separated from the soil, i.e. the roots were carefully washed with water to remove any remaining soil from the plant materials. Subsequently, roots, stems with leaves and seed pods were air-dried separately.

Here we present results of synchrotron-based X-ray fluorescence (XRF) measurements. Due to the high and monochromatic X-ray flux available, even small amounts of trace elements can be proved, and thus synchrotron XRF is ideally suited to identify traces of Cu NPs within the different parts of the plants, as well as to detect various other nutrients such as Mn, Fe or Zn. The experiments have been conducted at beamline 10 of the DELTA storage ring [9], making use of an X-ray energy of 9800 eV for the excitation. The impinging X-ray intensity was measured using a gas-filled ionization chamber, while a peltier-cooled Silicon-Drift-Diode (SDD, Amptek XR-100 SDD) with a pulse processor and a multichannel analyzer was used for the X-ray fluorescence detection. A typical XRF spectrum was collected within 120 s integration time each. Sample preparation includes fine-cutting of the different plant materials, and a distribution of the materials on adhesive Kapton tapes. The fruits were pestled into a fine powder and dispensed on Kapton tape. Cu speciation was done in all roots (P1-P4) and the fruits of the sample with highest Cu NP exposure (P4), for both sizes of the Cu NPs.

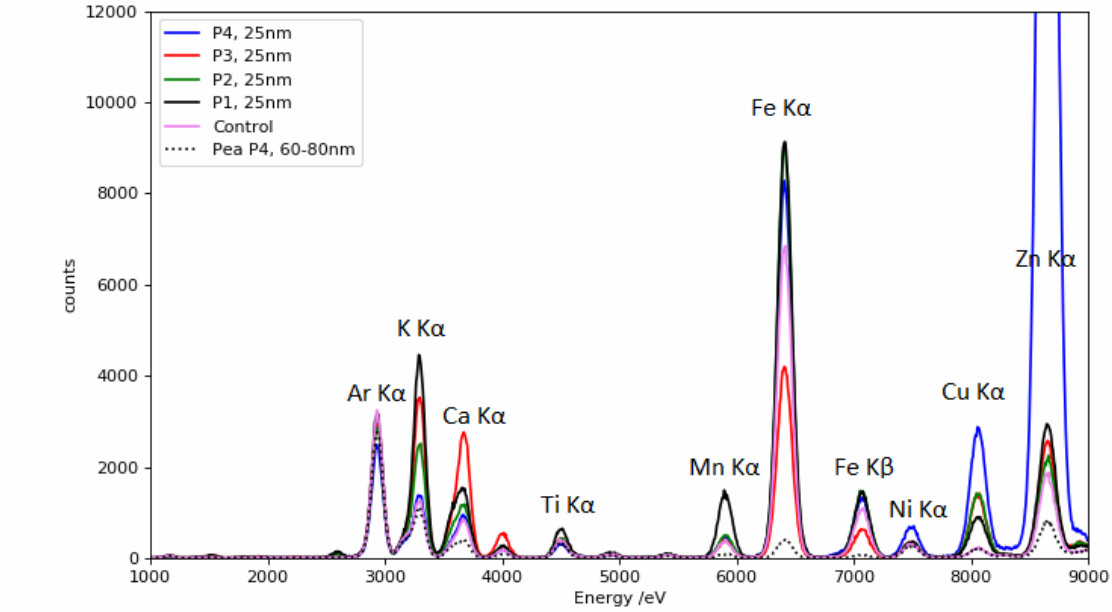

Fig. 1: X-ray fluorescence spectra of the roots of pea plants grown in soil loaded with different amounts of CuNPs as indicated (9800 eV excitation energy). Cu-contributions increase from the control roots (no extra Cu NPs added, Cu level below 1 mg/kg), to samples P1, P2, P3 & P4. Various other cations (K, Ca, Ti, Mn, Fe) are also detectable. A representative spectrum measured from a pea fruit is shown for comparison.

In Fig. 1, X-ray fluorescence spectra excited with a beam of 9800 eV photon energy from different roots from pea plants grown on soils loaded with varying loads of 25 nm Cu NPs are compared. As can be seen, the Cu contributions increase from the control sample (roots of plants grown in a soil with a Cu level <1mg/kg) to P1, P2, P3 and P4 with increasing signals. Various other cations such as K, Ca, Ti, Mn and Fe are detectable at different levels in all investigated samples as well. Changes in the contributions from those metals may as well be attributed to the growth in the CuNP-loaded soil and it is planned to investigate this effect in details in the future. Only a very small contribution of Cu was found in the pea fruit of sample P4, loaded however with 60-80 nm sized Cu NPs. The concentration of Cu is comparable to that found in the roots of the control sample, however also the relative contributions of Fe, Mn, Ca and K are different, indicating that there is an influence of the Cu NP exposure.

For future experiments, it is planned to speciate the contributions from the metal cations, in particular those of Cu, by means of X-ray absorption near edge structure (XANES) experiments. First tests have already indicated the principal feasibility to obtain XANES data of sufficient quality although the concentration of the X-ray absorbing element is in general quite small in the plant samples.

Acknowledgement

The like to thank Prof. Dr. G. Lohaus for the opportunity to use her greenhouse facilities for the germination and the growth of the pea plants investigated here. We furthermore acknowledge the DELTA machine group for providing synchrotron radiation for the presented experiments.

References

[1] J. Trujillo-Reyes, S. Majumdar, C.E. Botwz, J.R. Peralta-Videa, J.L. Gardea-Torresdey, J. Hazard. Mater. 267 (2014) 255.
[2] Y.-N. Chang, M. Zhang, L. Xia, J. Zhang, G. Xing, Materials 5 (2012) 2850.
[3] M.L.J. Xu, H. Iwai, Q. Mei, D. Fujita, H. Su, H. Chen, N. Hanagata, Sci. Rep. 2 (2012) 406.
[4] P. Zhang, Y. Ma, Z. Zhang, X. He, J. Zhang, Z. Guo, R. Tai, Y. Zhao, Z. Chai, ACS Nano 6 (2012) 9943.
[5] M.L. Lopez-Moreno, G. de la Rossa, J.A. Hernandez-Viezcas, H. Castillo-Michei, C.E. Botez, J.R. Peralta-Videa, J.L. Gardea-Torresdey, Environ. Sci. Technol. 44 (2010) 7315.
[6] Y. Ma, P. Zhang, Z. Zhang, X. He, J. Zhang, Y. Ding, J. Zhang, L. Zhang, Z. Guo, L. Zhang, Z. Chai, Y. Zhao, Environ. Sci. Technol. 49 (2015) 10668.
[7] C.O. Ogunkunle, B. Bornmann, R. Wagner, P.O. Fatoba, R. Frahm, D. Lützenkirchen-Hecht, DELTA annual report (2016) p. 81, and Int. J. Phytoremediation (2018), submitted.
[8] ISO Guideline 11269-2: Soil Quality - Determination of the Effects of Pollutants on Soil Flora - Part 2: Effects of Contaminated Soil on the Emergence and Early Growth of Higher Plants. International Organization for Standardization, Geneve, Switzerland.
[9] D. Lützenkirchen-Hecht, R. Wagner, S. Szillat, A. K. Hüsecken, K. Istomin,U. Pietsch, R. Frahm, J. Synchrotron Rad. 21 (2014) 819.

Influence of secreted shuttle molecules from metal reducing bacteria on the surface chemistry of stainless steel 304 during initial ennoblement

Nina Wurzler [a], Matthias Dimper [a], Julia Witt [a], Ralph Wagner [b], Dirk Lützenkirchen-Hecht [b], Ozlem Ozcan [a]

[a] *Federal Institute for Materials Research and Testing, Berlin, Germany*
[b] *Faculty 4 - Physics Department, Bergische Universität Wuppertal, Wuppertal, Germany*

Stainless steel is protected against corrosion by the formation of a stable oxide layer composed of iron and chromium oxides. Metal reducing bacteria (MRB) are known to play a role in the onset of pitting corrosion due to the ability to use various metallic compounds as electron acceptors. Different respiratory pathways are susceptible of initiating pitting, which is an increasing problem in many industries such as oil and gas, marine, as well as water and food utilities [1]. Riboflavin (RB) and its derivative flavin mononucleotide (FMN) are the redox centers of microorganisms flavor-enzymes and have a common electroactive moiety [2]. This isoalloxazine group can be present in three different forms and, therefore, store electrons. Electrons produced during the metabolic activities of metal reducing bacteria can be transferred to secreted redox molecules and shuttled to the electron acceptor [3]. Moreover, although they show similar redox reactions, the phosphonate group in FMN can affect the molecules' affinity to iron oxide surfaces.

The so-called ennoblement, the increase of the open circuit potential of stainless steel 304 in contact with MRBs, and the simultaneous beginning of flavin secretion may lead to an alteration of the surface oxides, which could be relevant for the initiation of pits. Furthermore, the presence of flavins during anodic polarization influences the attachment behavior of *Shewanella putrefaciens* and might accelerate microbially induced corrosion [4].

The aim of this study was to investigate, whether flavin molecules can be incorporated into the passive film on stainless steel 304 during anodic polarization, mimicking the initial stages of an ennoblement process, and how it influences the interaction of metal reducing bacteria *Shewanella putrefaciens* (CN32) with the steel surface.

Therefore, ex situ experiments at the Fe K-edge and the Cr K-edge have been performed to elucidate the changes in oxide chemistry of the stainless steel coupons after anodic polarization in different electrolytes with and without flavins (pure 20mM $NaClO_4$ vs. 1µM FMN in 20mM $NaClO_4$ vs. 1µM RB in 20mM $NaClO_4$). Stainless steel 304 coupons cut and polished (up to 1200 grit) were connected as working electrode in a three electrode electrochemical cell (Au counter electrode, sat. Ag/AgCl reference electrode). A 60 min polarization at +50 mV vs. OCP was performed for the preconditioning experiments.

Grazing incicende XANES experiments have been performed at DELTA beamline 10 using a channel cut Si (111) monochromator and gas-filled ionization chambers as detectors and a fluorescence detector. The samples were placed parallel to the x-ray beam and positioned with a transmission detector (Fig. 1). The angle for the measurements was determined by analyzing the reflectance spectra. Fluorescence spectra collected in grazing incidence were analyzed at the Fe and Cr edges directly after pre-conditioning and after 20 h incubation in MRB *Shewanella putrefaciens CN32* containing medium.

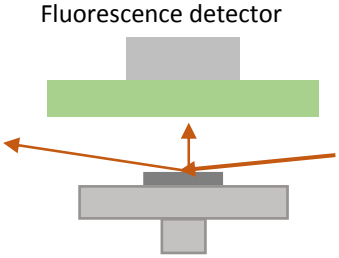

Figure 1: Schematics of ex situ grazing incidence XANES measurements

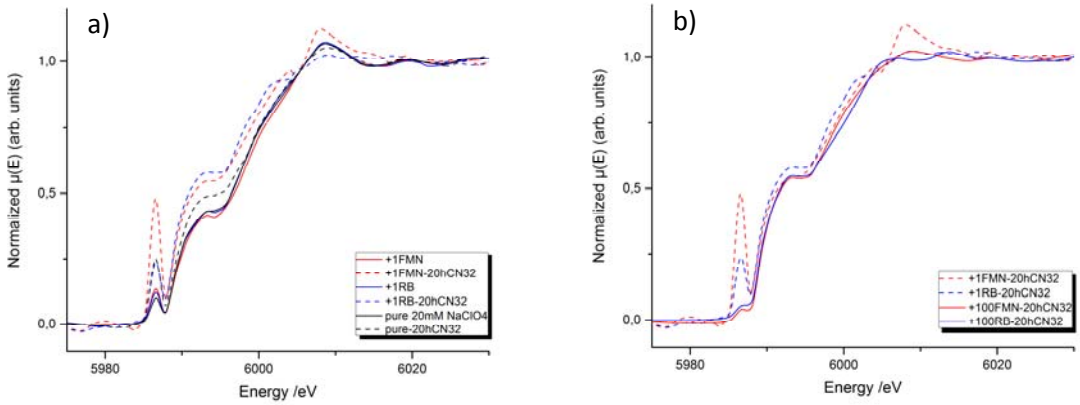

Figure 2: Representative grazing incidence XANES spectra at the Cr K-edge of
(a) preconditioned (solid lines) and incubated samples (dashed lines): **pure** 20 mM $NaClO_4$, **1 µM FMN** in 20mM $NaClO_4$, **1 µM RB** in 20mM $NaClO_4$
(b) incubated samples preconditioned in **1 µM RB**, **1 µM FMN** (dashed lines) and **100 µM RB**, **100 µM FMN** (solid lines)

Pre-conditioning in the presence or absence of flavins does not indicate a significant change in the surface oxide structure, but after incubation with bacteria for 20 h the spectra for Cr-edge show the electro-activity of the bacteria depending on the type of pre-conditioning. As seen in Fig. 2 a, in the presence of bacteria the intensities of the metallic shoulder and the pre-peak assigned Cr(VI) are increasing. The metallization behavior is more dominant on samples pre-conditioned with the addition of 1 µM RB, whereas the highest amount of Cr(VI) was observed with samples pre-conditioned in electrolyte containing 1µM FMN. Moreover, the intensities in the energy range for Cr(III) are increasing. The increase of flavin concentration does lead to a significant decrease in the Cr(VI) pre-peak and in Cr(III) intensity (Fig.2 b). Ongoing work indicates that the presence of flavins doesn't only affect he passive film composition, but also the passive film thickness, which leads to different corrosion behavior in the presence of MRB. Therefore, further ex-situ measurements are planned to investigate longer incubation times.

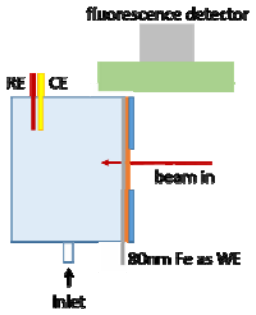

Figure 3: Schematics of in situ cell with a 80 nm Fe film deposited on Kapton © foil for backscattered fluorescence mode detection

For the in situ experiments on thin iron films, a measurement cell shown in Fig. 3 has been constructed and tested. Iron films of different thicknesses have been deposited by means of e-beam deposition on Kapton© foils. In the cell assembly, the iron film is facing the electrolyte and the Kapton© foil is acting as the window for the incident beam and backscattered fluorescence detection. Initial tests have been performed to optimize the thickness of the iron film for obtaining adequate surface sensitivity and signal intensity. Based on the results of these initial tests, 80 nm was determined as the optimum thickness for in situ measurements. In upcoming beamtimes, in-situ studies will be performed to study the kinetics of the iron and chromium dissolution separately in the presence of flavins and during attachment and biofilm formation.

Acknowledgement
We gratefully acknowledge the DELTA machine group for providing synchrotron radiation reliably.

References

1. Fredrickson, J.K., et al., *Towards environmental systems biology of Shewanella.* Nat Rev Microbiol, 2008. **6**(8): p. 592-603.
2. Li, R., et al., *Soluble electron shuttles can mediate energy taxis toward insoluble electron acceptors.* Environ Sci Technol, 2012. **46**(5): p. 2813-20.
3. Marsili, E., et al., *Shewanella secretes flavins that mediate extracellular electron transfer.* PNAS, Proceedings of the National Academy of Sciences, 2008. **105**(10): p. 3968-73.
4. Carmona-Martínez, A.A., et al., *Electron transfer and biofilm formation of Shewanella putrefaciens as function of anode potential.* Bioelectrochemistry, 2013. **93**: p. 23-29.

EXAFS data modelling of Nb processed in N_2-atmospheres at elevated temperatures

J. Kläs, R. Wagner, B. Bornmann, R. Frahm, D. Lützenkirchen-Hecht

Fakultät 4-Physik, Bergische Universität Wuppertal, Gaußstr. 20, 42097 Wuppertal, Germany

A high-temperature treatment of Nb metal foils in dilute N_2-atmospheres was conducted and the induced structural changes were monitored by in-situ EXAFS experiments at the Nb K-edge (18986 eV). Such mild nitriding treatments have shown to result in substantially improved radiofrequency superconducting properties in moderate acceleration fields [1]. The processing of the Nb foils included an annealing treatment in vacuum for 1 h at 900 °C, and a subsequent exposure to high-purity (5.0) N_2-gas under a pressure ranging from $3x10^{-3}$ up to 50 mbar for varying times. The EXAFS experiments were conducted at DELTA beamline 8 using the Si(311) monochromator and gas-filled ionization chambers as detectors for incident and transmitted intensities. Here we will focus on additional experiments and in particular on the evaluation and modeling of the EXAFS data. In Fig. 1, the effect of N_2-exposure for different conditions is exemplarily shown, it is obvious that a distinct reduction of all the EXAFS features occurs with increasing N_2-exposure, while however the features typical for the bcc-structure of metallic Nb are conserved. Accordingly, we have modeled the measured EXAFS fine structure oscillations using the bcc Nb lattice (space group no. 229) employing a lattice parameter of a=3.004 Å as starting parameter. We have restricted the fits to only the first two nearest neighbor Nb-Nb shells here. The amplitude reduction factor S_0^2 and the inner potential shift ΔE_0 were treated as global fit parameters, and the distances R_1 and R_2 of the first two Nb-Nb shells as well as the related mean squared displacements σ_1^2 and σ_2^2 were independently fitted. Fits were optimized using k^1-, k^2- and k^3-weighted fine structure data $\chi(k)$ simultaneously using the Artemis software [2].

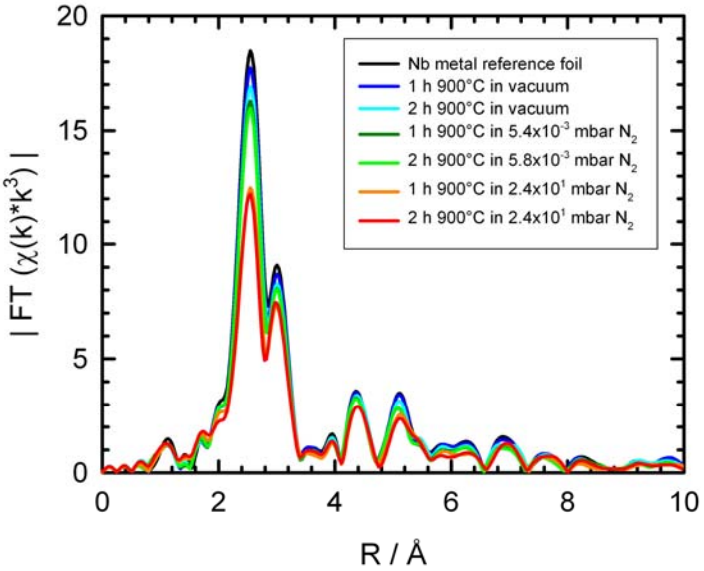

Fig. 1: Influence of a heat treatment on the magnitude of the Fourier-transform of the k^3-weighted EXAFS fine structure $|FT(\chi(k)*k^3)|$ after the treatments as indicated, in comparison to the FT of a Nb metal reference foil. All data were obtained at room temperature after cooling down from the reaction temperature (data are not corrected for phase-shifts. K-range for the Fourier-transform: 1.8 $Å^{-1}$ < k < 15 $Å^{-1}$.)

Results of the quantitative fits of the EXAFS data are compiled in Fig. 2. The subtle changes of the Fourier-transforms in Fig. 1 result in small changes of the fit parameters, in particular for R_1, R_2 and σ_1^2 and σ_2^2, i.e. distinct structural modifications are detectable. In particular, an irreversible decrease in amplitude with time is obvious for all coordination shells, as well as a slight shift of the bond distances towards larger values can be observed. However, the most prominent changes are observed for σ_1^2 and σ_2^2, where a substantial increase from values of about 0.007 $Å^2$ for an exposure of 0.1 mbar * min are found, while for 100 mbar * min, around 0.010 $Å^2$ was determined. For larger exposures, the trend

indicated a slight decrease of σ^2, which may be interpreted in terms of niobium-nitride (NbN) formation for a larger N_2-supply.

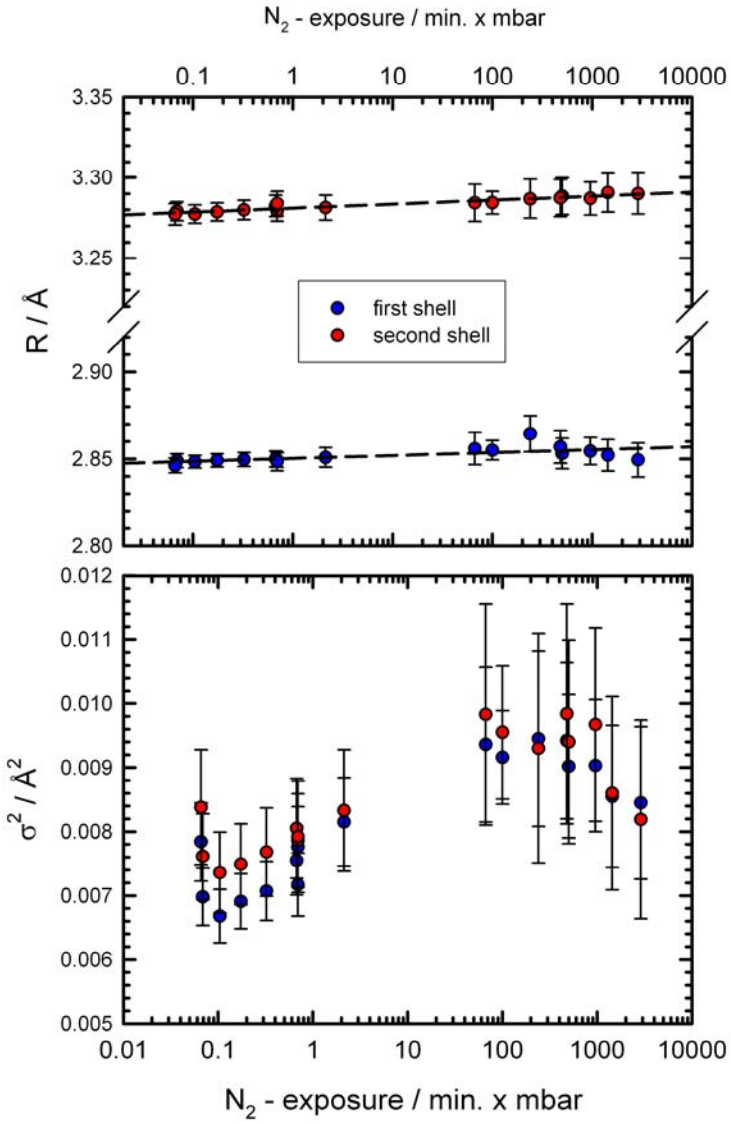

Fig. 2: Structure parameters for the first two Nb-Nb shells, derived from least-square fits of the in-situ room temperature EXAFS data from Nb foils treated at 900 °C in N_2, as a function of the N_2-exposure, i.e. N_2-pressure times the duration of the treatment. (top) Bond distances R_1 (●) and R_2 (●). The dashed lines show a slight increase of the bond lengths with exposure. (bottom) mean squared displacements σ_1^2 (●) and σ_2^2 (●).

In the bcc structure, several octahedral and tetrahedral sites are available for a substituted N-atoms, in between the regular Nb-sites. Those locations appear to be promising candidates for interstitial atoms in the bcc-structure, and it is thus likely that absorbed gas atoms or molecules may reside on those positions. Thus, the increase of the disorder parameter may hint on the occupation of those sites by N-atoms during the heat treatment, and the slight increase of the Nb-Nb bond distances with about 10^{-3} Å per decade (see Fig. 2(a)) also agrees qualitatively with such an assumption.

In order to further clarify this situation, it is planned to perform experiments on Nb samples cooled to cryogenic temperatures after the heat treatment. For lower temperatures, much more details and atoms in larger distances to the central atom may be included in a quantitative fit, thus fostering the fit results and achieving a more detailed insight into the structure of the heat-treated Nb-lattice.

Acknowledgements

We gratefully acknowledge the DELTA machine group for providing synchrotron radiation reliably. The financial support of the BMBF under project No. 05H15PXRB1 is gratefully acknowledged.

References

[1] A. Grasselino, A. Romanenko, D. Sergatskov, et al., Supercond. Sci. Technol. 26 (2013) 102001
[2] B. Ravel, M. Newville, J. Synchrotron Radiat. 12 (2005) 537

Notes

Notes